From DEPARTMENT OF CLINICAL NEUROSCIENCE
Karolinska Institutet, Stockholm, Sweden

DIFFUSION MAGNETIC RESONANCE IMAGING FOR INVESTIGATING ALTERATIONS IN BRAIN ORGANIZATION AFTER INJURY DURING EARLY DEVELOPMENT, WITH SPECIFIC REFERENCE TO THE MOTOR AND VISUAL SYSTEM

Finn Lennartsson

Karolinska Institutet

Stockholm 2016

Published by Karolinska Institutet.
Printed by Eprint AB 2016.

ISBN 978-91-7676-239-4

Diffusion magnetic resonance imaging for investigating alterations in brain organization after injury during early development, with specific reference to the motor and visual system

THESIS FOR DOCTORAL DEGREE (Ph.D.)

By

Finn Lennartsson

Principal Supervisor:
Olof Flodmark
Karolinska Institutet
Department of Clinical Neuroscience

Co-supervisor(s):
Brigitte Vollmer
Karolinska Institutet
Department of Women's and Children's Health

Lena Jacobson
Karolinska Institutet
Department of Clinical Neuroscience
Division of Ophthalmology and Vision

Jonas Larsson
Royal Holloway, University of London
Department of Psychology

Opponent:

A. James Barkovich
University of California, San Francisco
Department of Radiology

Examination Board:
Danielle van Westen
Lund University
Department of Clinical Sciences Lund
Diagnostic Radiology

Orvar Finnström
Linköping University
Department of Clinical and Experimental Medicine
Division of Pediatrics

Markus Nilsson
Lund University
Department of Clinical Sciences Lund
Diagnostic Radiology

To Indy

ABSTRACT

Disturbances or injuries to the brain during early development cause different types of structural abnormalities, depending mainly on the stage of maturation of the brain at the time of the insult. These are, herein, collectively referred to as early brain lesions. Early brain lesions can cause a wide range of clinical symptoms including disturbances to motor or sensory functions, perception, cognition, communication and behaviour; epilepsy is common. There is a large variation in outcomes and severity of impairments, contributed to by the superior compensatory mechanisms in the young brain compared to the adult brain.

The overall aim of this thesis was to study the organization of the motor and visual system in early brain lesions by using diffusion-weighted magnetic resonance imaging (MRI) and white matter fibre tractography. The specific aims of the studies on the motor system (Study I & II) were to investigate the microstructural changes in motor and sensory tracts in individuals with early brain lesions causing unilateral cerebral palsy (CP), and to explore associations with hand motor function. The specific aims of the studies on the visual system (Study III & IV) were to seek evidence of a relationship between damage to the immature optic radiation (OR) and subsequent development of the retinal ganglion cell layers, and associated visual field function, in individuals with early brain lesions caused by with white matter damage of immaturity (WMDI).

The results from Study I showed that diffusion parameters in central cortico-fugal fibres, distant from the primary lesions, were sensitive markers for injury and correlated with hand function in the non-dominant hand in children with unilateral CP. Study II used an improved fibre tractography method in the same cohort, to study the cortico-spinal tract (CST) and adjacent thalamic projections to the primary sensory cortex (TRS1). The results showed dissimilarities in both the structural and the parametric changes seen in CST compared to TRS1 on the lesion-side, indicating that the tracts are affected differently by the injury; however, reactive changes in TRS1 is a possible alternative explanation.

The results from Study III show that injuries to the immature OR are associated with reduced thickness of the retinal nerve fibre layer, causing predictable visual field defects. Study IV showed, by including visual field mapping with functional MRI, a strict topographical and correlating relationship between injury to the superior portion of the OR, the part of OR that projected to the visual field map below the horizontal meridian, and the secondary thinning of the macular ganglion cell layer, and corresponding visual field defects. The results from both studies provide convincing evidence of retrograde trans-synaptic degeneration in WMDI. The structural changes to the OR may suggest re-organisation to the tract upon injury.

The overall conclusion from this thesis is that diffusion-weighted MRI is more sensitive in detecting and assessing the extent of early brain lesions than conventional MRI, and provides a sensitive marker for studying relevant changes to structural entities of fibre tracts that have a direct effect on the clinical function.

LIST OF SCIENTIFIC PAPERS

I. Holmström L*, Lennartsson F*, Eliasson A-C, Flodmark O, Clark C, Tedroff K, Forssberg H, Vollmer B. Diffusion MRI in corticofugal fibers correlates with hand function in unilateral cerebral palsy. Neurology 2011, 77(8):775-783

   * These authors contributed equally to this work

II. Lennartsson F, Holmström L, Eliasson A-C, Flodmark O, Forssberg H, Tournier J-D, Vollmer B. Advanced Fiber Tracking in Early Acquired Brain Injury Causing Cerebral Palsy. Am J Neuroradiol. 2015, 36(1):181-187

III. Lennartsson F, Nilsson M, Flodmark O, Jacobson L. Damage to the Immature Optic Radiation Causes Severe Reduction of the Retinal Nerve Fiber Layer, Resulting in Predictable Visual Field Defects. Invest Ophthalmol Vis Sci. 2014, 55(12):8278-8288

IV. Lennartsson F, Nilsson M, Flodmark O, Jacobson L, Larsson J. Topographical correspondence between injuries to the immature optic radiation and thinning of the macular ganglion cell complex – evidence of retrograde trans-synaptic degeneration in the visual system. [Manuscript]

CONTENTS

LIST OF ABBREVIATIONS

ADC	Apparent diffusion coefficient
AFD	Apparent fibre density
CerPed	Cerebral peduncle
CP	Cerebral palsy
CSD	Constrained spherical deconvolution
CSF	Cerebrospinal fluid
CST	Cortico-spinal tract
CVI	Cerebral visual impairment
$D_{\perp}$ (or $ADC_{\perp}$)	Radial diffusivity (in DTI equal to the mean of eigenvalues λ_2 and λ_3)
$D_{//}$ (or $ADC_{//}$)	Axial diffusivity (in DTI equal to the largest eigenvalue λ_1)
dMRI or DWI	Diffusion-weighted magnetic resonance imaging
dODF	Diffusion orientation distribution function
DTI	Diffusion tensor imaging
EPI	Echo-planar imaging
FA	Fractional anisotropy
FLAIR	Fluid-attenutation inversion-recovery
fMRI	Functional magnetic resonance imaging
FOD or fODF	Fibre orientation distribution function
FTA	Fibre tract assessment
GCL_IPL	The macular ganglion cell layer and the inner plexiform layers
GM	Grey matter
GMH	Germinal matrix haemorraghe
GW	Gestational week
HARDI	High-angular resolution diffusion-weighted imaging
HI	Hypoxic-ischemic injury
IVH	Intraventricular haemorraghe
LGN	Lateral geniculate nucleus
MD	Mean diffusivity (for DTI equal to the trace of diffusion tensor)
MRI	Magnetic resonance imaging
OCT	Ocular coherence tomography

OR	Optic radiation
PAS	Perinatal ischemic stroke
PHI	Periventricular haemorrhagic infarct
PLIC	Posterior limb of internal capsule
PVL	Periventricular leukomalacia
RGC	Retinal ganglion cell
RNFL	Retinal nerve fibre layer
ROI	Region-of-interest
RTSD	Retrograde trans-synaptic degeneration
SP	Subplate
SVZ	Subventricular zone
T1w	T1-weighted magnetic resonance image
T2w	T2-weighted magnetic resonance image
TE	Echo time
TMS	Transcranial magnetic stimulation
TR	Repetition time
TRS1	Thalamic projections to the primary sensory cortex
V1	Primary visual cortex/striate cortex
VF	Visual field
WM	White matter
WMDI	White matter damage of immaturity

1 INTRODUCTION

The work presented in this thesis concern injuries to the brain during early development. In order to understand the pathophysiology and functional consequences of early brain lesions, a basic understanding of typical brain development is required. Therefore, this introduction commences with an overview on typical early brain development and the development of the motor and visual systems. The level of detail is not overly high, but the field is huge and hence the length of the text. This is followed by a section on pathophysiology of injuries during early brain development, subcategorized according to the timing of the insult, and consequences concerning the motor and visual system. Following this is a section on neuroimaging in early brain lesions. As we will see, neuroimaging, specifically magnetic resonance imaging (MRI), is key in detecting and describing early brain lesions. This is covered in one section, divided into sub-sections for conventional MRI and diffusion-weighted MRI (dMRI). Finally, there will be a section on the topic of brain re-organisation in the motor and visual system after injuries during early brain development.

1.1 EARLY BRAIN DEVELOPMENT

The development of the nervous system starts around embryonic day 18 (E18), with the formation of the neural plate in the midline of ectoderm in the dorsal aspect of the embryo. From this stage the neuronal development follows a tightly regulated series of partly overlapping developmental events to form the central and peripheral nervous systems as we know them. The majority of the major developmental events occur during gestation; only the later stages of the cortical organization (superficial layers), the short-range connectivity and the majority of the myelination occur after birth. During the rest of life the overall structure of the nervous system is static, but its function is dynamically modulated, primarily from the formation, maintenance and elimination of synapses and the modulation of myelination, partly from experience-driven processes.

Early brain lesions considered in this thesis are adverse events, either disturbances or injuries, occurring during the developmental stages of neurogenesis, neuronal migration and cortical development as well as during the establishment of the cortical connectivity. These two major developmental events will be considered in more detail in the following sections. For a more detailed overview of the development of the cerebral cortex and the brain connectivity the reader is referred to Bystron et al (1) and Kostović and Jovanov-Milošević (2) respectively.

1.1.1 Neurogenesis, neuronal migration and cortical organization

The first step in early brain development is generation of the billions of cerebral neurons and placing them in the right subcortical and cortical locations. This is summarized in the processes of neurogenesis, neuronal migration and cortical organisation. Injuries or disturbances to these processes are part of the spectrum of early brain lesions and therefore the processes of typical early brain development need first to be understood.

The neural tube closes on embryonic day 30 (E30) in humans (3), and shortly after this the neuronal proliferation and differentiation from the dividing neuronal epithelial cells (often referred to as neuronal stems cells) begins. The neuroepithelial cells form a pseudo-stratified epithelium with a radial organization lining the surface of the neuronal tube, i.e. the developing ventricles, and is called the ventricular zone (VZ) (1). When neurogenesis starts, the cell division is symmetric and the thickness and surface area of the VZ increases accordingly. At a certain point, approximately E33 in humans, there is a switch to asymmetrical cell division, with one daughter cell remaining progenitor and the other postmitotic cell destined to become neuron or glial cell (1). At the start of neurogenesis, the neuroepithelial cells down-regulate their epithelial characteristic to divide into cells with extending long apical processes towards the pial surface (1). These cells have been named radial glial cells (1). They constitute a radial scaffolding used by postmitotic neurons and glia cells to migrate along the cells, away from the VZ towards the pial surface.

The earliest post-mitotic cells to reach the pial surface form a structure called the pre-plate (PP). The PP is established around 5-6 gestational weeks (GW) and lies in between the VZ and the pial surface. The following wave of migrating neurons comes in 7-8 GW and divides the PP into a thin superficial layer, the marginal zone (MZ; future cortical layer 1), and a deep subcortical layer called the subplate (SP). The next wave of migrating neurons will pass the SP but is halted by the MZ to establish the first cortical layer, layer 6, of the cortical plate. Hereafter, every new wave of migrating neurons will pass the older cortical layers to form a new layer just below the MZ. In this way layers 6 up to 2 are established in an inside-out pattern. The result is the well-known laminated structure of the cortical layers: projecting pyramidal cells in layers 5-6, neurons receiving afferent thalamic input in layer 4 and neurons with cortico-cortical connections in layers 2-3. Finally the MZ turns into cortical layer 1, which has intra-cortical connections. An outline of the cortical layers are given in Figure 1-1 (p. 13).

The radial glial cells in the VZ produce both glial cells and neurons. With time, a distinct layer of neuronal progenitor cells will form in the upper layer of the dorsal VZ, the so called subventricular zone (SVZ). The progenitors in the SVZ produce mainly neurons, first glutaminergic pyramidal cells for the deeper cortical layers up until midgestation (20 GW) and thereafter GABA-ergic interneurons for the superficial cortical layers (Figure 1-1, p. 13). The ventral and basal VZ are often referred to as the ganglionic eminence (GE), and produce mainly GABA-ergic neurons. These GABA-ergic neurons migrate locally to form the basal ganglia and thalamus, and tangentially towards the SP and the cortex to form interneurons (Figure 1-1, p. 13). A collective term often used by clinicians for the proliferating zones around the ventricles is the germinal matrix (GM). With the neurogenesis and migration, an intermediate zone (IZ), i.e. the future white matter, develops between the VZ/SVZ and the SP. This IZ contains the neuronal axons and an abundance of glial cells in different stages of maturation.

The bulk of neurogenesis is completed by mid-gestation (20 GW) (1). The neuronal stem cells, the neuroblasts, are tightly regulated to produce multi-potent progenitor cell lineages

with given fates during certain times of development. In turn each progenitor cell population is also strictly controlled by intrinsic and environmental factors to produce certain neuronal or glial cell lineages during a set time of development (4). In this manner, a predictable scheme of neurons and glial cells with different fates are produced, in which pre-plate neurons proceed cortical plate neurons, etc. The results are waves of fate-specific neuronal and glial cell populations. When each population of fate-specific progenitor cells is exhausted no more neurons with that specific fate are generated. Consequently, the VZ regresses and finally disappears, around 27 GW for the dorsal VZ, and around term for the GE. On the contrary, late neurogenesis, mainly in the form of GABA-ergic interneurons destined for superficial cortical layers 2-3, persists in the SVZ (peak 22-27 GW) throughout gestation and to some extent thereafter in life.

The location of the proliferative zones (i.e the germinal matrix) lining the lateral ventricles and the routes of neuronal migration are outlined in Figure 1-1 (p. 13).

1.1.2 Cortical connectivity

Mid-gestation (~ 20 GW) is a turning point in the early brain development, with a shift from neurogenesis and neuronal migration to establishing brain connectivity, i.e. to "wire" the brain. The cerebral network is the basis for the integrated brain function. The structural connectome is characterised by cortico-fugal connections (i.e. cortical projections to sub-cerebral and subcortical structures) from the deep layers 5-6, the thalamo-cortical afferents to layer 4, the inter-cortical fibres to layer 3 (long association and commissural fibres) and layer 2 (short association) and a wealth of intra-cortical connections in the superficial layers 1-3 (Figure 1-1, p. 13). The developing connectivity follows, like the cortical histogenesis, an inside-out pattern. The connectivity is commonly affected in early brain lesions. Knowledge of this process is therefore important, and is described in more detail below.

A pivotal structure in the development of the cortical organization and connectivity is the subplate (SP). The SP contains a wealth of GABA-ergic interneurons that form transient connections with, first, migrating neurons, and later with incoming axons until the cortex is apt to receive them (5). In fact, the axonal outgrowth starts at the same time as the post-mitotic neurons migrate away from the proliferative zone. In this way the SP can be seen as a "waiting zone". There is evidence that axons can wait for weeks in the SP before entering the cortex (5,6).

The axons of deep-layered projection neurons have found their subcortical and subcerebral targets early in the gestation. It is unclear when the layer 6 neurons connect with the basal ganglia, but the efferents of the pyramidal cells in layer 5 are found quiescent in the brainstem from 8-17 GW before they decussate in the pyramids and extend towards the cervical spinal cord about 17-18 GW (7,8).

Thalamo-cortical afferents navigate through the internal capsule and the IZ to reach the SP. Here they become abundant by the end of mid-gestation (20-23 GW) and synapse with both GABA-ergic and glutaminergic interneurons in the SP in the wait to enter the cortical plate.

These transient synapses with SP interneurons form rudimentary neuronal circuits which show endogenous activity (5,9). At this stage GABA-ergic neurons can be excitatory before they later switch to become inhibitory. The thalamo-cortical afferents gradually start entering the cortical plate and form synapses with targets in layer 4 during 24-32 GW (2). The arrival of the thalamo-cortical afferents in the cortical plate is crucial in the cortical development as it initiates the synaptic organization of the cortex. With the establishment of thalamo-cortical synapses there is a time of co-existence of endogenous driven activity in thalamo-SP circuits and sensory-driven activity in thalamo-cortical circuitry, before it shifts towards the permanent sensory-driven circuitry. The thalamo-cortical connectivity processes are followed by the long-range cortico-cortical connections in association and commissural fibres. These fibre axons are abundant in the SP around 24-32 GW (2). During this time they are mainly responsible for the concurrent enlargement of the SP, which can be up to four-five times thicker than the cortical plate. Their axons enter the cortical plate during 33-35 GW to branch and synapse with cortical targets in layer 2-3 (2). The last fibres to form cortico-cortical connections are the short association fibres with cortical targets in layer 2-3. This occurs in the time frame 32-47 GW (2), and thus extends into the postnatal period. The developing connectivity is outlined in Figure 1-1 (p. 13).

The developing connectivity is closely linked to the emerging gyration-sulcation of the brain. Once the axons in the SP start entering the cortical plate they branch and form multiple synapses with the targets in designated layers. The axonal branching results in peripheral expansion the subcortical white matter. The deep projection layers 5-6 contain few intra-cortical connections in contrast to their abundance in the more superficial layers. In conjunction with the tangential connections in the superficial layers, this automatically results in cortical folding. This is facilitated by increased apoptotic activity at the bottom of sulci and increased SP thickness in areas underlying gyri.

The time scale of the connectivity processes, established by histopathological studies (2), and the gyration-sulcation pattern from morphological specimen studies (10) are in good agreement. The developing connectivity in the sensory thalamic circuits coincides with the gyration-sulcation around the primary somatosensory, auditory and visual areas. Similarly, secondary gyration-sulcation coincides with connectivity of long association fibres and tertiary gyration-sulcation with the short association fibres. Consequently, the transient SP disappears, first, around 31-36 GW under primary cortical areas, and lastly in higher prefrontal association areas, where it persists up until 6 months after term (5). In fact, there is recent evidence that the reorganization of the subplate tissue components in the white/grey matter border are protracted much longer than expected, into the second year of life in areas of association cortices (11). These findings could be linked to the on-going structural changes in the cortex, with cortical thickening and in the white-matter maturation during this time.

The developing connectivity with descending projection fibres and the transient thalamo- and inter-cortical connections with the SP neurons and their projections to the cortical plate are illustrated in Figure 1-1 (p. 13).

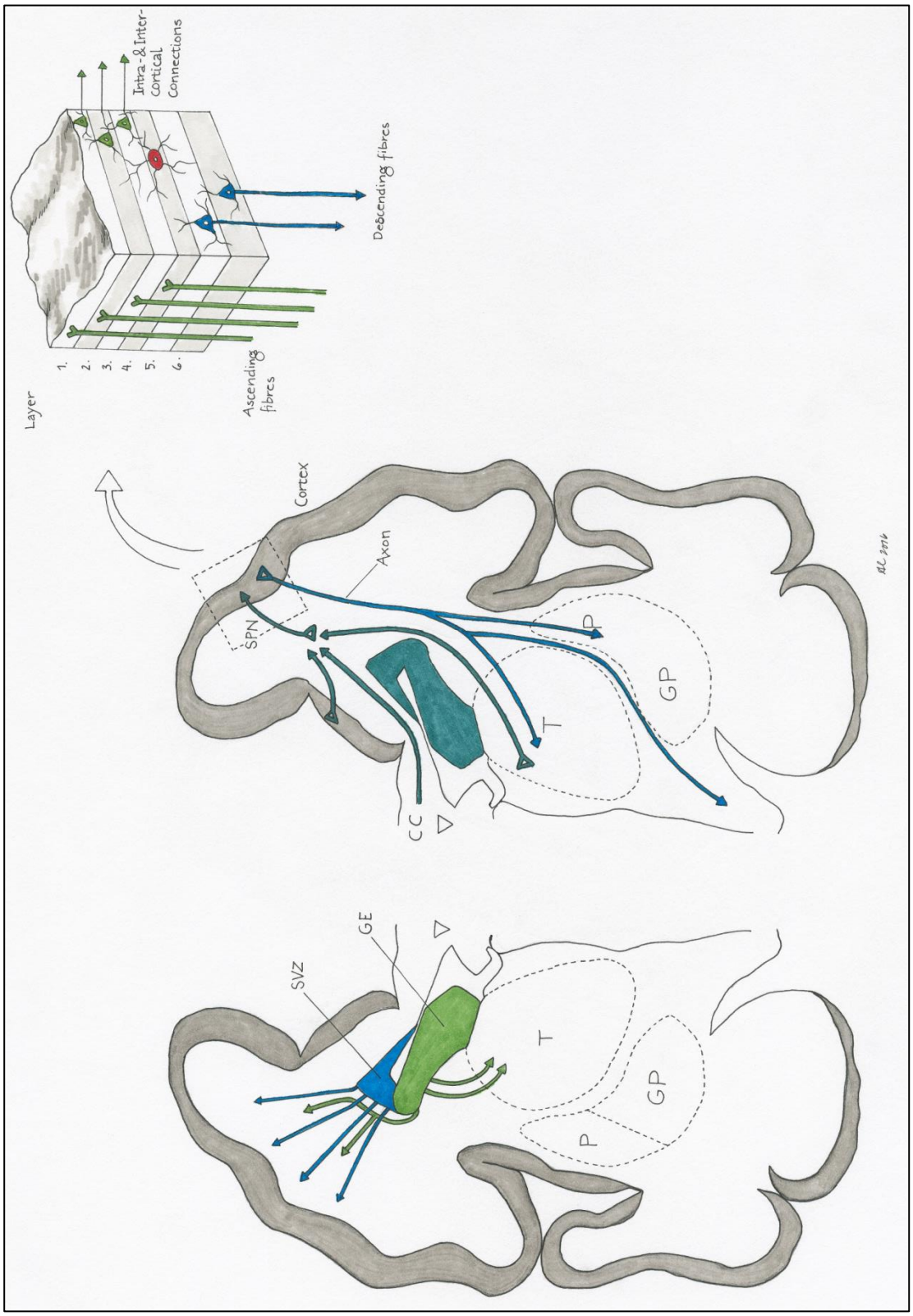

Figure 1-1: Outline of the processes (left) of neurogenesis and neuronal migration, and (right) the cortical connectivity in early brain development. The left hemisphere shows the location of the proliferative zones and the direction of migration of post-mitotic neurons from the GE and the SVZ. The right hemisphere shows the developing connectivity with axons making connections with SPN, which in turn connect with the cortical plate. Zoomed-in is an image of the cortex with its 6 layers and their in-coming and out-going axons. Note that layer 1 only has intra-cortical connections. GE=ganglionic eminence, SVZ=subventricular zone, CC=corpus callosum, T=thalamus, GP=globus pallidus, P=putamen, SPN=subplate neuron. Figure adapted from (12). Illustration by Anna-Carin Andersson.

1.1.3 Development of brain microvasculature

The developing vasculature adapts permanently to the metabolic needs of the tissue during early brain development (for a detailed review see Raybaud, 2010 (13)). The vasculature's role in early brain lesions is crucial as it provides, for destructive lesions, a final common pathway of injury. It is therefore essential to understand its development.

The early brain vasculature develops from around 8 GW to supply the proliferative zones of VZ, SVZ and GE, which contain significant capillary beds by mid-gestation. The vasculature then gradually regresses as the proliferative zones regress and disappear; the VZ around 28 GW and the GE around 34 GW.

In the periventricular white matter, in the SP and in the deep layers of the cortical plate, capillary beds emerge from around 15 GW. With the arrival of thalamic afferents to the cortical plate (around 22–27 GW), and the ensuing functional organization and synaptogenesis of the cortex, the cortical vascular bed increases steeply and continuously until week 47. The growing cortical capillary bed is thus established in an inside-out fashion from deep to more superficial layers, and follows the processes of the emerging connectivity. On the contrary, the microvascular density in the white matter is low throughout gestation.

The early venous drainage consist of venous collectors which develop to drain the capillary beds. First in proliferative zones, initially as transcerebral veins but soon (around 8 GW) the venous drainage is gradually shifted to the choroidal system (via the vein of Galen) as subependymal anastomoses develop, and the transcerebral channels regress. Cortical venous channels, draining to the brain's surface, develop later to drain the emerging cortical capillary bed and the white matter in the vicinity. These processes, again, follow the developing connectivity. Consequently, during this time there will be a gap between the deep periventricular and the superficial venous draining systems which anatomically matches (no histology studies available) the location of the SP, which eventually is drained by superficial veins (14). This will have a fundamental impact in the occurrence of periventricular haemorrhagic infarcts (PHI), which are venous congestion infarcts from upstream thrombosis in the veins draining the germinal matrix, and occur as a complication in germinal matrix haemorrhage (GMH) and intraventricular bleeding. Thus the PHI will theoretically spare the SP (see 1.2.1.2).

In general, the energy demands are relatively low in the immature brain despite the on-going intricate neurodevelopmental processes (15). This is reflected in an average cerebral blood flow of 20 ml [100 $mg^{-1} \cdot min^{-1}$] (compared with 50 ml [100 $mg^{-1} \cdot min^{-1}$] in the adult brain), only showing a slow increase after mid-gestation. However, there is a dramatic increase within the first 48 hours postnatally, which is independent of gestational age, and hence brain maturation (16). The increase in cerebral blood flow is not accompanied by any increase in cerebral blood pressure or blood volume, nor $PaCO_2$ or PaO_2. This is due to a reduced vasculature resistance, believed to be related the altered post-natal demands of the cardiopulmanory circulation (16).

1.1.4 Maturation of oligodendrocytes, microglia and astrocytes

The glial cell lineages include oligodendroctyes, astrocytes and microglia, which all have important roles in early brain development. To comprehend early brain development, an understanding of the maturation of these glial cell lineages is needed.

The oligodendrocytes have four stages of maturation in their differentiation: from oligodendroglial progenitors (OPC) to pre-oligodendrocytes to immature oligodendrocytes and finally mature, myelin-producing oligodendrocytes. The OPCs are generated from glial stem cells in the VZ, from where they migrate to their final destination in the IZ or the SP, generally following the neuronal axons, but they can also take more complex trajectories depending on their final target (17). Once in place, the OPCs start to differentiate. The OPC proliferation comes in fate-specific, sequential waves. Therefore several competing oligodendrocyte populations exist in the cerebrum. During 28-40 GW, the two intermediate stages (jointly referred to as pre-OL) are together in overwhelming dominance. They are primarily found in the periventricular white matter in the IZ, where they ensheath axons and are believed to have an important role in the developing connectivity. The first mature, myelin-producing oligodendrocytes appear around 30 GW in the IZ, and increase more diffusively in the brain after term. The myelination of the white matter fibre tracts and the basal ganglia starts in the early third trimester and in the cortex from term. The myelination processes proceed in a tract-specific pattern, with different onsets and durations, but do generally follow the pattern of connectivity and gyration-sulcation as discussed above. Overall, the gross myelination of the white matter tracts is completed by 2 years of age. Nevertheless, many fibre bundles contain both myelineated and unmyelineated axons, and there is now evidence of a dynamic, ongoing myelination processes as part of experience driven plasticity of the brain (17).

Microglia have key roles in brain development through controlling apoptosis, vascularization, axonal development and myelination. Microglia are of mesodermal origin and are found in the brain early on in development, around 6-7 GW in the VZ, and around 10 GW in the SP-cortical plate junction. Microglia become increasingly numerous in the forebrain around 16-22 GW, and reach most abundance in the early third trimester before decreasing drastically after 30 GW (18). They are especially abundant in the periventricular areas, the crossroads of major white matter fibre tracts, and in the IZ-SP junction, suggesting an active role in axonal guidance, removing superfluous axons and providing trophic factors.

Astrocytes are glial cells with a wide-range of functions and are abundant in the brain. The astroglial proliferation is largest from the second half of gestation. They play important roles in early brain development during the late neuronal migration, in axon guidance, in synaptic development and in myelination (19). They are also key cells in the brain lymphatic system (20). However, the exact role of astrocytes in early brain development is in general not yet fully understood.

1.1.5 Development of the motor system

The first system studied in this thesis is the motor system. The motor system is the neuronal system involved in the control of movement (21). It is a highly integrated system, involving the central and peripheral nervous system for execution and sensory feedback for control.

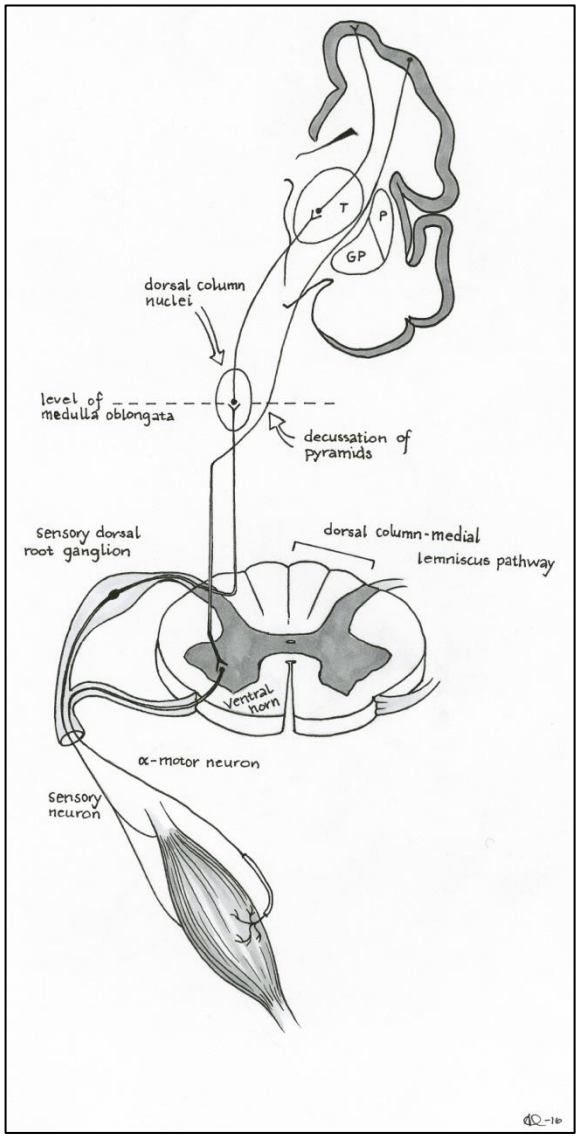

Figure 1-2: The corticospinal system. The upper motor neuron synapse with the lower α-motor neuron in the spinal cord. Sensory neurons from the muscle have their cell bodies in the dorsal root ganglion and project to the dorsal column nuclei in the medulla oblongata. These project to the thalamus, which in turn project to the cortex. This makes an integrated feedback-control system. Illustration by Anna-Carin Andersson.

The motor system can be divided into four, highly interactive, subsystems (21). First, the descending motor system, containing the upper motor neurons in the motor cortex responsible for planning, initiation and voluntary muscle movement, along with the brain stem centres responsible for basic movement and posture control. The upper motor neurons project to the second, subcerebral subsystem, located in the spinal cord and brain stem. This subsystem consists of the pool of α-motor neurons in the spinal cord's ventral horns and brain stem nuclei, which project to the skeletal muscles, and local interneurons for segmental circuitry control, which receive additional input from sensory afferents. The third and fourth subsystems are the basal ganglia in the lower part of the forebrain and the cerebellum respectively. The basal ganglia are responsible for gating and proper initiation of the upper motor neuron. The cerebellum is responsible for sensory-motor coordination of on-going movements.

This thesis focuses on the corticospinal system, which is the integrated circuitry of the descending cortico-spinal tract (i.e. descending upper motor neurons projecting to spinal cord), the ascending spino-thalamic afferents (i.e. segmental sensory neurons project to dorsal column nuclei which project to the thalamus) and the thalamo-cortical afferents. The corticospinal system thus consists of the first and second subsystems of the motor system described above (Figure 1-2). The corticospinal system is of particular interest in early brain lesions as it is frequently affected by injury, specifically the cortico-spinal tract and the thalamo-cortical projections. Understanding the development of the corticospinal system is therefore important in the context of early brain lesions and will be outlined in the following section.

As described in the previous chapter 1.1.2, already early in gestation the deepest cortical layer 6 is connected with the basal ganglia and thalamus. The axons from projecting upper motor neurons (the pyramidal cells in layer 5) are found in the cervical medulla by 17-18 GW (8), but still only in the white matter and they have not yet synapsed with the α-motor neurons in the ventral horn. The ascending spino-thalamic pathways are also established with the dorsal root neurons projecting to dorsal column nuclei, which in turn project to the thalamus. By this time, local functional circuits exist, both on a segmental level in the spinal cord (α-motor neuron → muscle → sensory neuron → spinal cord interneuron → α-motor neuron) and in the forebrain (thalamus ↔ subplate neuron). However, it is not until the arrival of the thalamo-cortical afferents into the cortical plate (layer 4), that upper motor neurons start to invade the spinal cord grey matter and synapse with the α-motor neuron pool. Thus, the complete integration of the corticospinal system occurs first once the thalamo-cortical connections are established (24-32 GW) (2).

The early integrated corticospinal system consists, therefore, of both the transient thalamo-subplate connections, with endogenous spontaneous firing, and the sensory driven thalamo-cortical connections (2,9). This functional integration with early endogenous activity is believed, as in the visual system 1.1.6, to be important for the early cortical organization. The connectivity processes also coincide with the development of fetal movements (15). By the time of the establishment of the corticospinal system, the cortico-spinal projection pattern is more extensive than in maturity, and descending motor neurons have terminations on both sides of the mid-line in the spinal cord (22), i.e. the upper motor neurons in the ipsilateral cortex project to both the contra- and ipsilateral sides in the spinal cord.

Further development of the corticospinal system occurs in post-natal life and involves refinement of the cortico-spinal projections, the neuro-muscular unit and the dorsal root neuron projections to the dorsal column nuclei. This is driven by cortical activity in the cortical motor areas and by limb use (22). Transcranial magnetic stimulation (TMS) studies suggest that aberrant ipsilateral cortico-spinal projections are withdrawn during the first two years of development from synaptic competition (23), but can be retained in cases of early injury (24), as discussed in 1.4.1.

1.1.6 Development of the visual system

The second system studied in this thesis is the visual system. The visual system is by far the most advanced of the sensory systems in the human body (21). The development of the visual system has been studied extensively, and findings have revealed many fundamental neurobiological principles. Its organisation and development are important in early brain lesions and will be described briefly.

The visual system consists of a highly specialized optical organ (the eye) for refraction and detection of light stimulus on the retina. The conversion of light (photon) energy in the retinal photoreceptors to electrical signals are refined in retinal circuits and, thereafter, transmitted from the eye by the retinal ganglion cells (RGC) in their axons in the optic nerves. The RGCs

primarily project to the lateral geniculate nuclei (LGN) in the thalami, but also to other targets for visual integration with cerebral functions. These include the suprachiasmatic nucleus in the hypothalamus (the retino-hypothalamic pathway) for circadian regulation of bodily processes, and several nuclei in the mesencephalic superior colliculi for coordination of head and eye movements to visual targets. The neurons in the LGN project, in turn, to the primary visual cortex (V1), or striate cortex, in the medial occipital lobe around the calcarine sulcus. V1 is connected via short-association fibres (layer 2-3), with higher order visual areas (V2-V5) for further processing of visual information, but has also projections to the LGN (from layer 6) and to the superior colliculus (from layer 5). The extrastriate cortices are located around the V1, either in an occipito-parietal direction (the "dorsal stream") or an occipito-temporal direction (the "ventral stream"). The dorsal stream is largely responsible for object location and motion and, in relation to this, integration with other cerebral functions via the parietal association cortex. These include visually guided movements, (e.g. to lift the foot to avoid tripping when stepping onto the pavement or for precision in hand gripping). Visuo-motor integration is often affected in cerebral palsy (25). The ventral stream is responsible for form and object recognition and visual memory processing, and has connections with the hippocampus.

A key feature of the visual system which is particularly relevant to this thesis, is that the retinotopic organization (i.e. a point-to-point representation of the visual field (VF) on the retina) is maintained throughout the lower-order visual areas. This means that there is an overall topographic organization of the VF along the visual pathways; i.e. in the optic nerves, the optic tracts, the LGN, the optic radiations (OR) and in the visual cortex (26). Consequently, injuries along the visual pathways will result in predictable VF defects (21). Therefore, topographic representation of the VF is a key element when considering the injuries to the immature OR. To achieve a continuous retinotopic map in the visual system, the following structural features are pivotal: the temporal retina (lateral aspect of the retina) projects to the ipsilateral LGN and the nasal retina (medial aspect of the retina) projects to the contralateral LGN by crossing the midline in the optic chiasm (21). The projections from each eye, the retino-geniculate projections, are segregated into six distinct monocular layers in LGN (i.e. layers receiving input from one eye only) (21), and the retinotopic map is maintained for all layers. This monocular separation is also preserved in the primary visual cortex as the bulk of the LGN neurons terminate in eye-specific alternating (0.5 mm wide), so-called ocular dominance columns (ODC) within layer 4 (specifically layer 4A and 4C) in the striate cortex (21). However, most neurons outside of layer 4, but connected to layer 4 with intra-cortical interneurons, are binocular, and hence the output to extrastriate areas (from layers 2-3) is binocular but maintains a continuous retinotopic visual field map (21,27).

In this thesis, the visual system has been studied in individuals with white matter damage of immaturity (WMDI). Periventricular WMDI can involve the OR and result in VF defects, commonly as bilateral homonymous inferior quadrantdysopias. The representation of the lower (inferior) and upper (superior) VF in the OR is key to understanding the structure-function relationship between injury and VF defect, and is outlined in Figure 1-3 (p. 19).

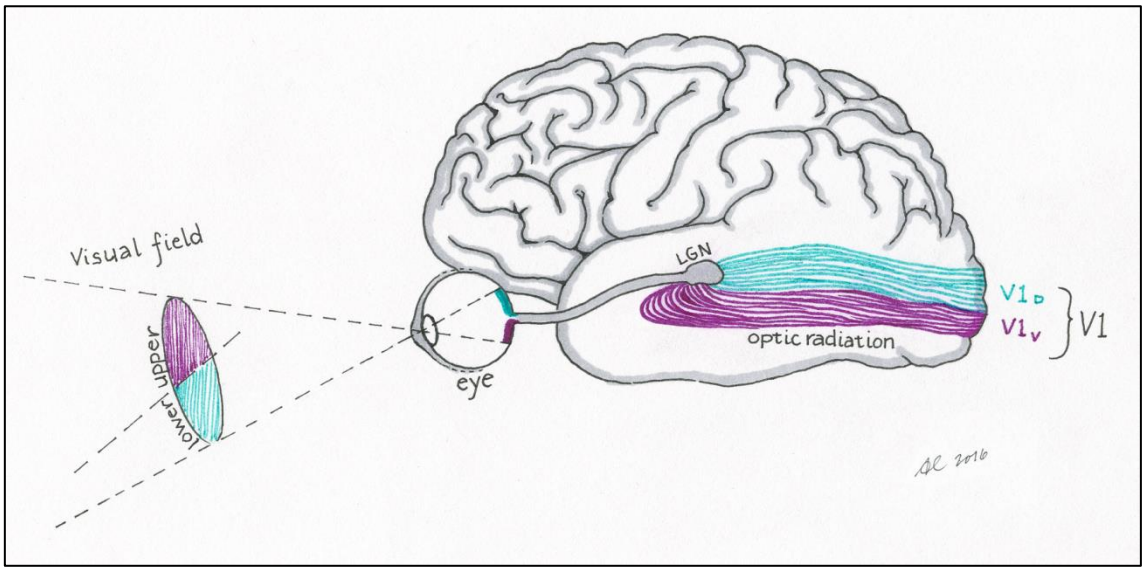

Figure 1-3: Representation of the upper (purple) and lower (turquoise) visual field on the retina, in the optic radiation and in the primary visual cortex,V1. Note that the drawing is simplified and does not show how the right and left hemifields (i.e. hemifields separated by the vertical meridian) are represented on the retina and in the contralateral hemispheres respectively. $V1_{D/V}$ = dorsal (turquoise) /ventral (purple) parts of V1. LGN=lateral geniculate nucleus. Illustration by Anna-Carin Andersson.

To develop the visual system to such a high level of complexity requires an intricate interplay between pre-programmed genetic processes and activity-dependent processes. Key elements for the organization of the visual system are the aggregation of the RGC projections into eye-specific layers in the LGN and eye-specific ODC in the V1. This is largely achieved by the preservation of the retinotopic map (28). The first RGC projections to the LGN have a crude retinotopic organization, but axons from both eyes are intermixed over a large portion of the LGN (28). These early retino-geniculate synapses are capable of synaptic transmission and the initial segregation into specific monocular layers results from a competitive interaction of retinal input from both eyes. It includes cellular apoptosis as well as synaptic re-modulation, and the bulk of the synaptic pruning in LGN occurs before mid-gestation (6). It has been linked to retinotopically coordinated, spontaneuous waves of firing in the RGCs over the retina (28). Similarly, the initial LGN projections to V1 (layer 4) also have a crude retinotopic map, but are intermixed. The refinement into eye-specific ODC is also activity-dependent, primarily from sensory driven activity, i.e. with the advent of visually evoked potentials after the opening of the eyes (29). The retino-cortical connections are hereby refined, strengthened and stabilized, and an adult-like pattern is essentially established at time of normal birth (30). Thereafter, visual stimulus further nurtures the cortical development and maturation of the retino-cortical structural organization (31). Importantly, the segregation of axons into eye-specific layers in the LGN precedes the cortical arrangement into ODC, and is presumably a requirement for achieving this particular organization in the striate cortex (32).

1.2 INJURIES DURING EARLY BRAIN DEVELOPMENT

Disturbances or injuries to the brain during early development cause different types of structural abnormalities depending mainly on the stage of maturation of the brain at the time of the insult (3) and have equivalents on neuroimaging (33).

Brain development can be viewed, as described in 1.1, as a series of separate but overlapping developmental stages. A disturbance or injury to the brain will cause both primary effects and secondary effects from maturational or trophic disturbances. Hence, neither the full extent nor the full consequences of the insult are possible to fully assess initially on neuroimaging. Importantly, three different groups of general lesion patterns can be seen on magnetic resonance imaging (MRI) in early brain injuries (33). These lesion patterns can be linked to the distinctive but overlapping stages in the early brain development, and are related to the different vulnerability of the developing brain at each stage. These three basic lesion patterns will now be described in some detail.

1.2.1 Patterns of brain abnormalities and lesions during early brain development

1.2.1.1 1st and 2nd trimester (< 24 GW)

Disturbances or injuries to brain development during the 1st and 2nd trimester, i.e. during the period dominated by neurogenesis, result in malformation of cortical development and of the midbrain-hindbrain (3), and can be classified on MRI (34,35). Malformations of cortical development can be classified into three principal categories: as malformations of abnormal proliferation and apoptosis; of abnormal neuronal migration; or of abnormal cortical organization (35,36). These categories represent the three consecutive and overlapping developmental stages: the neurogenesis in the germinal matrix; the migration of the post-mitotic neurons; and the laminar organization of the cerebral cortex. Malformations of cortical development are predominantly congenital, and an increasing number of genetic mutations have been linked with specific malformations (35). However, both the clinical and the neuroimaging phenotype can vary substantially despite mutations in the same gene. Conversely, the phenotype may be similar despite mutations in different genes. This leads to the conclusion that the genetic penetrance varies, and may depend on environmental factors. Mutations can be germ line mutations, shared by all the cells in the body, or *de-novo* mutations, which may only affect certain cell lineages and/or only appear in certain locations. Such mutations are called mosaic mutations, and their penetration is in general much less severe than germ line mutations. This also explains the geographical focus that certain malformations show. Mutations that are X-linked show, naturally, greater penetration in males. Malformations of cortical development are frequently part of more complex syndromes.

Malformation of abnormal proliferation and apoptosis concerns the neurogenesis of the populations of post-mitotic neurons and glial cells generated in the proliferative zones. These processes are tightly regulated to decide fate determination and differentiation of the progenitor cell lines, as well as their mitotic activity to control the neuron number (1,4). Insight into the role of apoptosis, or programmed cell death, in controlling these processes has been gained in the last few decades (37). Disturbances or lesions affecting the neurogenesis cause malformation of cortical development, and are subcategorized by either abnormalities of brain size, i.e. conditions of micro- or macroencephaly, or abnormal proliferation with abnormal cells

(35). Malformations in the second subcategory frequently cause epilepsy, and are further subcategorized according to whether the abnormal cells are non-neoplastic or neoplastic.

Malformation of abnormal migration is subcategorized into the lissencephalies/subcortical band heterotopia spectrum, the cobblestone complex and heterotopias (35). A major difference between the first two is that in the lissencephalies, the neurons have not reached the cortical plate, whereas in the cobblestone complex, many of the migrating neurons migrate too far, into the subpial space. This is further elucidated by the fact that the wealth of the genetic mutations that have now been linked to different malformations of abnormal migration mainly concern cellular functions of movement and adhesion.

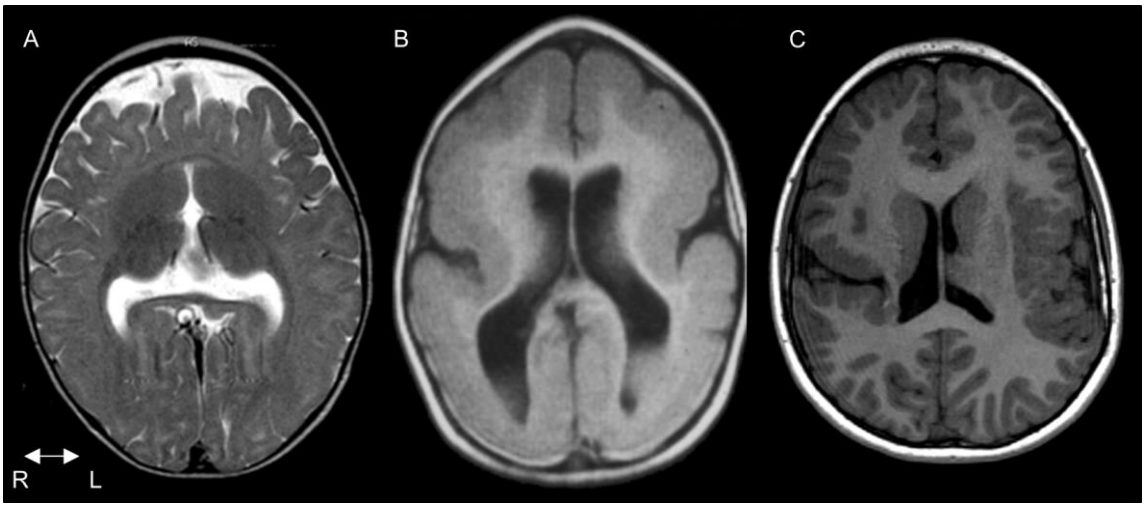

Figure 1-4: Examples of malformations of cortical development. (A) Lobar holoprosencephaly is a result of an incomplete separation of the cerebral hemispheres, in this case the frontal lobes, which occurs early in gestation. (B) Lissencephaly, here with smooth, thick cortex (agyria and pachygyria), is a malformation of abnormal neuronal migration. (C) Polymicrogyria, here bilateral perisylvian polymicrogyria with an open-lip schizencephaly on the right side, is a malformation of abnormal cortical organization and late migration. R=right, L=left.

Malformation of abnormal cortical organization concerns the developing cortical organization from the processes of synaptogenesis, neurite extension and neuronal maturation, but also includes the late neurogenesis and migration. Malformations of abnormal cortical organization are characterized by polymicrogyria (35). Polymicrogyria mainly affects the deeper layers of the cerebral cortex and, as a consequence, an abnormally involuted cortex with multiple small gyri develops (38). Polymicrogyria is typically subclassified in relation to the affected cortical areas, e.g. perisylvian polymicrogyria, and can be uni- (40 %) or bilateral (60 %) (38). The polymicrogyric cortex can be in continuum with the ventricular ependyme, in which case it is called a schizencephaly. In schizencephaly the abnormal cortex constitutes a cleft into the ventricular surface. Schizencephaly can be isolated or occur in combination with polymicrogyria in other locations. Polymicrogyra or schizencephaly are part of many congenital developmental disorder syndromes, and several polymicrogyria patterns have been linked with genetic abnormalities or genetic mutations (35,38). Polymicrogyria can also result from prenatal ischemia (39) or infection (40) in the latter part of the second trimester. In fact, isolated schizencephaly may be caused by focal ischemic infarct affecting the germinal matrix (41,42). Recently questions have been raised as to whether polymicrogyria, in fact, constitutes a more heterogeneous group of malformations than previously believed (35,38).

Three examples of malformations of cortical development can be seen in Figure 1-4 (p. 21).

1.2.1.2 Early 3rd trimester (24 – 34 GW)

Brain development in the early third trimester is dominated by the developing connectivity, especially thalamo-cortical and long-range cortico-cortical connections (2). There is on-going neurogenesis of GABA-ergic interneurons (1), and the oligodendrocytes and microglia are active, with key roles in the axonal development and myelination. The main triggers of injury are ischemia and inflammation, which often co-exist and can potentiate each other (12), and the result is a downstream pro-inflammatory cascade of excessive cytokine production, excitotoxic glutamate release and oxidative stress, with free-radical release mediated by activated microglia (12). Particularly at risk for injury is the premature newborn, in whom transient hypoxic/ischemic events, as well as inflammatory/infectious episodes, are common due to the immature cerebral autoregulation of cerebral blood flow and the primitive protective barriers in the skin and gut in combination with the immature immune system (43).

Injuries to the brain during the early third trimester are commonly referred to as white-matter damage of immaturity (WMDI) (44) as they can occur both in utero and in the premature newborn. The most frequent injury seen in WMDI is injury to the periventricular white matter. This can be in the form of periventricular leukomalacia (PVL) (45,46). The term PVL has, over the years, been misused and also used to describe white matter lesions occurring at later developmental stages. Therefore, the term WMDI will be used instead wherever possible, to avoid confusion. Germinal matrix haemorrhage (GMH), either complicated by intraventricular haemorrhage (IVH) and/or periventricular haemorrhagic infarcts (PHI), and punctate lesions in the periventricular white matter are more rare, but remain parts of the lesional spectrum included in WMDI (8). The periventricular zones in the peritrigonal area, the frontal horns and the area around the foramen Monroi constitute watershed areas of the deep cerebral white matter, and are sensitive to hypoxic/ischemic events (47). This might explain why we observe a predilection of WMDI in these localization (47), which is also seen on imaging (44,48). In order to understand WMDI, the vulnerability of different cell types in the developing brain during the early third trimester has to be considered, as well as the consequential results of injury. In the following section, the vulnerability of the cell lineages will be discussed, followed by the different lesion entities in the WMDI spectrum. Punctate lesions in WMDI will not be discussed further. Their origin is debated, though not ischemic, and their impact on neurodevelopment is unclear, although if extensive they can leave areas of hypomyelination (8).

The oligodendrocyte cell lineage are in active development during 24-40 GW (49). Immature stages of oligendrocytes (Pre-OLs) are especially vulnerable to insults of ischemia and inflammation, and to the downstream mechanisms of microglial activation with cytokine release, exitotoxicity and free radical attack (49,50). Populations of pre-OLs dominate the cerebrum during the early third trimester, and are specifically abundant in the periventricular WM during 24-32 GW (51). The pre-OL population thus constitutes the major target of injury in this time period (49,52). Upon insult there will be a decrease in the pre-OL population which

in time is counteracted by an increase in oligodendroglial progenitors which, however, lack the ability to mature into myelin-producing oligodendrocytes (53). Hence, the result of injury to the pre-OL population is a combination of hypomyelination and detrimental effect on axonal development (both afferents and efferent axons), which in turn effects both cortical and thalamic development (12,52). With the onset of myelination in the periventricular white matter from around 30 GW, the pre-OL populations are gradually replaced by mature, myelinproducing oligodendrocytes, and consequently risk of pre-OL injury dramatically decreases. This coincides with the decrease in occurrence of PVL from around 32 GW (51).

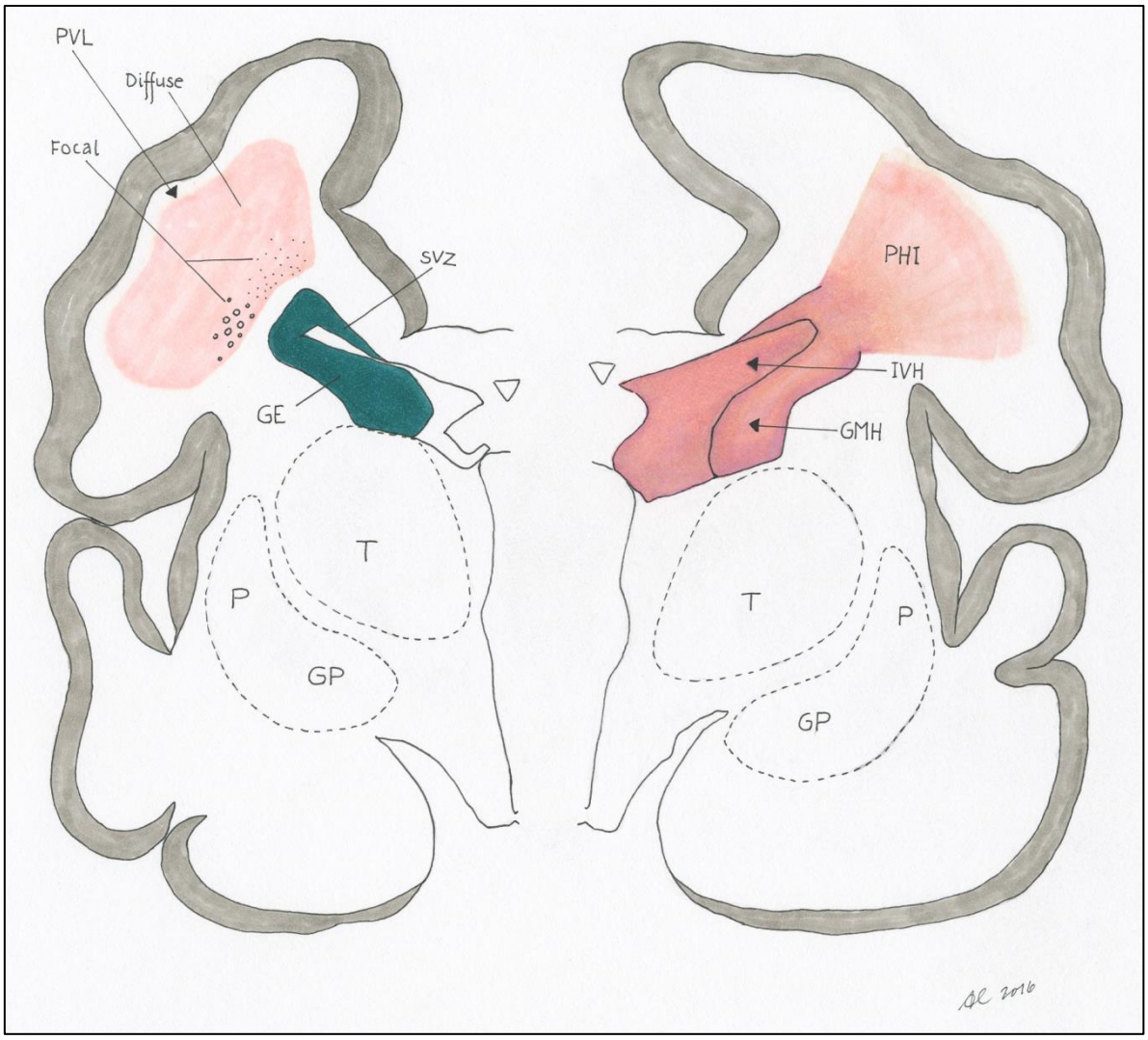

Figure 1-5: Typical locations of WMDI illustrated in two hemispheres. The left hemisphere shows focal PVL, either cystic (circles) or non-cystic (dots) in the deep periventricular WM and diffuse PVL, extending into the subcortical WM. The right hemisphere shows GMH, which can bleed into the ventricle causing IVH, and, in most severe cases, a PHI with destruction of both the SVZ and the deep periventricular WM. GE=ganglionic eminence, SVZ=subventricular zone, PVL=periventricular leukomalacia, GMH=germinal matrix haemorrhage, IVH=intraventricular haemorrhage, PHI=periventricular haemorrhagic infarct, CC=corpus callosum, T=thalamus, GP=globus pallidus, P=putamen. Figure adapted from (12). Illustration by Anna-Carin Andersson.

Axonal and neuronal injury are increasingly recognized, and are more frequent injuries than previously thought in WMDI (12,54). In both cases, it is hard to distinguish primary from secondary injuries. Primary axonal injuries from destructive WMDI, such as necrotic foci in cystic PVL, are evident from neuropathological findings (45), however, recent studies have

also shown more widespread axonal injuries in diffuse WMDI showing increased levels of the apoptopic marker fractin in axons in gliotic tissue (54,55). Again, the injuries may still be primary or secondary. Axonal injuries also cause degeneration of the ensheathing pre-OLs, resulting in hypomyelination (53). Cerebral white matter axons are in rapid development during the early third trimester, and an injury, focal or widespread, results in white matter loss with impact on the cortical and thalamic development. Neuropathology studies have also shown neuronal loss and/or gliosis in the thalamus and in the basal ganglia (56), with a clear relation to PVL, but again no studies can say whether these injuries are primary or secondary. In the study by Pierson et al (56), the thalamic injuries were found to be primary and secondary, with both anterograde and retrograde neurodegeneration. Hence, injuries would cause thalamic degeneration and secondary axonal injuries with effects on cortical development and hypomyelination via pre-OL destruction. SP interneurons are vulnerable to hypoxia-ischemia (57), and there is evidence of injury to the SP in PVL (58,59). This transient structure peaks during the early third trimester, and is pivotal for both cortical and deep nuclei development. An injury will therefore have extensive secondary effects. Again, injury to the afferent axons effect both cortical and thalamic development, whereas injury to the efferent axons would affect cortical development and their targets. Both cause hypomyelination. Further, the SP interneurons are important in creating the first functional circuits between cortical plate and its periphery, and if this is compromised there could be detrimental effects on the development of functional brain circuitry.

WMDI in the form of PVL occurs as a focal necrotic PVL, cystic or non-cystic, in the deep periventricular WM, and more diffuse gliosis in the subcortical WM without necrosis (43). WMDI is often bilateral or asymmetrically bilateral, although unilateral injury can occur. Focal PVL consists of destructive necrosis to all cellular elements (45), whereas in focal non-cystic PVL the microscopic necrosis often turn into glial scars rather than cysts. Both focal cystic and focal non-cystic PVL often have diffuse perifocal gliosis. The distribution of focal PVL has a predilection to the anterior and posterior ventricular horns (47), with more widespread involvement in younger premature neonates (54,60). Cystic WMDI is relatively rare today, being observed in less than 5 % of infants with very-low birth weight (< 1500 g) (8,61), but associated with adverse neurological outcome, related to the extent of the cysts (48). The diffuse PVL accounts for the majority of cases with WMDI (43), and is characterized by astro- and microgliosis and an initial decrease in pre-OL followed by compensatory increase in oligodendrocyte progenitors (53). However, the oligodendrocyte progenitors lack the ability to differentiate into mature oligodendrocytes, resulting in hypomyelination and loss of parenchymal volume with secondary ventricular dilatation. The PVL spectrum is believed to be a continuum from the most severe form of cystic PVL, to focal non-cystic to diffuse white-matter gliosis. Not surprisingly, activated microglia are found in the periventricular region in non-cystic PVL (62). WMDI is often accompanied with neuronal/axonal injuries affecting the cerebral and cerebellar white and grey matter, as described above (12).

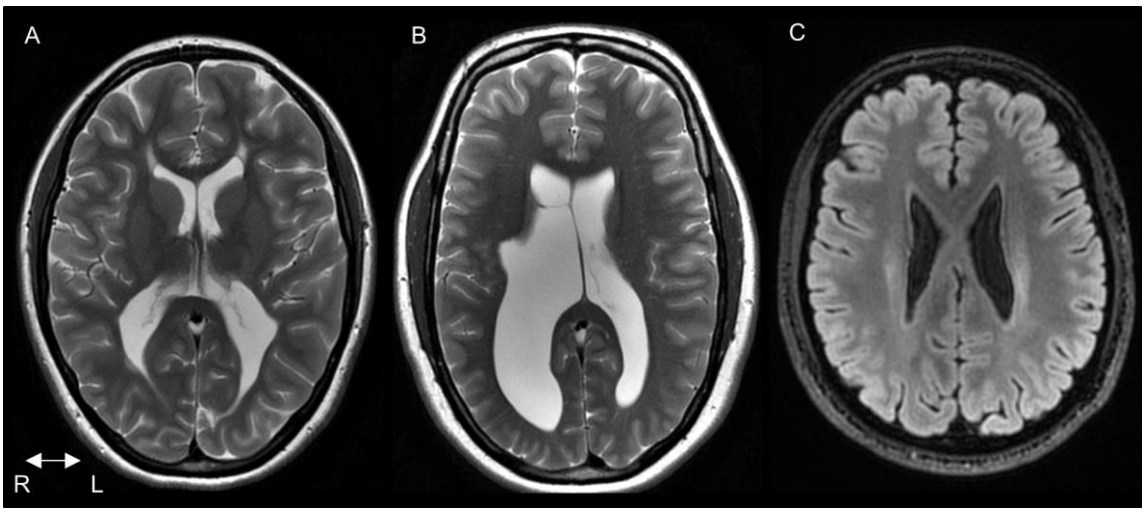

Figure 1-6: Examples of lesions occurring during the early 3rd trimester causing WMDI. (A) Bilateral WMDI with extensive reduction of and gliosis in the periventricular WM, most pronounced in the posterior WM. (B) Bilateral WMDI with extensive reduction of the middle and posterior white matter, especially on the right side. A porencephlic cyst from an earlier PHI is seen in the region of right foramen of Monroi. Only subtle gliosis in the right middle periventricular white matter (not seen in this axial section). (C) Bilateral WMDI with minor reduction of the left middle and left posterior periventricular white matter and discrete bilateral gliosis. R=right, L=left.

Germinal matrix haemorrhage (GMH) is a bleeding in the subependymal veins, draining the germinal matrix (63). It may be uni- or bilateral. The precise mechanism for the GMH is not fully understood, but it is evident that the aetiology is multifactorial and primarily attributed to the fragility of the germinal matrix microvasculature. This is particularly sensitive to hypoxia/ischemia (64), as the germinal matrix is in a state of involution. Up until term the subependymal veins lack collagen fibres, and contain a single layer of endothelial cells with weak basal lamina. This immaturity makes them at risk of rupture. GMH is most frequent in the first 48 hours in the premature neonate, and the risk of haemorrhage is increased with more severe prematurity and lower birth weight (8). The primary effect of the GMH is on the proliferation zones, GE and SVZ, the former in particular with decreased generation of GABA-ergic interneurons, which may cause secondary effects on cortical and thalamic development. However, isolated GMHs are often seen in early brain imaging and are believed not to have any larger impact on neurodevelopment. When the GMH is large, it may break through the ventricular ependymal, and results in an IVH which can be complicated by ventriculomegaly and hydrocephalus. The GMH-IVH can also progress further to cause an upstream thrombosis and haemorrhage in the afferent medullary venous tributaries, resulting in a periventricular haemorrhagic infarct (PHI). The major destructive focal effects in GMH-IVH with PHI comes from the PHI, which destroys the dorsal SVZ and overlying periventricular white matter, including pre-OLs and axons. This causes a destructive cystic lesion, a porencephalic cyst. The thin membrane separating the porencephalic cyst from the ventricle is often defective, and it may break down completely, causing the cyst to become part of the ventricle and lined with ependyma. As with PVL (47), PHI is mainly located in the deep frontal and occipital watershed zones (65), from observation prevalent around the foramen of Monroi. GMH/IVH, with our without PHI, can occur in combination with PVL. The axonal and pre-OL injuries may result in secondary effects on cortical and thalamic development and myelination (12). Deep venous injuries appear to spare the SP (8), which may be

beneficial for cortical development and neurodevelopmental outcome as discussed above (see 1.1.2). Therefore, the overall neurological deficits may be less severe (66), and even focal deficits are less severe than expected from conventional anatomy. This may be a result of increased plasticity due to the intact SP zone (67). The intact SP may also explain the often normally convoluted overlying cortex. Despite the fact that the injury occurred before this process started and at a time when the cortical surface was smooth (8).

Typical locations of WMDI are illustrated in Figure 1-5 (p. 23), and three examples of MRI of WMDI are shown in Figure 1-6 (p. 25).

1.2.1.3 Late 3rd trimester (> 34 GW)

During the late third trimester, the cortical development is active in the superficial layers. The connectivity processes here involve extensive synaptogenesis between cortical neurons and afferent axons. These processes are energy-consuming, and the superficial layers have at this point become richly vascularized (13). Likewise, the vasculature in the germinal matrix has regressed as the proliferative zones have regressed. As a consequence, at this point in time the brain vasculature has reached an overall adult pattern. This includes arterial blood supply to the forebrain from the three major cerebral arteries with their characteristic watershed zones, blood supply to the central subcortical structures from perforating end-arteries, and the blood supply to the brainstem and hindbrain from the vertebro-basilary system. The glial cell lineages have reached a greater degree of maturity and are not excessively vulnerable anymore. Injuries in the late third trimester effect predominantly the cortical and subcortical grey matter. They are primarily of vascular origin, and can be divided into global hypoxic-ischemic injury and focal ischemic infarcts.

Hypoxic-ischemic injury (HI) is caused by a global hypoxic/ischemic event and can be acute or prolonged, deep or partial. Examples include prolapse of the umbilical cord, rupture of the uterus or abruption of the placenta, or placenta insufficiency for prolonged, partial ischemia. In the late 3rd trimester, the basal ganglia, thalamus and the cortical peri-rolandic/central regions have the highest glucose metabolism (68). They are therefore the most sensitive structures to HI. The severity of the insult and the severity of the clinical symptoms, as well as the subsequent motor outcome, have been related to injury patterns on neonatal MRI (69,70). The mildest pattern includes injuries in the adjacent structures of the ventro-lateral thalamus and the posterior third of putamen, which is a part lentiform nucleus (one example in Figure 1-7, p. 27). In the intermediate injury pattern, cortical ischemic injuries are also seen in the peri-rolandic/central areas. The most severe pattern also includes hippocampal injuries, as well as injuries to the entire thalamus. In contrast to acute asphyxia, the fetus/baby can experience a prolonged asphyxia of varying degrees. The lesion patterns are necrotic injuries to parasagittal watershed areas (43). The damage is often bilateral but not necessarily symmetric. The extent of the injuries can range from mild watershed infarcts (one example in Figure 1-7, p. 27), to severe end-stage multicystic encephalopathy with extensive necrotic injuries in larger parts of the hemispheres.

Focal infarcts are caused by an impaired or ceased blood flow in a major cerebral artery, resulting in a downstream hypo-perfusion of the brain parenchyma of the vascular territory. Focal ischemic infarcts in fetal life up until postnatal day 28 are referred as perinatal ischemic stroke (PAS) (71). The incidence of PAS is around 1 in 2300 newborns (72). Perinatal ischemic stroke is caused by a local thrombosis or by embolism from extracranial sites, such as vessels, the heart, umbilical vein or the placenta (43). The pathogenesis of PAS is complicated and multifactorial, and includes factors that affect the placental and brain vasculature, their haemostatic mechanisms, as well as the coagulatory states of the fetus and the mother (71). This is illustrated by the fact that the pro-coagulatory state in pregnancy is further up-regulated around birth. Likewise, thrombophilias in the mother or child are risk factors for PAS. All neonates have a high haematocrit, which is protective but can, in cases of coagulopathy, cause thromboembolism at birth. The major affected vessel is the middle cerebral artery (MCA) (one example in Figure 1-7), with dominance on the left side, though all major intracranial vessels can be affected. The left-side preference in MCA-infarcts is thought to be due to the fetal circulation, where e.g. the bidirectional flow in aorta can in combination with a (still) patent ductus arteriosus cause emboli in the thoracic vessels to go over the aorta and reach the intracranial vessels. It has been suggested that an early focal infarct, in utero, may be the cause of a focal injury like schizencephaly by infarction of the germinal matrix (42). Perinatal ischemic stroke in the early third trimester causes WMDI, with characteristic vascular distribution often showing extensive white matter damage with pronounced effects to cortical and thalamic development.

Three examples of early brain lesions of vascular origin in the late third trimester are shown in Figure 1-7.

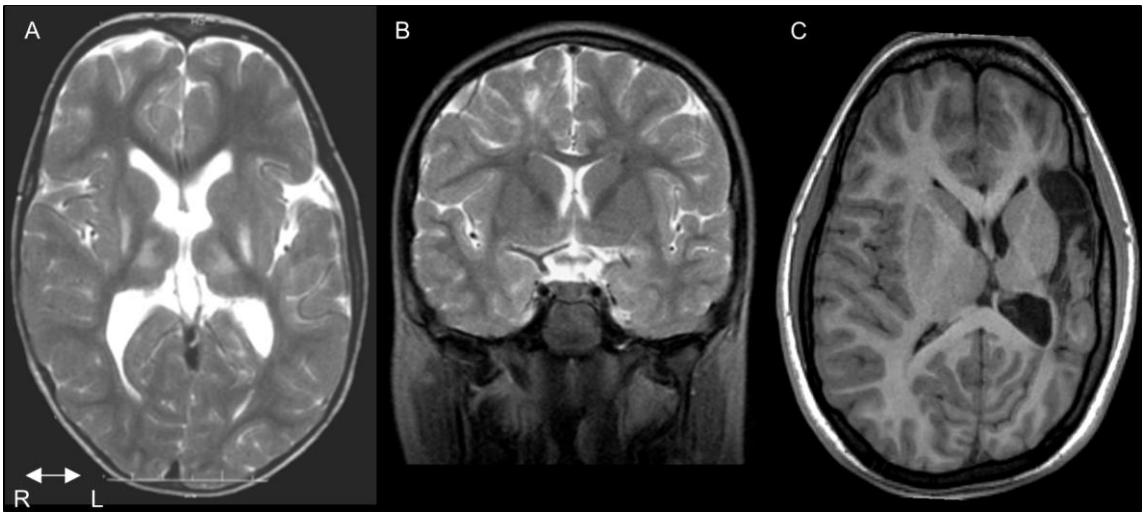

Figure 1-7: Examples of lesions occurring during the late 3rd trimester causing, pre-dominantly, cortical and subcortical GM lesions. (A) Bilateral lesions in the postero-lateral lentiform nuclei and ventro-lateral thalami from acute, profound asphyxia. (B) Watershed infarct affecting the subcortical WM in the right superior frontal gyrus from prolonged, partial asphyxia. (C) Focal infarct in the territory of the left middle cerebral artery with extensive damage to the left cerebral hemisphere. Note the small left hemicranium.

1.2.2 Clinical presentation of early brain lesions

1.2.2.1 Cerebral palsy

Cerebral Palsy (CP) is a persistent disorder of movement and posture caused by non-progressive lesions of the immature brain (73). CP is often accompanied by disturbances of sensation (including hearing and vision), perception, cognition, communication and behaviour. Epilepsy and secondary musculoskeletal problems are also common (73).

The prevalence of CP in the Western world is stable, around 2-3 per 1000 live births (44,74), although recent data indicates that the overall prevalence of CP within Europe is decreasing (75). About 50 % of CP cases occur in children with normal birth weight. Children born preterm or with moderately low (< 2500 g) or very low birth weight (< 1500 g) are at increased risk of CP, and the risk in the preterm group is highest for those born with extremely low birth weight (< 1000 g). The overall decrease in CP prevalence is likely to be due to the decrease of CP prevalence in the moderately and very low birth weight group (75).

A widely accepted classification of CP types has been proposed by the Surveillance of Cerebral Palsy group, SCPE (http://www.scpenetwork.eu). In this classification system, CP is classified into spastic, dyskinetic (dystonic or choreo-athetotic) or ataxic CP, according to the predominant neurological signs. Spastic CP is the dominating form (around 80 %), and is further sub-classified into unilateral (30 %) and bilateral (50 %) CP.

In this thesis, unilateral spastic CP has been studied. The hand function is always affected in unilateral CP, although to varying degrees, ranging from clumsiness to difficulty performing voluntary motion. This includes various aspects of hand function, including, for example, coordination (76), scaling of grip forces (77) and impaired sensory function (78). The individuals often have a tendency to only use their good hand, however, bimanual manipulation is required in many everyday situations (e.g. pulling up a zipper), and poor bimanual performance is a common functional limitation. Classification systems are suggested to describe the hand motor function abilities for the individual (73). These include the Manual Ability Classification System (MACS) (79) to assess hand and arm function. Various timed tests have also been developed to quantify the hand motor function, including the Box & Block test (80) to measure gross manual dexterity, which is used in this thesis and is described in 3.4.1.

1.2.2.2 Cerebral visual impairment

The spectrum of visual impairment caused by early brain lesions includes subnormal visual acuity, restriction of visual fields (VF) (81,82), eye motility disorders such as strabismus (83), unstable fixation, nystagmus (84), inadequate saccades and smooth pursuit movements (85), and inadequate accommodation (86). In addition, there are difficulties in visuo-spatial analysis and disorders of other higher visual functions (87).

Injury to the brain has become the most common cause of visual impairment in children in high-income countries (88,89). However, there is as yet no consensus on a definition of the diagnosis for cerebral visual impairment (CVI) and, consequently, no ICD-10 code exists.

Children with CVI are given other diagnosis codes, e.g. strabismus or nystagmus, and as a result, the true incidence and prevalence of CVI in children is difficult to assess. Nevertheless, Mitry et al. (90) highlight a more than two-fold increase in the number of new blind and partial-sighted children registered in England between 1982 and 2011. This is a result of improved survival of critically ill newborns, particularly those born preterm.

In adults, lesions to the retino-geniculate-cortical pathway cause predictable VF defects (21). Similar lesions sustained early in life are generally better compensated, resulting in smaller or no VF defects (91). The VF-function can be correlated with the pattern of injury in cortico-subcortical injuries (i.e. injuries in the late 3rd trimester, > 34 GW), but only in cases of extensive WMDI or malformations for the earlier lesion patterns (82), and presumably the is a result of brain plasticity during the maturation period (92). Further, there is a topographical correspondence between the VF-function and the lesion pattern: hemianopias are seen in injuries in the late 3rd trimester causing focal infarct (82), whereas bilateral homonymous inferior quadrantdysopsias are common in WMDI, indicating bilateral injuries to the superior portions of the optic radiations (81).

Injuries to the posterior visual pathways are associated with thinning of the retinal nerve fibre layer and the macular ganglion cell complex, assessed with ocular coherence tomography (OCT) - seen in both congenital and later acquired lesions (93,94). The tentative mechanism would be retrograde trans-synaptic degeneration (RTSD). Individuals with WMDI demonstrate abnormal appearance of the optic discs, with reduced amount of neural tissue as either small discs or discs with large cups; a finding supporting the hypothesis that a lesion to the immature posterior visual system causes RTSD of the retinal ganglion cell layer (95). The causal link between primary injury in the immature optic radiation and thinning of the retinal ganglion cell layer has been investigated in this thesis (Study III & IV).

1.3 NEUROIMAGING OF EARLY BRAIN LESIONS

Neuroimaging is invaluable in the investigation of early brain lesions. Imaging modalities include primarily cranial ultrasound (CUS), magnetic resonance imaging (MRI) and computed tomography (CT), all of which are used for different reasons at different points. Nuclear imaging techniques, including as positron-emission tomography (PET), have no general role in neuroimaging of early brain lesions.

Bedside CUS is suitable for the majority of acute conditions in the newborn and young infant, and is used extensively in the neonatal intensive care unit (NICU). CUS has the advantage of being fast and serial examinations can be made. It is often the basis for diagnosis in the acute phase. However, the interpretation is dependent on the operator's experience, and subtle findings, typically cortical and white matter abnormalities, are difficult to detect. Hence, CUS has a low negative predictive value, i.e. does not always exclude pathology.

Today CT has little role in the investigation of early brain lesion. CT can be considered a complement when certain diagnoses need to be investigated. Calcifications are readably seen on CT and may be diagnostic for certain infections as cause for early brain lesion, often due

to intrauterine infections. Bone pathologies are, naturally, best seen on CT, and the method used may therefore be important in the radiological work-up of several syndromes.

1.3.1 Conventional magnetic resonance imaging in early brain lesions

Magnetic resonance imaging (MRI) is the method of choice for detecting and characterizing early brain lesions, stipulating timing for the insult and providing prognostic predictions. All individuals with early brain lesions should therefore have an MRI examination.

The timing of the MRI examination is dependent on the clinical question. The asphyxiated term-born should have an MRI in the neonatal period to detect acute/subacute injury. Acute neurological symptoms, e.g. neonatal seizures, should also have prompt MRI. Neonatal MRI is, on the other hand, seldom indicated in the preterm and imaging is instead often performed at term-equivalent age. However, to assess the full extent of the brain lesion, especially WMDI, imaging is preferred after 2 years of age, when the brain has matured from an imaging point of view (96).

Magnetic resonance imaging sequences in the clinical examination include T1- (T1w) and T2-weighted (T2w) sequences, fluid-attenuation inversion-recovery images (FLAIR), diffusion-weighted MRI (dMRI) and a susceptibility-sensitive sequence. Imaging should cover relevant imaging planes, and high-resolution 3D-sequences can be useful. This set of MRI sequences constitute a basic clinical protocol, but may be complemented depending on the specific clinical question, or in research.

T1w- and T2w-images are used for structural/anatomical and pathological assessments. The immature and the infant brain has a much larger water-content and is not yet myelinated, and hence the T1- and T2-relaxation times are considerably longer (97). This has to be considered in MRI during neonatal period and up until 1-2 years of age. Fluid-attenuation inversion-recovery images are sensitive for pathological changes, e.g. gliosis, and are valuable in assessing the brain parenchyma adjacent to CSF-spaces, such as the periventricular WM. Diffusion-weighted MRI can detect the evolution of ischemic and cytotoxic events. Sequences for detecting haemorrhage, most often gradient-echo (GRE) T2*-weighted sequences or susceptibility-weighted imaging (SWI) to visualize the susceptibility effects from blood-breakdown products, are useful. However, in contrast to adults, blood-breakdown products are often cleared away more effectively in young children and lost on MRI after a few years.

1.3.1.1 Magnetic resonance imaging in malformations of cortical development

Magnetic resonance imaging is invaluable in detecting and characterizing malformations of cortical development (35). Epilepsy is common in this lesion type group, and is often the reason for the MRI examination. Imaging findings in malformations of cortical development can be subtle, e.g. small areas of focal cortical dysplasia, or hard to depict, such as abnormal gyration patterns in polymicrogyria. The MRI examination should therefore be optimized to achieve the best possible morphological evaluation, preferably using high-field MR systems (3 Tesla). Dedicated sequences include sequences for increased GM/WM contrast, high-

resolution anatomical T1w and T2w/FLAIR images to evaluate the cortical layer and structure and areas of abnormal myelination. Diffusion-weighted MRI and SWI should also be included. The presence of neoplastic cells (35) needs to be assessed, often best with FLAIR sequences.

1.3.1.2 Magnetic resonance imaging in white matter damage of immaturity

Magnetic resonance imaging of WMDI includes assessing findings indicative of PVL and/or GMH/IVH and evaluation of associated lesions. As discussed earlier, the lesional spectrum in WMDI also includes "punctate" lesions in the deep WM with increased T1-signal and no restricted diffusion. As these lesions disappear on follow-up or leave traces of hypomyelination, and have no correlates in outcome, they are not considered further herein.

Cystic-PVL has a characteristic appearance with an irregular ventricular border, ventriculomegaly secondary to the periventricular parenchymal loss and abutted grey matter in deep cortical gyri (98). Non-cystic and diffuse PVL are seen on T2/FLAIR as areas of hyperintense gliotic changes, often lining the periventricular WM and extending into the deep WM, frequently appearing patchy. Residues of blood-breakdown products on T2*/SWI can be seen in the ventricular subependyma or in the ventricles and choroid plexus, indicating GMH/IVH. The WM reduction in IVH can be extensive with ventriculomegali. Focal reduction of the deep periventricular WM corresponding to the medullary veins, often with an associated porencephalic cyst, indicate an earlier PHI. In extensive WMDI there is severe reduction of deep periventricular WM, however, to confidently assess the amount of residual WM, the WM should be myelinated and the periventricular WM should be not be compressed by expanding ventricles, e.g. hydrocephalus. Anterior affection in WMDI indicate injury in the earlier part of the early 3rd trimester (24-30 GW), whereas posterior dominance is characteristic for injuries closer to (30-) 34 GW (99).

Associated lesions to WMDI include the basal ganglia, thalamus, brainstem and cerebellum (12). Injuries in these structures are seen as volume reduction and hyperintensities on T2/FLAIR. Basal ganglia and thalamic injuries can be primary or secondary (12), the latter most common, however, conventional end-stage MRI cannot differentiate between the two. Here dMRI provides clues (see 3.3.2.5). Characteristic thinning of the isthmus of the corpus callosum is common in WMDI causing CP due to secondary (Wallerian) neurodegeneration of the transcallosal fibres. Thinning of the optic nerves, optic chiasm and optic tracts, and T2/FLAIR hyperintensities in the LGN (100) are seen in WMDI causing visual impairment, and are believed to be secondary due to retrograde trans-synaptic degeneration.

1.3.1.3 Magnetic resonance imaging in cortical and subcortical grey matter injuries

Injuries in the late 3rd trimester typically affect the cortical and subcortical grey matter and are mainly of vascular origin.

Hypoxic-ischemic injuries (HI) can be acute or prolonged and profound or partial. Term neonates with hypoxic-ischemic encephalopathy should have an MRI in the neonatal period.

Acute, profound HI in the term neonate typically affects the basal ganglia, thalamus, cortical peri-rolandic/central regions and, in extreme cases, the hippocampias, as described in 1.2.1.3. Diffusion-weighted MRI is the best sequence for detecting acute ischemia but may, in the neonate, underestimate lesions in the basal ganglia and thalamus as these structures have altered signal characteristics on dMRI in early life (101). For practical reasons (e.g. hypothermia treatment in HI), the MRI examination may not be performed until 5-10 days after the ischemic event. At this time, the ADC may have pseudo-normalized and instead, conventional sequences, primarily T1w-images, are more sensitive to detecting injury (101). Differentiation between cytotoxic changes of different origins, i.e. non-ischemic, may be difficult. Usually, the injury pattern and additional clinical information may help. Hypoglycaemia is common in neonates and extensive areas of restricted diffusion may be seen. However, these areas have an occipital predilection, are often bilateral and do not follow vascular territories (102). Prolonged, partial asphyxia typically results in parasagittal lesions in the watershed zones. Injuries range from mild cortical watershed infarcts (Figure 1-7, p. 27) to severe multicystic encephalopathy. For HI, the end-stage MRI pattern reveals chronic ischemic injuries, typically with increased water signal, volume reduction and cystic transformations.

Perinatal ischemic stroke (PAS) are focal infarcts caused by an impaired or ceased blood flow in a major cerebral artery, often due to thromboembolism (71), as described in 1.2.1.3. Magnetic resonance imaging of PAS reveals ischemic lesions corresponding to a vessel territory. In general, adult-like MRI signal changes are seen. The exception can be acute/subacute infarcts to the basal ganglia and thalami in the neonate period, as discussed above. In PAS causing WMDI the distribution of the white matter injury follow a vessel territory and cortical injuries are common, not only secondary, and may be severe. PAS in the middle cerebral artery (MCA), or absent MCA, has been the suggestive cause of schizencephaly, in some cases with confirmed MCA-occlusion on MR-angiography (42).

1.3.1.4 Magnetic resonance imaging in cerebral palsy

The role of MRI in cerebral palsy (CP) is to identify the underlying lesion or abnormality and to estimate the timing of injury. The recommendations are, therefore, that every child with CP should have an MRI examination. The European recommendations (103) for MRI in CP are to wait until 2 years of age for lesion classification, unless an MRI scan at an earlier age clearly shows a pathogenic pattern.

In a fairly recent literature review, Krägeloh-Mann & Horber (104) concluded that MRI was abnormal in 86-90 % of CP cases, and that it gave clues to the aetiology in the majority of these cases. Imaging findings are also in good correlation with the clinical symptoms of CP (44). However, and this is shown repeatedly, that MRI is normal in around 10 % in individuals with CP (44,104). The distribution of the lesion types (33) is, in non-selected materials, fairly consistent: malformations represent nearly 10 %, WMDI around 40 % and cortical/subcortical grey matter lesions 20 % of cases (104). As expected, WMDI is most prevalent in prematurely born children, whereas the other lesion types are more common in children born at term. However, the degree of WMDI may be difficult to assess before the com-

pletion of myelination around 2 years of age, especially for milder cases. Likewise, lesions in the basal ganglia and thalamus may not be identifiable on early MRI as they are often secondary and/or subtle.

The relationship between the lesions seen on conventional MRI and the clinical symptoms of CP are understood to some extent. Focal infarcts commonly cause unilateral CP, and bilateral periventricular WMDI cause spastic leg-dominated CP due to the closeness of the lower limb motor fibres to the ventricles. The extent of the white matter reduction in WMDI is associated with the degree of motor impairment (105,106). Lesions in the basal ganglia and thalami are associated with more severe motor impairments and a dystonic rather than spastic CP pattern. In unilateral CP, the extent of the lesion (106) and degree of dysgenesis in the cortico-spinal tract (108) are related to the severity of hand motor impairment.

In a recent systematic review of the available studies on the relationship between findings on structural MRI and motor outcome in children with CP (37 studies met inclusion criteria, total 2330 subjects), Arnfield et al (109) concluded that there is evidence for a relationship between lesion type and the motor type (i.e. the CP subtype and neurology), and the gross motor function classified with Gross Motor Function Classification System (GMFCS) (110). However, they point out the need for better quantitative measures of the MRI findings, specifically regarding the location and severity of the lesion. Recent efforts include standardized semi-quantitative scoring systems (e.g. 111,112), however, these are still only used for research purposes, and have not yet come into clinical practice.

1.3.1.5 Magnetic resonance imaging in early brain lesions causing cerebral visual impairment

Early brain injuries to the visual pathways can cause cerebral visual impairment (CVI) (113), and, similarly to CP, children with CVI suspected of early brain lesion should have an MRI examination. However, contrary to CP, the correlation between findings on MRI and visual dysfunction has not been extensively investigated.

Injuries to the posterior visual pathways can be evaluated with MRI, and include lesions in the optic radiation (OR), the occipital cortex and the basal ganglia and thalamus, including lateral geniculate nucleus (LGN). Injuries to the OR are most commonly caused by WMDI (98,114), in focal infarcts (FI) (115) or in watershed infarcts. Findings on end-stage MRI include periventricular WM reduction and gliosis along the anticipated course of the OR, especially in WMDI. Malformations of cortical development could also involve the OR (82). Primary cortical injuries are seen in FI as cortical thinning (115). Occipital polymicrogyria does not necessarily cause visual impairment, however, and normal visual fields and cortical activation on visual functional MRI can be seen (116). This highlights the difficulty in predicting visual function from MRI in malformations, and the visual system seems to have a high-degree of self-organizing plasticity in malformations of cortical development as discussed earlier in 1.4.2. Lastly, the full extent of OR involvement in early brain lesions, specifically in WMDI, may be difficult to judge on conventional structural MRI.

Associated lesions to the primary injuries in the posterior visual pathways include injuries in the basal ganglia and thalamus, most notably the LGN, showing volume reduction and/or increased water signal on MRI (114). The changes to the basal ganglia and thalamus can be primary or secondary, depending on the aetiology and extent of the early brain lesion. However, involvement of these structures correlate strongly with visual impairment (117). Thinning of the optic nerves, the optic chiasm and optic tracts can be assessed with MRI and, together with LGN injuries (100), indicate secondary neurodegenerative injuries.

1.3.2 Diffusion-weighted magnetic resonance imaging in early brain lesions

Diffusion-weighted MRI (dMRI) is a sensitive method for studying alterations to tissue microstructure and fibre tract organization after early brain injury. Some specific results related to early brain lesions causing cerebral palsy and/or visual impairments will be outlined in the following paragraphs. Diffusion-weighted MRI is described in more detail in 3.3.2.

1.3.2.1 Diffusion-weighted magnetic resonance imaging in early brain lesions causing cerebral palsy

Diffusion-weighted MRI has gained increasing interest in the last decade for studying macro- and microstructural changes in several major white matter tracts and their functional-structural relationships in CP (for a review see Scheck et al. 2012 (118)). A wealth of studies show alterations to different diffusion parameters in the descending motor pathways indicating altered microstructure (118). These studies have mainly used DTI to show decreased fractional anisotropy (FA) and increased mean diffusivity (MD) (118). In parts of the corticospinal tract (CST) distant from the primary lesion the DTI parametric changes are indicative of secondary anterograde (Wallerian) neurodegeneration (119,120). The superior and posterior thalamic radiations have gained interest recently as they seem more sensitive to DTI parametric changes upon injury (118). Transcallosal fibres show more conflicting results (121–123). Association fibres are increasingly studied and show promising results (122,124). There is evidence that parametric changes (primarily FA) in various tracts correlate with the overall severity of CP and specific measures of motor function (118) and sensory function (125).

Most dMRI studies on CP have used DTI, but recently an increasing number of studies use more advanced methodology, including whole-brain connectivity approaches to show alterations to the connectivity profiles in various tracts in CP (122,126) and/or high-order diffusion models and probabilistic fibre tractography (122,124,125,127), which allow a more accurate study of white matter tracts (128).

Many recent studies show, interestingly, positive post-treatment effects of botulinium toxin A injections and/or rehabilitation (physio- and occupational therapy), both in the CST (129,130) and whole-brain connectivity (131) that correlate with dMRI changes (increased FA in tracts). This indicates the potential of dMRI to capture plasticity processes.

1.3.2.2 Diffusion-weighted magnetic resonance imaging in early brain lesions causing cerebral visual impairment

Despite the associations between early brain lesions and visual impairments, few studies have investigated the effect of injury to the immature visual system with dMRI. Some case reports exist. Seghier et al (132) used dMRI in combination with fMRI to study the recovery of visual function in an infant with perinatal stroke. In this case, the optic radiation (OR), delineated from fibre tracking, showed a perilesional volumetric increase on sequential imaging at 12 and 20 months of age, which was interpreted as structural modifications in parallel with functional recovery. Two case reports show perilesional changes to the course of the OR in WMDI (92,133). Our recent study, presented in this thesis (Study III & IV), shows advanced structural changes to the immature OR after WMDI, with evidence of topographical retrograde trans-synaptic degeneration in the retina and corresponding VF defects. More studies exist on the OR in preterm born children. These show changes in diffusion parameters indicating altered white matter microstructure (134–138). In one study these alterations correlated with the degree (no, mild/moderate or severe) of WMDI (138). Further, these changes correlated with early assessment of visual ability (134,135) and visual evoked potentials (136) at term age, but not at later follow-ups at 2 and 4 years (138). From the available studies one can conclude a general vulnerability of the OR in the third trimester, but a limited effect on long-term functional outcome.

1.4 BRAIN RE-ORGANISATION IN EARLY BRAIN LESIONS

Injury during early brain development occurs when the brain's potential for plasticity is at its greatest (43). The relationship between compensatory mechanisms and the timing of brain injury was studied by the American neurologist Margaret Kennard (1899-1975) in early pioneering work in the 1930-40's together with John Fulton (139). They could see a negative relationship between the functional outcome and the timing of the injury, attributed to the greater potential of plasticity in the younger brain.

This thesis aims to investigate the brain organisation, or re-organisation, after injury during early brain development. An outline of the main pattern of re-organisation in the motor and the visual system will hereby follow.

1.4.1 Motor and sensory system

Several studies show re-organization of the motor and somatosensory systems after early brain injuries (140). With transcranial magnetic stimulation (TMS), the cortical projection patterns can be studied. Alterations to the normal crossed projection pattern, in which the hemiplegic hand is controlled by from the contralateral side, are seen in unilateral CP and include both ipsilateral and mixed projection patterns (141–143). These ipsi- and mixed projection patterns are seen for all types of early brain lesions (142,143), and indicate interhemispheric re-organization, possibly from persisting connections from the bilateral projections during early developmental stages (24). In contrast, the sensory system shows mainly an ipsilesional re-organisation after injury (142,144). The reason has been attributed to still de-

veloping thalamo-cortical connections (140), especially for early injuries in the second and early third trimester, as long as the post-central gyrus is not injured (140). Several tractography studies have now showed alterations to motor and/or sensory tracts (125,127,145–147). The potential for re-organization is evident considering that the sensory function can be well preserved even in cases of large periventricular lesions (140,144). However, inter-hemispheric re-organization of the motor system is associated with poorer function (142,145), but whether this is due to a hemispheric sensory-motor disassociation, an inherent poorer function of ipsilesional motor projections or simply a manifestation of a larger injury is unclear.

In summary, TMS studies and dMRI fibre tractography studies, mainly case studies, indicate that the re-organizational pattern for the motor and somatosensory system are different in early brain lesions, and that the compensatory mechanisms in the somatosensory system are greater than in the motor system. Presumably this is due to differences in the potential of plasticity at the time of the insult.

1.4.2 Visual system

The potential of brain plasticity in the visual system in early brain lesions is not well documented. Part of the problem is that visual assessment is difficult in the young infant, however, early identification of visual impairment is important considering its role in cognitive development (148). The visual field (VF) can be rudimentarily assessed with confrontation techniques to diagnose large VF defects (149), but detailed visual perimetry (Goldmann perimetry) to detect relative VF defects cannot be done until early school age (82). Studies show that visual function is less affected in individuals with early brain injuries compared to individuals with injuries acquired later in life (113), and this is contributed to greater compensatory mechanisms and the superior potential of plasticity early in life.

Very few studies, and these mainly case studies, have studied the plasticity of the visual function in malformations of cortical development. However, this lesion type is associated with least visual impairments, presumably due to the great potential of plasticity at this early stage of brain development (92). Dumoulin et al (116) showed in three patients with polymicrogyria and normal visual field function that cortical activation maps (V1-V3), delineated with retinotopic fMRI mapping, had normal anatomical location in the occipital lobes and normal activation pattern despite substantial overlaps with areas of polymicrogyria. This suggests that polymicrogyric cortex can contribute to normal visual function, a result also indicated in other studies (150). Muckli et al (151) studied a 10-year old girl with only one hemisphere (including agenesis of the ipsilateral diencephalon) and a mild hemiplegia, but near normal visual field function. Retinotopic fMRI mapping revealed representation of both visual hemifields (V1-V3) in the remaining hemisphere and in the LGN, concluding that in cases of very early malformations (here around 5 GW) the developing brain has an extraordinary potential of self-organisation in the developing mechanisms for cortical map formation.

Injuries during the early 3rd trimester causing WMDI are often associated with visual impairment, most notably VF defects, which correlate with the severity and the extent of the WMDI (81) and involvement of the optic radiation (OR). Interestingly, and importantly, the VF defects in IVH are less pronounced, and may only be permanent in the more severe cases (IVH grad III-IV). They are, instead, more dependent on the involvement of the basal ganglia and thalamus (152,153), which are central structures important for the normal visual function. Case reports also show, as in the somatosensory system (145), tractography reconstructions of the OR that bypass the periventricular lesion (133,152).

In lesions occurring in the late 3rd trimester primarily affecting the cortical and subcortical grey matter, the visual function is also better preserved than expected, especially at long-term follow up (113), indicating plastic potential for this lesion pattern. This is the case in perinatal strokes where occipital strokes lead to less visual impairment than expected at follow-up (115,154), however, homonymous VF defects are common. This is illustrated in a case-study of perinatal stroke by Seghier et al (132). They could show an ipsilesional recovery of cortical response on visual fMRI and an increasing structural prominence of the optic radiation (delineated with deterministic tensor tractography) on imaging at 20 months, compared to imaging at 12 months. However, nothing is mentioned in the study regarding clinical evaluation of the visual function. Injuries involving the central structures such as the basal ganglia and the thalamus in hypoxic-ischemic injury or in focal infarcts are often associated with visual dysfunction, regardless of the extent of involvement of the OR or the occipital cortex (82,117,155). This emphasises the important role the basal ganglia and the thalami have for the development of the visual function.

In summary, there is evidence for a better visual recovery after early brain lesions than after lesions acquired in adult life. This is attributed to the potential of plasticity at the time of the insult. However, the exact mechanisms are not clear and seem to depend on both the timing and extent of the lesion, but studies suggest intra-hemispheric re-organization.

2 AIMS OF THESIS

The overall aim of this thesis was to study the organization of the motor and visual system in early brain lesions by using dMRI and advanced white matter fibre tractography. The specific aims of the studies on the motor (Study I & II) and visual system (Study III & IV) are outlined below.

Study I

The specific aim of this study was to investigate the microstructure in central parts of cortico-fugal fibres; at the level of the posterior limb of the internal capsule, the cerebral peduncle and the portion of fibres connecting these areas in unilateral CP, and their correlations with hand motor function.

Study II

The aim of this study was to further investigate the changes to the cortico-fugal fibres seen in Study I by using a combined normalization and probabilistic fibre-tracking methods for improved fibre tractography. With this method, the cortico-spinal tract, from primary motor cortex to cerebral peduncle, could be investigated both close to and distant from the lesion, and compared to the adjacent thalamic projections to the primary sensory cortex.

Study III

The specific aim of this study was to seek evidence of a relationship between damage to the immature optic radiation and subsequent development of the retinal nerve fibre layer, and associated visual field function in individuals with known WMDI and visual dysfunction.

Study IV

The specific aim of this study was to refine the fibre tractography of optic radiation in Study III by including cortical targets from retinotopic fMRI mapping. The retinotopic organisation of the optic radiation could then be studied and compared with structural measurements in the retina of the macular ganglion cell complex, which has a more direct correspondence to the visual field. The study could provide evidence for retrograde trans-synaptic degeneration in the visual system.

3 METHODS

3.1 STUDY DESIGN

The motor system (Study I & II) was investigated in a cross-sectional study design using a convenience sample from a larger cohort of children with unilateral CP. A control group of age- and sex-matched children were recruited.

The visual system (Study III & IV) was investigated in an extended case description design. An expert group (consisting of paediatric neuro-ophthalmologist, paediatric neuroradiologist, optometrician, MR-physicist/neuroradiologist) estimated that very few patients with early brain lesions who have suitable visual field deficits and can cope with the MRI session and the assessment of visual field function with standardized methods. After reviewing possible participants in the Stockholm area, the overall majority of cases were found to have WMDI. For this reason we decided to limit the study group to a cohort with WMDI. A group of age- and sex-matched controls was recruited. A second control/patient group of (young) adults with visual field deficits secondary to lesions in the visual pathways acquired later in childhood was also recruited.

3.2 PARTICIPANTS

3.2.1 Motor system (Study I & II)

Study I & II shared the same study cohort. The index group included 15 children/adolescents (6 boys, 9 girls, median age 12.4 years, min 7.2, max 17) with unilateral CP, recruited as a convenience sample with a wide range in hand function. Inclusion criteria was a diagnosis of unilateral CP according to the Surveillance of Cerebral Palsy in Europe criteria 2000 (103). Exclusion criteria were epilepsy, hearing impairment and ventriculo-peritoneal shunt. From the sample, two children (one with malformation of cortical development and one with WMDI) were excluded due to poor quality of the dMRI data.

A convenience sample of 24 sex- and age-matched typically developing children/adolescents (9 boys, 15 girls; median age 12.7 years, min 8.8, max 17.3) were recruited as a control group for the dMRI measures.

Data was collected during 2007 at the MR Research Centre at Karolinska University Hospital. This was part of a study that also included transcranial magnetic stimulation (TMS). On arrival, the children were first seen by an experienced paediatric neurologist to confirm the CP diagnosis. This was followed by assessment of motor and hand function by a physiotherapist. Thereafter, TMS and neuroimaging were performed - the order of the examinations was individualized to meet the needs of the child, and in some cases divided into two separate sessions. The total time spent at the hospital for each patient was around 4 hours.

The children in the control group were imaged using the same neuroimaging protocol as the CP group. For them, the total time spent at the hospital was around 1.5 hours.

3.2.2 Visual system (Study III & IV)

The Study III cohort consisted of seven young adults (2 males, 5 females; age range 18 – 35 years) with known WMDI and visual dysfunction. The participants were selected from a large cohort of individuals with WMDI who presented with visual dysfunction as children, collected over 25 years by Lena Jacobson (thesis co-supervisor) in clinical paediatric ophthalmology care. Around 30 had reached adulthood, and those with the best intellectual, attention, and motor prerequisites, who could cooperate in the demanding MRI sessions (without spastic movements to sound), with ability to maintain fixation during ocular coherence tomography (OCT), and who could follow instructions and carry out a standardized perimetry test, were selected. Eight individuals were invited to the study, of which one declined participation.

Study IV shared the same index group as Study III, and included a control group of six healthy young adults (2 males, 4 females; age range 22 – 33 years).

Data was collected in autumn 2012 and spring 2013 on two separate occasions. First, visual function was assessed and fundus morphology was documented with photography OCT at St Erik's Eye Hospital, Stockholm. Then neuroimaging was performed at the MR Research Centre at Karolinska University Hospital. The visual examinations lasted around 1.5 hours and neuroimaging around 2 hours. On both occasions the schedule was adapted to the individual's needs to include breaks when necessary.

3.3 NEUROIMAGING

Magnetic resonance imaging (MRI) is the modality of choice for detecting and describing early brain lesions (see also 1.3). This thesis has used diffusion-weighted MRI (dMRI) as the main imaging method, which is described in detail in this section. This is followed by a short primer on retinotopic fMRI mapping, which is used to create cortical activation ROIs in Study IV. However, some basic understanding of MRI is given first, as this is needed to understand the imaging techniques dMRI and fMRI.

3.3.1 Basis of magnetic resonance imaging

Magnetic resonance imaging (MRI) relies on the phenomenon of nuclear magnetic resonance (NMR) to create images of nuclear spin systems in the body. In clinical MRI, protons (^{1}H) are ideal due to their abundance in the body as the nuclei of the hydrogen atoms in water molecules (H_2O), making MRI an extremely versatile tool for imaging of the human body.

The basis for NMR is that certain atomic nuclei and elementary particles (the condition is a non-zero net spin number) can absorb and re-emit electromagnetic radiation when placed in an external magnetic field $\mathbf{B}_0$. The frequency of the electromagnetic radiation is given by the Larmor equation:

$$f_{\text{Larmor}} = \frac{\gamma}{2\pi} B_0$$

Where *f* is the frequency in Hz [s^{-1}] of the absorbed/emitted radiofrequency waves, and γ is the gyromagnetic ratio [rad · s^{-1} · T^{-1}], a nuclei specific proportionality constant, and B_0 [T] is the net strength of $\mathbf{B}_0$. In the case of protons γ = 267.513×10^6 rad · s^{-1} · T^{-1}, giving a Larmor frequency of 42.576 MHz · T^{-1}.

In an external magnetic field, the ground-state energy of a proton is split into two states, designated spin-numbers = ± ½ , separated by an energy difference $\Delta E = h\gamma B_0$. The distribution between the two states will thus be skewed, following a Boltzmann distribution:

$$\frac{N_{S=½}}{N_{S=-½}} = e^{\frac{\Delta E}{kT}} = e^{\frac{h\gamma B_0}{kT}}$$

Here *N* denotes the number of protons with spin-numbers ½ or -½, h is Plank's constant, k is Boltzmann's constant, T is the absolute temperature [K], B_0 is the net external magnetic field, and γ is the gyromagnetic ratio. At 1 Tesla and at body temperature the difference in population of the spin states is only around 1 ppm!

On a macroscopic scale, the uneven distribution between the spin-states creates a net magnetization **M**, parallel with static external field $\mathbf{B}_0$, by convention defined as the z-axis in the MR-scanner.

3.3.1.1 RF-excitation

At the start of the MR-experiment, a radiofrequency (RF) pulse (of the order of 1 ms long) is applied at the Larmor frequency, depositing energy into the spin-system. This allows transitions from the low-energy state into the high-energy state. The net effect is a decrease in the z-component of **M**, M_z. After the RF-excitation, the system returns to the equilibrium state, as energy is gradually lost from the spin-system by interactions with its surroundings. This process is coined the T1-relaxation (or spin-lattice relaxation), and exhibits an exponential recovery (T1-value defined as time 63 % of recovery of equilibrium magnitude of M_z). The T1-values in brain tissue are around 900 ms in WM, 1300 ms in GM and 3 s in CSF (3 T). Since T1-values are tissue-specific, the relative differences in T1-relaxation times between tissues can be exploited to create T1-weighted (T1w) MR images. In this thesis, T1w-images are used for evaluation of the anatomy of the cortex, the central GM and the CSF-spaces (especially the ventricles) in patients with early brain lesions. T1w-images are also used in the post-processing steps in fMRI to visualize activation maps on flattened T1w-cortical maps, and in dMRI, fibre tracts are overlaid on T1w-images for evaluation of the anatomical course of the tracts.

In addition, the random phase distribution in the angular magnetic moments **μ** associated with the spin state of each proton gives rise to a second macroscopic magnetisation effect. The RF-excitation pulse is applied perpendicular to the $\mathbf{B}_0$-field, and creates a temporary quantum phase-coherence. This generates a faint magnetic field, or transverse magnetization $\mathbf{M}_{xy}$ in the transverse plane perpendicular to the z-axis. This signal can be picked up by the MR scanner receiver coils to generate the MR image. After the RF-excitation the phase-coherence

is gradually lost (by spin-spin interactions) and the system returns to equilibrium ($\mathbf{M}_{xy}= \mathbf{0}$). This relaxation process is coined T2-relaxation (or spin-spin relaxation), and follows an exponential decay (T2-value is defined as 63 % reduction of M_{xy}). The T2-values in brain tissue are around 80 ms, 110 ms and 1200 ms for GM, WM and CSF respectively (3 T). Many pathological processes change the T2-relaxation properties of the tissue, which then stands out on the T2w-images. In this thesis, T2w-images are used in the radiological assessment of early brain lesions to both detect and define the extent of the lesions and residual gliosis.

The phase-dispersion process is not only dependent on spin-spin interactions, rather any field perturbation will influence it. These range from small field perturbations (differences in magnetic susceptibility of tissue components, e.g. blood-oxygenation level, or blood breakdown after haemorrhage), to local/regional perturbations (e.g. in the vicinity to metal implants or air cavities) to large scale perturbation (e.g. inhomogeneities in the $\mathbf{B}_0$-field or RF-field). These effects speed up the phase dispersion, and result in a faster so called T2*-relaxation. Large field inhomogeneities create rapid phase dispersion, often resulting in rapid, total signal degradation. The T2*-relaxation is exploited to achieve T2*w-images and in susceptibility-weighted MRI (SWI), but can also hamper the k-space spatial-encoding (see 3.3.1.2) and result in image artifacts. These may be significant in echo-planar imaging (EPI) (156), the imaging method used in dMRI and fMRI in this thesis. Ways to reduce induced image distortions in the dMRI and the fMRI sequences had to be considered in this work. This is outlined more specifically in dedicated paragraphs.

3.3.1.2 K-space formalism and image contrast

The creation of the MR image of an object is achieved by applying spatially varying gradient fields **G**, both during and after the RF-excitation. A linear gradient field **G** applied over the imaged object will induce spatially dependent resonance frequencies as

$$f(\mathbf{r}) = \frac{\gamma}{2\pi}(B_0 + \mathbf{G}\cdot\mathbf{r})$$

Here ***r*** is the position in space [m], **G** is the gradient [T/m]. This will give a spectrum of frequencies in the MR signal. In fact, the MR signal *S* in the receiver coils detected at time *t* can be expressed as the Fourier transform of the spin density distribution ρ in the imaged object as

$$S(t) = \int_{\mathbb{R}} \rho(\mathbf{r}) e^{i\mathbf{k}(t)\cdot\mathbf{r}} d\mathbf{r}$$

where

$$\mathbf{k}(t) = \gamma \int_o^t \mathbf{G}(\tau) d\tau$$

The value of the spatial frequency **k** is the accumulated gradient history multiplied by the gyromagnetic ratio γ. In fact, the use of spatial gradients naturally parameterises the MR signal

according to its spatial frequency **k**, and the spatial domain **r** (i.e. the image [m]) and k-space domain **k** (i.e. spatial frequency [1/m]) constitute a Fourier pair. The detected MR signal in the receiver coils is thus the Fourier transform of the NMR signal from the object. Hence, the MR image can then be obtained by an inverse Fourier-transform of MR signal. This is the basis for the k-space formalism in MRI. An example of the MR image and its k-space MR signal is shown in Figure 3-1.

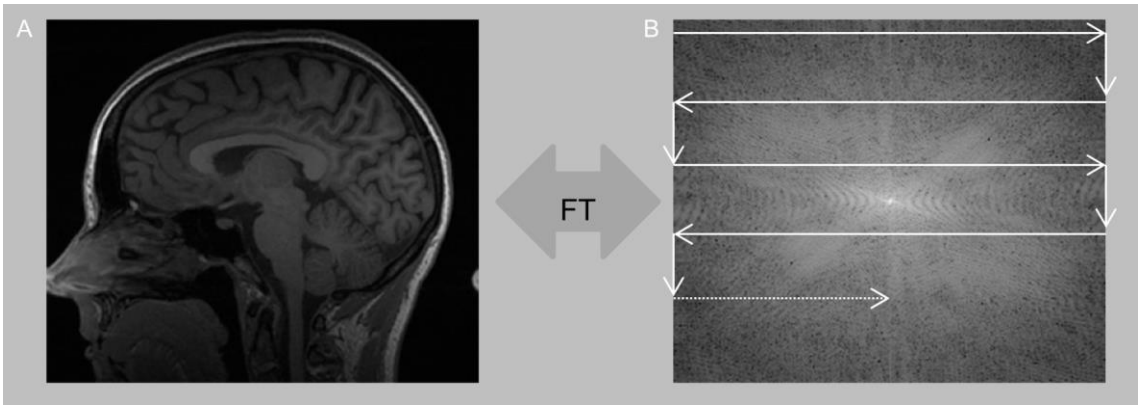

Figure 3-1: (A) Sagital T1w-image of the brain and its (B) representation in k-space. A trajectory for an EPI-readout is outlined in k-space (white arrows). FT=Fourier transform.

The formation of an MR image can be viewed as sampling the MR signal in k-space. However, this takes time since the traverse of k-space is limited by the strength and switching rates of the gradients (typical gradient strengths are in the order of 40-60 $mT \cdot m^{-1}$ and slew-rates in the order of 200 $mT \cdot m^{-1} \cdot s^{-1}$). Time is a limitation because of the on-going relaxation processes (primarily the quick T2/T2*-relaxation), which will cause the MR signal to vary between sample points in k-space, and eventually to disappear altogether. Therefore, it is often not possible to sample the entire k-space at one time. Instead, repeated RF-excitations are used to sample k-space in parts, most often one or several "k-space line/s" at a time. With such a sampling strategy, an image will take minutes to acquire. The exception is when fast image acquisition is required, such as in fMRI, dMRI or perfusion-weighted MRI. Most of these techniques use k-space sampling with EPI (156), in which the whole k-space in a single image slice is sampled at one time (i.e. one single RF-excitation). A slice in an image is acquired in tens of ms. An illustration of an EPI k-space sampling trajectory is given in Figure 3-1B.

Importantly, the k-space sampling strategy will determine the fundamental image contrast, i.e. dominated by a T1- or a T2/T2*-contrast. Sampling one "k-space line" takes in the order of tenths of a ms, which is quick in relation to the T1- and T2/T2*-relaxation. The central parts of k-space (i.e. small nominal values in **k**) are the contrast-bearing spatial frequencies in the MR signal. Hence the fundamental image contrast is determined when those parts of k-space are sampled. The time between RF-excitation (i.e. between repeated energy deposition) and sampling of the centre of k-space is coined the echo time (TE). The TE primarily manipulates the T2/T2*-contrast component in the image, in the sense that the T2/T2*-contrast component increases with TE (as T2/T2*-relaxation has an exponential decay). The time be-

tween consecutive RF-excitations is coined the repetition time (TR). The TR primarily manipulates the T1-contrast component in the image, in that the T1-contrast component decreases with TR (as T1-relaxation has an exponential recovery). Hence, T1w-images are achieved by k-space sampling strategies combining short TR with short TE and, conversely, T2/T2*w-images by combining a long TR with a long TE. Images can be acquired so that neither of these processes dominate, and the weighting is, instead, dependent on the underlying proton "densities" (PD). Such images are referred to as PD-images. However, the PD shows little variation in the brain tissue and therefore PD-images are seldom used.

To further emphasize the contrast between tissues, or selectively null the signal from certain tissue components, pre-pulses, or inversion-recovery (IR) pulses, can be applied prior to the RF-excitation. This manipulates the available M_z magnetization when the RF-pulse is applied. In this thesis, IR-sequences are used in the fluid-attenuated inversion recovery (FLAIR) sequence, which is a T2w-sequence that is IR-prepared to null the CSF signal, and is useful for studying T2 changes in proximities of CSF spaces. Pre-pulses can also be used to suppress the MR signal from fat. This can reduce the fat-induced chemical shift artifacts, which is problematic in sequences using EPI-readouts like dMRI and fMRI in this work.

As described above, the RF excitation generates a faint transversal magnetization $\mathbf{M}_{xy}$ that experiences a T2* relaxation process, or free-induction decay process (FID). MR pulse sequences that sample the FID are referred to as gradient-echo (GRE) sequences. Alternatives are spin-echo (SE) sequences. In SE, a second RF pulse (also called 180° pulse) is applied in the transverse plane at a specific time (t = TE/2) after the RF excitation. The result is reversal of the effect of all the static intravoxel field inhomogeneities so that phase coherence is progressively regained. The maximum phase coherence, and resulting peak in the $\mathbf{M}_{xy}$, is achieved at t = TE. The sampling/readout of k-space is then timed so that the traversal of the centre of k-space is achieved at this point (t = TE). This "spin" echo is enveloped by the T2* relaxation, which the 180° pulse cannot reverse. In this work, GRE sequences are used for the high-resolution T1w-images and the fMRI images, the latter to exploit the BOLD-effect described in more detail in paragraph 3.3.3. SE sequences are used for the T2/FLAIR images and the dMRI.

3.3.2 Introduction to diffusion-weighted magnetic resonance imaging

In diffusion-weighted MRI (dMRI or DWI), the MR signal, or dMRI signal herein, is sensitized to the diffusion properties of tissue water to reflect various characteristics of the underlying brain tissue, including tissue structure and type, physical and physiological state, as well as the small scale microstructure (157). Diffusion-weighted MRI is a fairly new technique, but has already gained many important clinical applications. Diffusion-weighted MRI is invaluable in stroke imaging as it can detect ischemia within minutes after onset, and is an important sequence for almost any other intracranial condition. Diffusion-weighted MRI can also, as in this thesis, be used to study the white matter and its organization *in vivo* in the normal brain, in brain development or in disease.

Diffusion is a physical process describing the random-walk, or Brownian motion, of an ensemble of particles, driven by their thermal energy. For an ensemble of particles, the root-mean-square displacement r_{rms} is given by the Einstein equation $\langle r^2 \rangle = 6Dt$, where D is the diffusion coefficient, and t diffusion time during which the particles have been left to diffuse. The diffusion process follows Fick's laws (first and second), stating that the flux $\mathbf{J}$ of diffusing particles strives to even out concentration differences over time as

$$\mathbf{J} = -D\nabla C$$
$$-\nabla \mathbf{J} = \frac{\partial \mathrm{C}}{\partial \mathrm{t}} = D\nabla^2 C$$

Where C is the local concentration of particles, D is the diffusion coefficient and ∇^2 the Laplacian operator. D is dependent on temperature, viscosity (inter-molecule interactions) and molecular weight.

The diffusion of water molecules in brain tissue is complicated by various obstacles related to the intra- (e.g. organelles, cytoskeleton) and extra-cellular microstructure (e.g. myelin), the cell membrane/s, different compartments (e.g. intra-cellar cytoplasm versus extra-cellular matrix, cell membranes, different cell types) and the exchange between compartments over cell membranes (including both passive and active transport processes). Commonly, obstacles creating relative boundaries are referred to as causing "hindered" diffusion, whereas absolute boundaries (cell membranes, omitting transmembraneal diffusion/transport) are referred to as causing "restricted" diffusion. This is illustrated in Figure 3-2. However, this nomenclature is not entirely standard, e.g. hindered diffusion is often referred to as restricted diffusion. The axon diameter in brain WM is of the order of 0.5-5 μm (157). As normal diffusion times in dMRI are in the order of ~ 50 ms, the water displacement from diffusion is around 5-15 μm and, hence, the water molecules will have ample time to interact with their immediate environment. To account for the overall effect of "hindered" and "restricted" diffusion in brain tissue, and deviation from the random-walk Gaussian diffusion process, D is replaced with an apparent diffusion coefficient (ADC). The average ADC, or mean diffusivity (MD), in WM and GM are surprisingly similar in the range 7-11 x 10^{-4} mm^2/s, in the higher range in GM and lower range in WM, but significantly lower than in CSF with 27-30 x 10^{-4} mm^2/s (158).

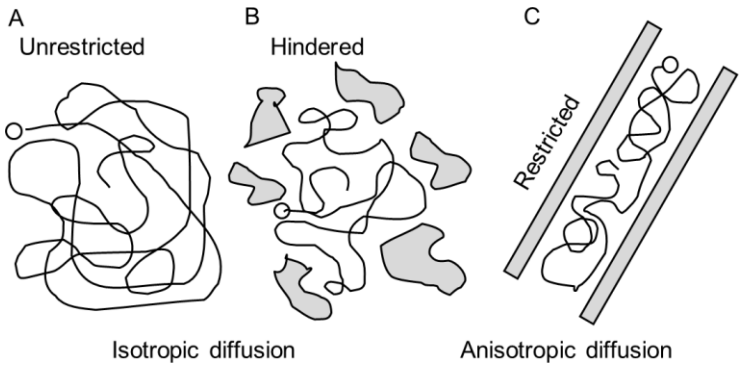

Figure 3-2: Diffusion trajectories in tissue in cases of (A) unrestricted diffusion, (B) isotropic hindered diffusion and (C) anisotropic restricted diffusion.

The diffusion process can be isotropic (same diffusion properties in all spatial directions) or anisotropic (diffusion properties are direction-dependent), see Figure 3-2.

The key observation in dMRI in the brain is that, in ordered WM (i.e. fibre bundles with coherent, parallel axons) the dMRI signal

is highly anisotropic depending on the orientation of the underlying axons (157). This is reflected in the ADC measured parallel to an axon bundle ($ADC_{//}$), which will be larger than when measured perpendicular ($ADC_{\perp}$) to the bundle, as water molecules are free to diffuse along the axons but are restricted by the cell membranes when moving in a perpendicular direction. Hence, the anisotropy in the dMRI signal will reflect the underlying neuronal structure (Figure 3-2, p. 45). The main contributor to the anisotropic diffusion in WM is the restriction to diffusion imposed by the cellular membranes, whereas the degree of myelination only modulates the diffusion anisotropy (157). This also is evident from studies in early human brain development, where an increasing degree of anisotropy is measured in the maturing major white matter tracts before the onset of myelination (159–161). In fact, the splenium of the corpus callosum is the fibre bundle with the highest degree of anisotropy in the newborn, despite being largely unmyelinated at birth (162).

The spatial resolution is in the order of 1-2 mm in dMRI. Therefore, in addition to the microscopic cellular level, the macroscopic architectural tissue characteristics (including axonal coherence and microscopic crossing fibres) and partial volume effects (including complex fibre configurations in voxels with multiple fibre population or voxel-sharing with different tissue types) will also be reflected in the dMRI signal (163). In fact, the vast majority of brain voxels contain multiple fibre populations, often crossing fibres (164), which imposes a great challenge for dMRI and will be discussed in 3.3.2.3.

3.3.2.1 Pulse-sequence considerations in diffusion-weighted MRI

In dMRI, two large gradient pulses can be applied symmetrically around the refocusing 180° pulse in a spin-echo sequence. This makes the dMRI signal sensitive to the diffusion process of tissue water, which is the so-called pulse-gradient spin echo sequence (PGSE) (165). The effect on a diffusing water molecule is a small net phase contribution to the dMRI signal, resulting in additional phase dispersion for the ensemble of diffusion spins. The effect is a diffusion-dependent attenuation of the dMRI signal as

$$S_b = S_0 e^{-b \cdot ADC_{\mathbf{r}}}$$

Here S_b is the dMRI signal, S_0 is the baseline MR signal (without diffusion encoding), $ADC_{\mathbf{r}}$ the apparent diffusion coefficient [mm^2/s] along spatial direction **r**, and b is the so called b-value [s/mm^2]. Stationary molecules will experience a zero net phase shift and their dMRI signal is thus not affected by the gradient lobes in the PGSE. By repeating the experiment without diffusion encoding (to measure S_0) the $ADC_{\mathbf{r}}$ along direction **r** is calculated as

$$ADC_{\mathbf{r}} = -\frac{1}{b} ln\left(\frac{S_b}{S_0}\right)$$

The b-value is the diffusion-sensitizing factor, and determines the length scale at which the measured diffusion coefficient $ADC_{\mathbf{r}}$ is explored. To assess the 3-dimensional diffusion properties, ADC has to be measured in all spatial directions (x,y,z). The average ADC (clinically referred to as the ADC) then estimates the mean diffusivity (MD) as $MD =$

$ADC_{average} = \frac{1}{3}(ADC_x + ADC_y + ADC_z)$. The b-value depends on the diffusion preparation in the pulse sequence. In PGSE it is given by the gradient amplitude *G*, the gradient duration δ and the separation of the gradient lobes Δ (i.e. the diffusion time), and the gyromagnetic ratio γ as $b = (\gamma G\delta)^2(\Delta - \delta/3)$. To probe the brain WM, b-values in the order of 700-3000 s/mm² are commonly used, which allows investigation of both free, hindered and restricted diffusion (157,166). The signal attenuation from the diffusion preparation is substantial: for a b-value of 1000 s/mm^2 in brain tissue (average ADC ~ 9 mm^2/s), the signal attenuation is around 60 %. As the dMRI is inherently a low signal technique, S_b will often be close to the noise floor. An illustration of the dMRI experiment is given in Figure 3-3.

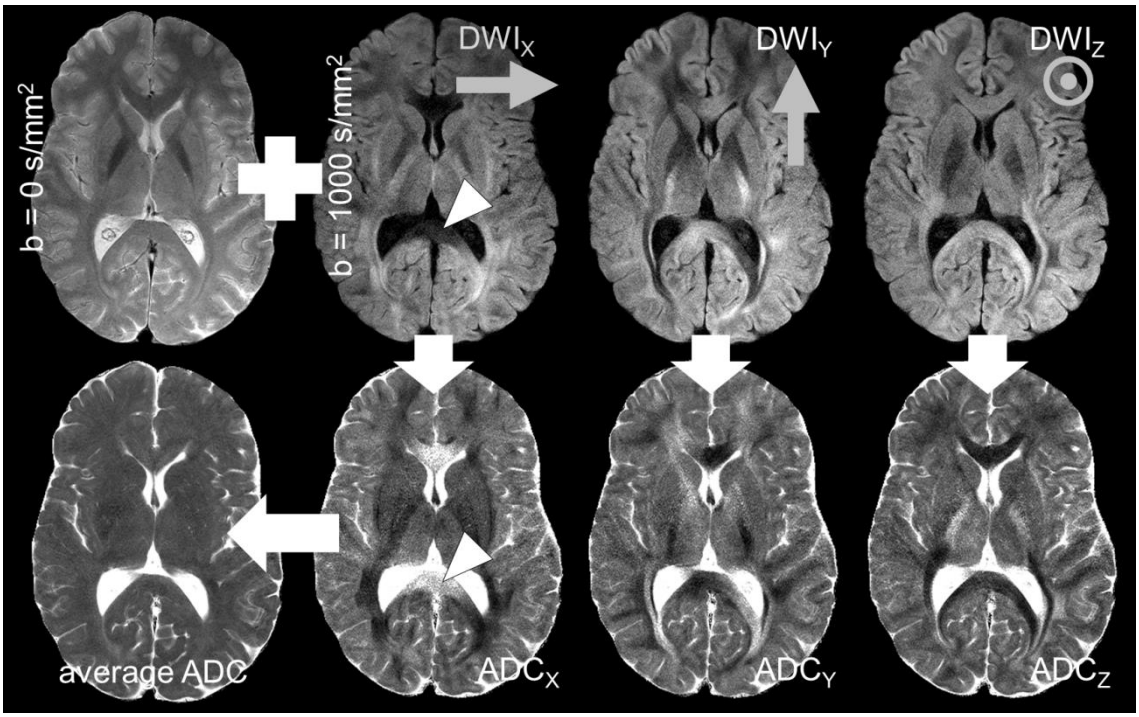

Figure 3-3: A dMRI experiment. Upper row: 1 b=0 and 3 diffusion-weighted images encoded along (x,y,z) with b=1000 s/mm^2. Lower row: corresponding ADC maps along each direction (x,y,z) and the average ADC map. Notice the rich directional information in the dMRI and ADC images (e.g. the splenium of corpus callosum marked with white arrowhead) which is not present in the average ADC. Courtesy of Stefan Skare.

In dMRI, the aim is to detect the microscopic diffusion motion of water molecules. However, the diffusion encoding will also be sensitive to any motion, such as patient motion or cardiac pulsations. To freeze bulk motion, single-shoot (SS) techniques with rapid readout, commonly echo-planar imaging (EPI), are often used. However, SS-EPI is inherently prone to image degrading artifacts from B_0 susceptibility artifacts and induced eddy-currents from the strong and rapidly shifting diffusion-encoding gradients. Additionally, the T2* relaxation during the long signal readout causes blurring and limits the image resolution.

As dMRI is inherently a low signal technique with a low signal-to-noise ratio (SNR), special considerations have to be taken into account when designing the sequence protocol to optimize the study and to minimize image artifacts. Parallel imaging (PI) techniques (167,168) can be applied to shorten the echo spacing and readout time, which will improve image quality, even with modest reduction factors (R = 2), for a slight penalty in SNR (169). Multi-shot

techniques with segmented readouts are a promising recent advance, especially for high-resolution dMRI with low image distortions (170). Eddy currents can be effectively minimized by applying a twice-refocused SS-EPI sequence (171), although with an increase in echo time. The susceptibility-induced off-resonance field effects can be estimated by acquiring additional b=0 image/s with reversed phase-encoding polarity (172), and to a large degree adjusted in post-processing steps (173).

3.3.2.2 Diffusion tensor imaging

The diffusion tensor was introduced in the early 1990's to model the diffusion properties of water molecules in brain tissue in dMRI (174), and is referred to as diffusion tensor imaging (DTI). Diffusion tensor imaging has had an enormous impact in the field of dMRI, and forms a central part of this thesis.

The simplest model to describe a 3-dimensional random-walk is the diffusion tensor **D**. **D** is a 3x3 symmetric matrix which generalises Einstein's equation as

$$\mathbf{D} = \begin{bmatrix} D_{xx} & D_{xy} & D_{xz} \\ D_{xy} & D_{yy} & D_{yz} \\ D_{xz} & D_{xy} & D_{zz} \end{bmatrix} = \frac{1}{6t}\langle \mathbf{r}\mathbf{r}^{\mathrm{T}} \rangle,$$

where **D** becomes the covariance matrix of the displacement vector **r**. The diffusion tensor **D** describes a Gaussian diffusion process (i.e. random-walk) with zero mean, and generalises the signal attenuation equation under this assumption as

$$S_b = S_0 e^{-b\frac{\mathbf{g}^{\mathrm{T}}\mathbf{D}\mathbf{g}}{|\mathbf{g}|^2}}$$

where $\mathbf{g}/|\mathbf{g}|$ is the normalized diffusion gradient vector, i.e spatial direction along which the tissue diffusion processes is studied. The diffusion tensor **D** is symmetric matrix with real-valued entries (i.e. positive definite matrix) and can thus be diagonalised into a set of real-valued positive eigenvalues (λ_1,λ_2,λ_3) and corresponding eigenvectors ($\mathbf{e}_1$,$\mathbf{e}_2$,$\mathbf{e}_3$). The tensor model provides an illustrative description of the diffusion process as the eigenvalues and eigenvectors describe the radii and principal axis of the diffusion ellipsoid (Figure 3-4, p. 49). Cases when $\lambda_1 > \lambda_2, \lambda_3$ represent an elongated, cigar-shaped diffusion ellipsoid, suitable for describing the anisotropic diffusion in coherent, parallel WM axons (Figure 3-4, p. 49). In cases where $\lambda_1 = \lambda_2 = \lambda_3$, the diffusion ellipsoid turns into a sphere, which describes an isotropic diffusion process, e.g. in GM. For cases in which $\lambda_1 \approx \lambda_2 > \lambda_3$, the diffusion ellipsoid turns into an oblate/saucer (one example in Figure 3-6, p. 53), which has no real structural equivalent.

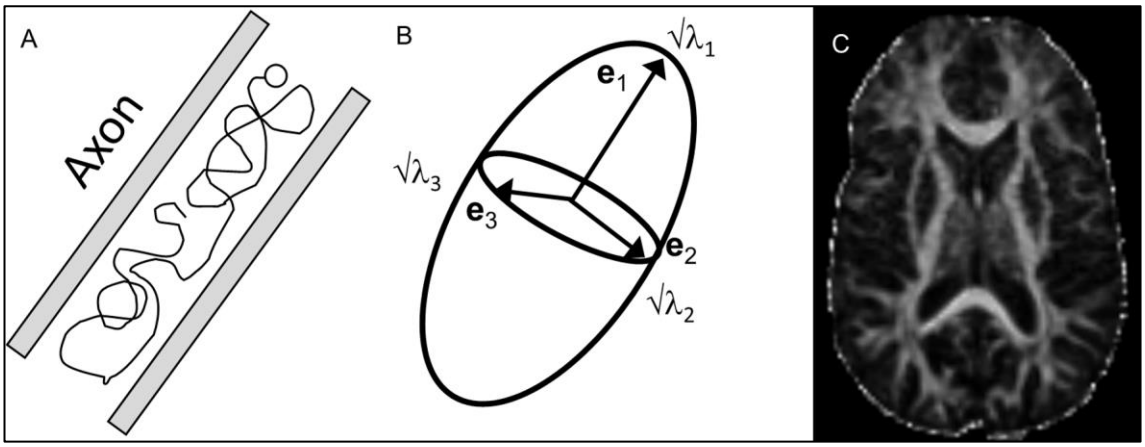

Figure 3-4: The diffusion process in (A) a single axon and (B) its tensor ellipsoid estimation (eigenvalues $\lambda_1, \lambda_2, \lambda_3$ and eigenvectors e_1, e_2, e_3). (C) Fractional anisotropy (FA) map illustrating the anisotropy of the tensor in an axial brain slice. Note the high FA values in the central, coherent WM fibre bundles (e.g. internal capsule and the genu and splenium of the corpus callosum) and the low FA in parts of the periventricular WM where major WM fascicles cross.

The diffusion tensor provides a set of useful, rotationally invariant scalar parameters for describing different characteristics of the diffusion process (175). The mean diffusivity MD is calculated from the trace of **D** as

$$MD = \frac{1}{3} trace(\mathbf{D}) = \frac{1}{3}\left(D_{xx} + D_{yy} + D_{zz}\right) = \frac{1}{3}(\lambda_1 + \lambda_2 + \lambda_3)$$

The axial diffusivity $ADC_{//}$, or $D_{//}$, can be estimated as the value of the largest eigenvalue ($D_{//} = \lambda_1$), and the radial diffusivity $ADC_{\perp}$, or $D_{\perp}$, as the mean of the second and third eigenvalues ($D_{\perp} = (\lambda_2+\lambda_3)/2$). The fractional anisotropy index (FA) is frequently reported, and is given by

$$FA = \sqrt{\frac{3}{2}} \sqrt{\frac{\left(\lambda_1 - \bar{\lambda}\right)^2 + \left(\lambda_2 - \bar{\lambda}\right)^2 + \left(\lambda_3 - \bar{\lambda}\right)^2}{\lambda_1^2 + \lambda_2^2 + \lambda_3^2}}$$

where $\bar{\lambda} = (\lambda_1 + \lambda_2 + \lambda_3)/3$. The FA is a unitless scalar in the range 0 to 1, which geometrically describes the elongation/pointedness of the tensor ellipsoid from the inter-relation of the eigenvalues. FA can capture the degree of anisotropy of the diffusion process: FA=0 describes a sphere (i.e. isotropic diffusion process), and FA close to 1 describes an elongated diffusion ellipsoid (highly anisotropic diffusion process). In the brain, FA is large in areas of highly organized and coherent WM tracts (Figure 3-4C), e.g. the corpus callosum, and is sensitive in reflecting small inter-eigenvalue changes, which can be related to underlying structural changes to the nerve tissue structure. FA maps can be used both for quantitative measurements and for visualisation. Directionally encoded colour maps (DEC) are colour-coded according to the orientation of the principal eigenvector (176), and are useful for visualisation of DTI data. Conventionally, a red-green-blue colour-scheme is used, in which the right-left direction is coloured red, the anterior-posterior direction is coloured green, and the superior-inferior direction is coloured blue (for illustrations see Figure 3-9, p. 66).

The tensor model contains 6 unknowns (3 diagonal quadratic terms and 3 off-diagonal cross-terms), and including the b=0 image, a total of 7 measurements is needed to fully determine the entries in the diffusion matrix. As dMRI is inherently noisy, it is generally recommended that more than 7 measurements are acquired in order to achieve robust estimates of the diffusion tensor or the calculated scalar parameters. Generally, around 25-30 gradient directions sampled uniformly on the sphere with one b=0 image per 5 (177) or 7-8 directions (178) is recommended. The optimal b-value in a two-shell acquisition (first shell is b=0) for characterizing the diffusion tensor, tensor parameters and fibre orientation, is in the range 700-1300 s/mm^2 (177). In clinical practise, b=1000 s/mm^2 is used, dropping to around b=700 s/mm^2 in young children and newborns, due to the generally increased water content in their brain tissue.

As outlined above, the tensor model describes one single, free Gaussian diffusion process. Using the tensor model to fit the dMRI data has clear limitations. Primarily, in voxels with complex fibre architecture, the tensor model can only model the dominating fibre population. Even so, changes to DTI parameters can be due to changes in any of the underlying fibre populations, and, thus, have to be interpreted with care (179–181). In voxels with several equivalent fibre populations, the simple interpretation of the tensor model breaks down completely. An illustrative example are the low FA values in the periventricular WM in areas of the crossroads of the large white matter fascicles (example in Figure 3-4C, p. 49). Moreover, the diffusion of water in brain tissue is not free diffusion; instead, as described earlier, it is multifactorial, with several contributing factors leading to deviation from Gaussian behaviour. To address both these problems, more elaborate diffusion models have to be considered. Nevertheless, despite its shortcomings, DTI is an invaluable tool for investigating the brain tissue structure.

An extension of DTI is diffusion kurtosis imaging (DKI), where the 2nd order diffusion tensor is complemented with a 4th order kurtosis tensor (182). The kurtosis tensor can capture non-Gaussian diffusion, and, therefore, better describe the diffusion process in brain WM tissue. As a result, DKI can provide measures better related to the neuronal microstructure (183). An advantage of DKI is that it can be implemented in a clinical setting, using a multi-shell acquisition with b-values in the range 0-3000 s/mm^2. Around 30 directions in 3-5 shells is sufficient, making it comparable to a HARDI-acquisition (see 3.3.2.3) in terms of scan time. Even though DKI can characterise a non-Gaussian diffusion process, and provides parametric measures that have proven sensitive and specific to various pathological conditions (183), DKI is a mathematical expansion of the dMRI signal as a function of the b-value and does not bear any biophysical modelling. DKI should therefore be interpreted with caution.

3.3.2.3 Higher-angular resolution diffusion-weighted imaging

This thesis focuses on white matter fibre tractography, where the issue of complex fibre architecture, primarily crossing fibres, is a major concern. Models for resolving crossing fibres are therefore discussed here.

Under certain conditions (the narrow pulse approximation - i.e. gradient duration δ is short), the dMRI signal-attenuation in the PSGE diffusion-sequence can be viewed as the Fourier transform of the diffusion spin displacement propagator *P* as

$$S(\mathbf{q},\mathrm{t}) = S_0 \int_{\mathbb{R}^3} P(\mathbf{r},\mathrm{t})\, e^{-i\mathbf{q}^{\mathrm{T}}\mathbf{r}} d^3\mathbf{r}$$

Here S_0 is the b=0 image, $\mathbf{q} = \gamma\delta\mathbf{G}$ is the q-space vector, given by the nuclear gyromagnetic ratio γ, the applied **G** diffusion gradient and its duration δ. The diffusion spin propagator $P(\mathbf{r},t)$ describes the likelihood of encountering the diffusing water molecules at a certain position **r** at a certain point in time *t*. $P(\mathbf{r},t)$ is thus the displacement probability density function (dPDF) for the diffusion process, and, if we could calculate it, would fully describe the diffusion process in the voxel (Figure 3-5). Presumably, the dPDF would then reflect the underlying neuronal structure. The q-space formalism in dMRI represents a Fourier-dualism between the dMRI signal and the diffusion spin propagator; this mirrors the k-space formalism in image formation in MRI (see 3.3.1.2). By sampling the dMRI signal in q-space, the dPDF can be estimated by taking the inverse Fourier-transform of the dMRI signal.

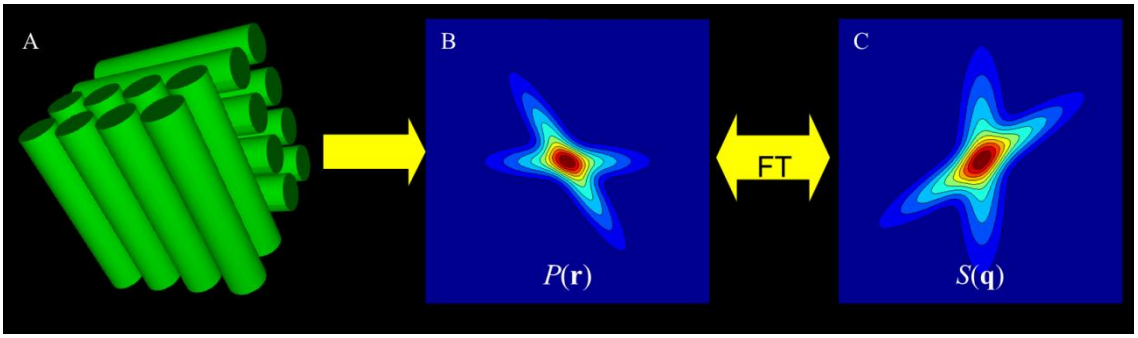

Figure 3-5: Showing (A) a voxel with two crossing fibres, (B) the corresponding spin propagator *P*(r) and (C) its Fourier pair which is the measured MR-signal *S*(q) in q-space. FT=Fourier transform. Courtesy of JD Tournier.

This is the basis for diffusion spectrum imaging (DSI) (184), which is a powerful means for estimating the diffusion process in brain tissue. However, collecting an entire DSI dataset takes ~ 30 minutes, which is not feasible in a clinical setting.

As the structure of both the dMRI signal and the spin propagator (Figure 3-5) contain a wealth of directional information, an alternative approach is to sample the dMRI signal on a q-sphere (i.e. fixed $|\mathbf{q}|$ but varying the angle of inclination) for a sufficiently high b-value. This allows the rich orientational information in the spin propagator to be appreciated, and the diffusion orientation distribution function (dODF) of the spin propagator can be estimated instead. The dODF relates, in turn, to the underlying fibre orientation distribution function (fODF or FOD), which describes the orientational organization of the different fibre populations in the voxel. This is the object of high-angular resolution diffusion-weighted imaging (HARDI), with a primary focus on resolving the issue of crossing fibres in dMRI.

HARDI techniques commonly try to infer the angular information of the spin propagator, either by estimating the FOD directly, or via the dODF of the spin propagator. There is an im-

portant distinction between the FOD and dODF. The FOD quantifies the fraction of fibres in a voxel pointing in certain direction, and is, thus, a distribution function on the sphere for the fibre orientations. The dODF, on the other hand, can be viewed as a 2-dimensional radial projection of the (complete) 3-dimensional dPDF, and thus describes the orientational distribution of the spin propagator, given the dMRI data. A HARDI technique should ideally recover the FOD, as it would then describe the different fibre orientations in the voxel as well as their relative volume fraction. However, HARDI techniques calculating the FOD must use some prior assumption/model to link the diffusion process with the underlying fibre structure (i.e. they are not model free). Estimating the dODF requires no model assumption, but often makes the much more simplistic assumption that the underlying fibre orientations coincide with the peaks of the dODF. However, the dODF is typically broader than the FOD.

HARDI techniques can be divided into model-based or model-free methods (185). Model-based methods can be parametric or non-parametric (often referred to as mixture models), whereas model-free methods are non-parametric. Instead of fitting a parametric model to the dMRI signal, non-parametric methods estimate a continuous FOD, either directly (model-based methods) or by calculating the dODF (model-free methods). By using a non-parametric model, fewer constraints need to be placed on the algorithm, and a continuous f/dODF can be estimated, which provides better insight into the underlying fibre configuration (185).

A common requirement for HARDI, regardless of algorithm, is that the diffusion-weighting is sufficiently strong, and that the sphere is sufficiently sampled. A rule of thumb is b-values around 2000-3000 s/mm^2 and $\geq$ 60 gradient directions. This makes HARDI techniques applicable for clinical imaging times, and a high-quality dataset can be acquired in ~ 10 min. Several HARDI methods have been implemented for multi-shell acquisition (multiple b-values).

The model-based HARDI techniques try to resolve the crossing fibre issue by modelling distinct fibre populations separately. One extension of DTI is to use multi-tensor models as a mixture of weighted Gaussian diffusion models. This may seem like a straight-forward approach, however, the models will be limited, as for the single-tensor model, by non-Gaussian behaviour of the dMRI signal. Further, the multi-tensor models cannot be solved using a simple log-linear least-squares fit, commonly used for the single tensor model, and instead, non-linear optimization techniques have to be used to find solutions, which are often unstable for the noisy dMRI data.

Related to the multi-tensor approach is the CHARMED (combined hindered and restricted model of diffusion) model (186), which models the dMRI signal as a combination of an hindered extra-cellular compartment and a restricted intra-cellular cylinder-shaped compartment. The main purpose of the CHARMED model is to probe the tissue microstructure with dMRI, and provide estimates for relevant parameters such as the axonal density, the diffusivity of the extra-axonal compartment (hindered diffusion) and the fibre orientations. In the modified framework of AxCaliber (187), the axon diameter can be estimated (it is fixed in CHARMED). Both methods, especially CHARMED, require extensive q-space sampling, which is in general not feasible in a clinical setting, although optimized acquisition schemes

have recently been suggested (188). Another recent composite model is neurite orientation dispersion and density imaging (NODDI) (189), which allow estimations of neurite angular dispersion (i.e. the spread in fibre direction) and neurite density with a three-shell acquisition (e.g. 30 directions at b = 1000 s/mm^2 and 60 directions at b = 2000 s/mm^2) within a clinical setting (10-30 min). Diffusion models, including DKI (see 3.3.2.2), that probe the microstructure of neuronal tissue are an active area of research, but their clinical use remains limited by the lengthy acquisition schemes needed in many cases.

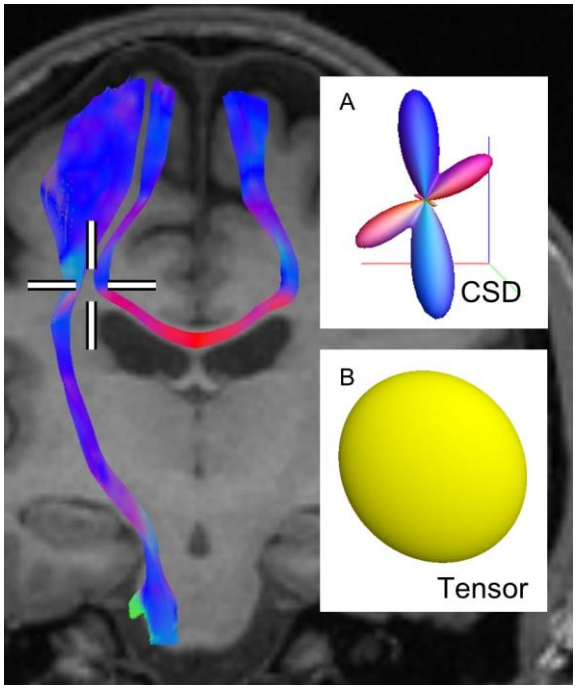

Figure 3-6: Figure showing the accurate (A) CSD and inferior (B) tensor estimations in a voxel with crossing fibres (hair cross). The underlying picture shows deterministic tensor tractography of the CST and transcallosal fibres. This displays the tensor tractography method's inability to track through areas with complex fibre architecture. CSD=constrained spherical deconvolution.

One simple multi-tensor model is the "ball-and-stick" model (190), which assumes that data either comes from a population with free isotropic diffusion in and around axons (the ball, fitted to an isotropic Gaussian model), or from a population that only moves along the axon (the stick, fitted with a Gaussian model with a single, non-zero eigenvalue). Several sticks could be added to model multiple fibre populations (191) to deal with crossing fibres. The model has also been adapted to multi-shell acquisitions and improved to overcome the fitting problem (192). The "ball-and-stick" model is simple, but has proven efficient in resolving crossing fibres, also for lower b-values (193). The model, with its extensions, is implemented in the FSL software package (194). In this thesis, the original multi-fibre model (191) was used in the first study (Study I).

A group of HARDI models are the non-parametric methods, such as DSI (184), Q-ball (195), and PAS-MRI (196), that try to recover the dODF rather than the FOD. Spherical deconvolution (SD) techniques are non-parametric methods that try to recover FOD directly (197) by deconvolving the dMRI signal on the sphere. The convolution kernel, or response function, is estimated from the response for a single fibre population, which becomes the model part (hence the label mixture model). SD techniques are slightly different depending on which basis function they use (most common is the spherical harmonics), and how they estimate the response function. However, the deconvolution operation causes the assumption that the measurement can be seen as a weighted sum of the individual measurements for each fibre population, i.e. a linearity assumption. This also assumes that there is no, or a negligible, exchange between the fibre populations during the diffusion process (so called slow-exchange assumption), which is generally met in a clinical situation (diffusion time ~ 50 ms). The SD models are powerful, since they estimate the FOD directly. The FOD has better angular definition than the dODF, and can therefore distinguish fibre populations more accurately. The

SD is sensitive to noise. As a result considerable improvements have been developed using regularization methods, e.g. in constrained super-resolved spherical deconvolution (CSD) (198). However, the single-fibre voxels used for the calibration have to be chosen carefully (199), and may also have to be considered in cases of diffuse, widespread WM pathology. CSD is capable of accurately resolving crossing fibres down to an angle of 30-40° (200). For a comparison of the tensor model and the CSD, see Figure 3-6 (p. 53).

In this thesis, the implementation of CSD in the MRtrix software package (201) was used for the last three studies (Study II-IV).

3.3.2.4 White matter fibre tractography

One of the most exciting applications of dMRI is white matter fibre tractography. This application allows the study of individual white matter fibre tracts non-invasively, *in vivo*, and has given scientists and clinicians new insights into the WM structure in the normal brain, in disease and during brain development. This section outlines conventional streamline tractography, followed by a discussion on visual evaluation of tractograms.

The rich orientational information in the dMRI signal, as discussed earlier, can be used to convey directional information on the underlying fibre populations in every voxel, and presents this in a vector field. In DTI, the principal eigenvector (i.e. the long axis of the diffusion ellipsoid) is used to estimate the underlying fibre orientation, whereas in HARDI the individual peaks of the FOD/dODF (depending on the algorithm) are used. In a stepwise algorithm, a 3-dimensional trajectory in space, a streamline, is generated by following the estimated fibre direction point by point, as given by the vector field. This process is referred to as streamline tractography (202) (Figure 3-7, p. 55). The tracking algorithm is initiated from a starting (seed) point, and run iteratively until stopping criteria are met (e.g. leaving the white matter or reaching a termination ROI). This can either be done in a deterministic way, by following the most probable direction (202), or in a probabilistic manner, by sampling the calculated PDF (FOD or dODF usually). The methods are hence referred to as deterministic and probabilistic fibre tractography respectively. The tracking algorithm is repeated for large number of streamlines. Seed points, inclusion/exclusion rules, and termination criteria are user-defined inputs to the fibre tracking algorithm. The set of accepted streamlines, a tractogram, is the final result and is considered to represent the underlying fibre tract. Inputs are often tailored, based on assumptions of the underlying neuroanatomy, to generate a desired tract. Whole-brain tractograms can be generated by random seeding in all brain voxels.

Tracking algorithms are typically prone to both false positives (non-physiological tracts/parts of a tract) and false negatives (failure to generate tracts/parts of a tract). The latter is common in deterministic tensor tractography, and, to a lesser extent, in probabilistic approaches, whereas the former is primarily a problem for probabilistic tractography. By the method's nature, tracking algorithms will oversample the shortest, simplest and straightest path (203), resulting in more elaborate connections being undersampled. The streamline count (i.e. number of accepted streamlines) is, therefore, primarily a measure of the reproducibility of the

tracking algorithm and not a measure reflecting the underlying numbers of axons, and should not be reported as such (204). Errors, or inadequacies, in the PDF estimation will also be reflected in the tractogram. Similarly, there is a propagation of uncertainty with the tracking distance (205) in the probabilistic tractogram, i.e. the cone of streamlines will grow as the tracking progresses through the PDF field. This will lead to a gradual decrease in the probability of connection with distance (e.g. if measured as the fraction of passing and accepted streamlines). In conclusion, the tracking result has to be judged wisely, both for deterministic and probabilistic tractography. However, the most realistic reconstruction of white matter fibre tracts is achieved with probabilistic fibre tractography in a diffusion model capable of resolving crossing fibres. Illustration of these problems are shown in Figure 3-7.

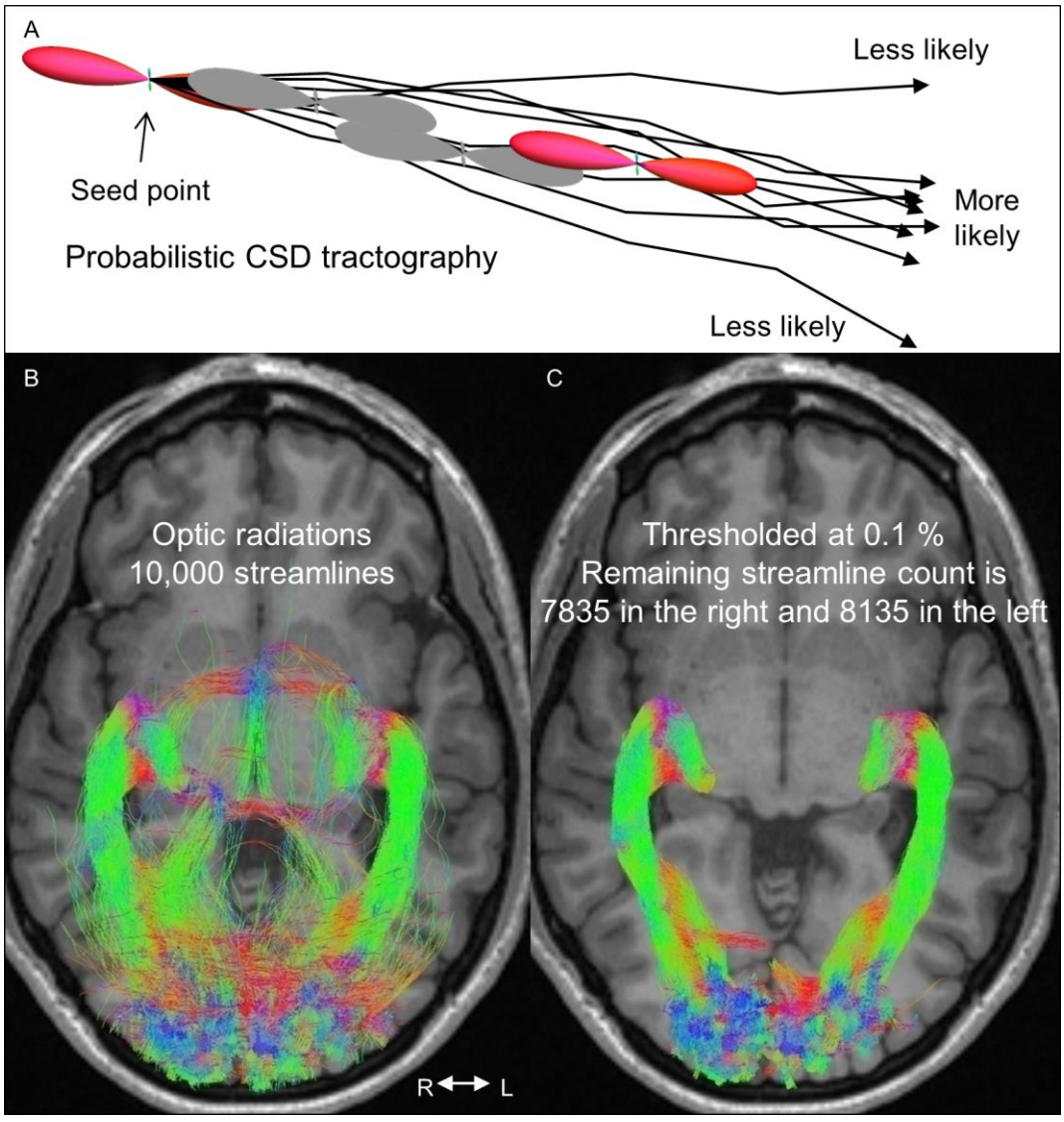

Figure 3-7: Probabilistic CSD tractography. (A) Shows a set of streamlines generated from the same seeding point. Notice the gradual spatial spread among streamlines with tracking distance, and the separation into sets of more and less likely connections (the latter probably false positives). (B) Probablistic CSD tractography of the optic radiations (OR). (C) Notice the effective pruning of the OR tracts from false positive when thresholded at a 0.1 % visitation count. CSD=constrained spherical deconvolution. R=right, L=left. Courtesy of JD Tournier

White matter fibre tractography can reconstruct the major fibre bundles in the brain (206,207), and guidelines have been published to reliably reconstruct most white matter tracts (208,209), or more specific tracts, like the optic radiation for HARDI-techniques (210).

Visual inspection of a tractogram is the first quality check to see whether the tracking has been successful. The tracking procedure is often iterated by changing the input slightly until the desired result is achieved. It is important to remember that the tractogram is an estimate of the fibre trajectories, given the dMRI data, and does not represent the axons themselves. Therefore, the tractogram has to be compared with the expected neuroanatomy, and judged thereafter with respect to its structural morphology and occurrence of false positives (spurious tracts) or possible false negatives (absent parts). The aim should be to reconstruct the tract as accurately as possible. However, anatomical validation of tractography is problematic in humans as a gold standard to compare with, e.g. histology tracer studies, does not exist (185). Comparisons between tractograms and blunt dissection of human brains give similar results (211), although both techniques have problems in areas of more complex fibre architecture, such as crossing fibres. Other techniques to assess the validity of fibre tractography include connectivity-based parcellation of brain structures with known connections. This has produced anatomically relevant results for several brain structures. One early study parcellated the thalamus depending on its (most likely) cortical projections, and showed high agreement with the known thalamic nuclei (212). Indirect validation can be done with functional techniques (e.g. fMRI, electrical or magnetic stimulation). Such studies show that the tracking results are in general agreement with the functional data, but not necessarily identical (213). Similarly, the anatomical relationship between the different components in a tract, or adjacent tracts, commonly overlap and share voxels (214). In conclusion, visual inspection of a tractogram is valid, primarily as a quality check, but can be used in a qualitative descriptive study design to compare tracts with the expected anatomy and between individuals. However, additional analyses have to be carried out to infer the finer structure of a tract.

Tract density images (TDI) (215) with voxel values equal to the number of passing streamlines can be generated, and provide a high-resolution visualisation tool of the finer tract structure. The concept of TDI maps can be generalised, as any tract characteristic can be mapped into a "TDI"-like map to produce a large range of contrasts (216). The TDI map can serve as a tract probability map and be used to filter the tractogram from low probability streamlines, typically false positives (217). This is illustrated in Figure 3-7 (p. 55).

In this thesis, the fibre tractography methods have been tailored in every study to achieve the most accurate and reproducible delineation of the tract of interest. This has been important, as all studies have contained relatively few participants, so that systematic errors in the method did not decrease the statistical power. For improved input to fibre tractography, ROI-definition was done in a study-specific template in one study (Study II), and as cortical activation maps from retinotopic fMRI in another (Study IV). One study used manually drawn ROIs for input (Study I), and two studies used manually defined locations for ROIs (centre of lateral geniculate nuclei in Study III & IV and centre of occipital pole in Study III). Exact details on the fibre tracking methods for each study are given in 3.3.4.

3.3.2.5 Changes in diffusion parameters in white matter upon injury

Diffusion-weighted MRI (dMRI) is sensitive to changes to the water molecules' diffusion properties in brain tissue after injury, both in grey and white matter. This thesis concerns mainly end-stage imaging of early brain injuries, with the focus on major white matter fibre tracts. This section outlines diffusion changes in the brain WM at this stage.

In white matter with coherent, parallel neuronal axons, changes in $ADC_{//}$ are mainly related to the axonal membrane, whereas changes in $ADC_{\perp}$ primarily reflect changes in myelination (157,218). This has been observed in different species (157), under different genetic conditions of dysmyelination (219,220), and in human brain development (160). This is also reflected in the evolution of secondary anterograde (Wallerian) degeneration. Early work has been done by Song et al (221) studying the time course of secondary anterograde degeneration in the rat optic nerve after retinal injury. They could see that the early axonal degeneration, within days, caused an decrease in $ADC_{//}$, which is followed in the chronic phase after around 2 weeks, by an increase in $ADC_{\perp}$, depicting the myelin degradation. The degree of anisotropy (e.g. FA) and MD changes accordingly. The same pattern can be seen in human lacunar strokes with DTI (222). The end-stage pattern after secondary anterograde (Wallerian) degeneration in single fibre populations showed a large increase in FA, a decrease in axial diffusivity $D_{//}$, an increase in radial diffusivity $D_{\perp}$, but only subtle changes in MD. Pierpaoli et al (181) also showed that at the primary lesion site both $D_{//}$ and $D_{\perp}$ are increased, causing a large increase in MD and a drop in FA due to a general loss of coherence. The DTI changes presented by Pierpaoli et al are commonly regarded as reflecting changes in primary neurodegeneration from destructive injuries and distant, secondary neurodegeneration. The changes are summarized in Table 3-1.

DTI parameter	Primary neurodegeneration	Secondary neurodegeneration
Mean diffusivity (MD)	Large increase	No/Small increase
Fractional anisotropy (FA)	Large decrease	Large decrease
Axial diffusivity ($D_{//}$)	Increase	Decrease
Radial diffusivity ($D_{\perp}$)	Increase	Increase

Table 3-1: DTI parametric changes in a single fibre population after primary and secondary neurodegeneration. The parametric changes in primary neurodegeneration are due to a general loss of tissue coherence. The decrease in axial diffusivity and increase in radial diffusivity in secondary anterograde degeneration are chiefly due to the degeneration of the axons and the subsequent demyelination respectively. Based on (181,223).

However, it is important to remember that similar, or even identical, patterns of DTI changes are seen in a wide range of diseases, reflecting different pathological events. Therefore, a generalisation from one disease model to other may not hold.

Moreover, the interpretation of DTI changes are less straightforward in areas of crossing fibres (179–181). In fact, a decrease in FA can be caused by a decrease in $D_{//}$ in a dominating fibre population, or due to an increase in $D_{//}$ in a non-dominating fibre population, thus re-

flecting completely different underlying physiological changes. Similarly, a change in the relative volume fraction of different fibre populations in a voxel can change a DTI parameter. Moreover the tensor-based MD (i.e. $MD = 1/3\,\mathrm{Trace}(\mathbf{D})$) is dependent on the underlying fibre structure (224). Despite this, DTI parameters are useful in detecting diffusion changes, both within and between subjects, but need to be interpreted with caution.

Spherical deconvolution can also provide relevant parametric measures (225,226). The changes in the dMRI signal, particularly the intra-cellular component at higher b-values, are translated into changes in amplitude of the corresponding FOD amplitude of that fibre population. A clear demonstration of this was shown in the original paper on apparent fibre density (AFD) by Raffelt et al (225). In patients with motor neuron disease, specifically amyotrophic lateral sclerosis (ALS), the FOD-lobes corresponding to both the descending projection fibres from, and the transcallosal commissural fibres in-between, the primary motor cortex/cortices had decreased amplitude compared to controls. This could be seen in areas of crossing fibres. However, the methods require normalization of the FODs (225) for cross-subject comparisons, which may not be straightforward, especially not in populations with wide-spread pathological changes. Nevertheless, higher order models, such as CSD, would aid to the understanding of primary and secondary changes in early brain lesions.

Similar to other dMRI studies on early brain lesions (see section 1.3.2), this thesis has used DTI parameters for statistical comparison within and between study groups (Study I, II & IV). DTI parameters are sensitive in detecting changes related to injury, but have clear limitations in depicting the actual underpinnings of the change. All studies have therefore clearly stated whenever the interpretation of the DTI changes could be doubted. In the last study (Study IV), the higher-order model AFD (225) with the implementation of AFD connectivity (afdconnectivity command in MRtrix3; https://github.com/MRtrix3/mrtrix3) was used to better probe changes in the optic radiations.

3.3.2.6 Cross-subject comparisons of diffusion parameters

Different approaches can be used when comparing diffusion parameters between groups. Methods relevant for this thesis are outlined here.

Voxel-based whole-brain techniques for cross-subject comparisons of dMRI data using traditional voxel-based morphometry (VBM) approaches (227) are generally discouraged, due to the problems in normalization of dMRI data, and the non-Gaussian distribution of the voxel values in the DTI parametric maps (228,229). Tract-based spatial statistics (TBSS) (230) is an alternative method, in which cross-subject comparisons are carried out on a study-specific template, a mean FA-skeleton, which to a large extent overcomes the normalization issues. DTI parameters are then projected on the FA-skeleton, and can be compared between subjects, significantly reducing the problem of multiple comparisons in TBSS. TBSS has gained considerable popularity as an objective, simple method for group analysis of "whole-brain" DTI changes in major white matter tracts. However, this method is completely dependent on the success of the FA-skeletonization procedure, which is not guaranteed in voxels affected

by disease. Moreover, the tensor model has limitations in voxels with complex fibre architecture, and hence the TBSS results always need to be interpreted with extreme care.

A region-of-interest (ROI) is a specific volume/area of voxels for which a parameter can be calculated, often as the mean or median value of a diffusion parameter, and then compared. ROIs can be manually defined, tract-defined (as the spatial extent of a fibre tract), or defined from some other criteria (e.g. activation map on fMRI). ROI-based comparisons reduce the problem of multiple comparisons, but introduce a prior bias. However, this may be a relevant approach if the research hypothesis concerns a specific area/tract. Defining ROIs by hand is time consuming and requires expertise, and even so, the reproducibility may be limited and should be reported. Tract-based ROI definition is expected to be more precise, since the fibre tracking algorithm is automated, and more accurate, since the structure of interest can be targeted. In studies (231), tract-based ROI definition has proved more sensitive than manual ROI definition. The fibre tracking algorithm requires input, commonly user-defined ROIs, for seeding streamlines. Probabilistic fibre tracking is, in general, less sensitive to the input, as the algorithm will primarily find the connections of highest probability (203). So, by ensuring that the input ROIs are not too restricted (i.e. have good anatomical coverage), the core of the tract is retrieved. This is also my personal experience. Alternatives to manually drawn ROIs are ROIs based on activation maps from fMRI, which represent relevant functional activity. However, the localization of functional areas with fMRI is not perfect, the resolution is often relatively poor, and is not certain that fMRI would elicit a functional response in all cases, especially in patient groups.

Many studies using tract-based ROIs extract diffusion parameters as the average, or the median, over large parts of the tract. This might be misleading, as DTI parameters vary along a tract, both naturally and depending on the voxel fibre composition, which translates into the diffusion tensor (e.g. in areas with crossing fibres). Wakana et al (208) illustrate this in deterministic tensor reconstructions of the cortico-spinal tract (CST), anterior thalamic radiation, and the inferior fronto-occipital fasciculus. Along all these tracts, the FA varies slightly but sharply in areas of crossing fibres. At the same time, the measured T2-values showed minor, slower variations along the entire tracts. Nevertheless, these tract-parameter profiles were highly reproducible and tract-specific when studied in a normal adult population. Wakana et al showed, with power calculations[1], that the numbers needed to detect a 10-20-40 % change in FA in CST were no more than 6-4-4 subjects at significance level $p = 0.05$ and power = 0.8 (208). Heiervang et al (232) systematically investigated the in-between subject variability for tract reconstruction using probabilistic tractography in the single-fibre "ball-and-stick" model (190) in a number of tracts. They showed that for the CST, the numbers needed (given as the

[1] Power calculations refers here to post-hoc estimation of the sample size required to yield a certain power for a test, e.g. rejecting the null hypothesis at a certain significance level p.

average left and right) to detect a 2-5 % change in FA and in MD were around 4.5-3 and 9.5-3 respectively for (one-tailed) a significance level p = 0.05 with power = 0.8. For the optic radiation, corresponding numbers detecting a 2-5 % change in FA and a 2-5-10 % change in MD were 8.5-3 and 18-5.5-3.5 respectively. High reproducibility for tracts and DTI parameters have also been reported for HARDI-techniques, including CSD (233), and in the OR for Q-balls and PAS-MRI (210). However, no power calculations were reported. In summary, provided that the tracking method has high reproducibility, the DTI parameters extracted show high reproducibility and are sensitive to change. When studying DTI changes in disease however, the statistical power increases when tract regions most affected by disease are targeted specifically.

When the same tract is reconstructed in multiple data sets, the precision in the ROI definition in every data set (the "native" space) can be improved by defining the ROI in a common space (a standard space or a study-specific template) (217), and mapping this into each subject's native space. By using a standard space (e.g. Talairach or MNI), ROI-atlases can be used to define relevant brain regions. Tracking can, in theory, be performed in a common space, but requires a registration algorithm that preserves the full information in the diffusion model (234). Tracking is therefore usually performed in native space, and tracts can then be mapped into a common space for further analysis.

In this thesis, ROI-based comparisons of diffusion parameters have been used, both by using manually drawn ROIs (Study I) and tract-based ROIs (Study I & II and IV).

3.3.3 Retinotopic functional magnetic resonance imaging mapping

The organization of the visual cortex into visual field maps can be investigated with retinotopic functional MRI (fMRI) mapping (27,235). Abnormalities in retinotopic fMRI maps are in good correlation with visual field (VF) defects measured with visual perimetry (236–238). In Study IV, retinotopic fMRI mapping was used to define the primary visual cortex (V1) to study the retinotopic organisation in the optic radiation. This section will give a brief outline of the technique of retinotopic fMRI mapping.

Neuronal activity is energy-requiring, with metabolic changes in neurons and astrocytes at and around the synapse after neurotransmitter release (239). The brain uses, ultimately, oxidative metabolism, and an increased oxygen delivery is needed to the site of the active synapses. However, normal oxygen delivery by transcapillary diffusion cannot meet these demands. Instead, by means of the neuro-vascular coupling, excessive amounts of oxygenated blood is pooled to the capillary bed to increase the diffusion pressure, with the result of an increased blood volume in the post-capillary venules and draining veins. This results in a net increase in the ratio of oxygenated to deoxygenated blood in the area, mainly located on the venous side, which in turn causes a shift in the local magnetic susceptibility (slight decrease of the dominating paramagnetic effect from the deoxygenated blood). The shift in magnetic susceptibility can be imaged with MRI to create images with a subtle increase of the MR sig-

nal (~ 2-3 % at 1.5 T). The effect is referred to as blood-oxygen level dependent (BOLD) response (240), and the MRI technique, BOLD functional MRI (BOLD-fMRI)

The BOLD response profile upon neuronal activity is the so called haemodynamic response. It typically shows a brief initial dip at 0.5-1 s after stimulus onset, before a sharp increase and overshoot to yield a stable positive BOLD response, peaking at around 5-8 s, and a post-stimulus undershoot returning to baseline first after tens of seconds (239).

The time-lag and complexity of the haemodynamic response causes a temporal blurring in the BOLD response in relation to the underlying neuronal activity. Because of this, the relative weak BOLD response and the special demands on the MRI sequences in BOLD-fMRI (not discussed here), the experimental design is often based on repetition of a stimulus, e.g in a block-paradigm (same stimulus is repeated in cycles). By acquiring a large number of fMRI images of the same brain volume, typically every 1-2 s during the experiment, statistical methods can be used to find the brain voxels that correlate in BOLD response with stimulus paradigm. These are the brain activation maps showing the areas activated by the stimulus.

The cortical visual system is ideal to study with fMRI. The location in the occipital lobe, with extension to the parietal and temporal lobes, is accessible (e.g. with dedicated surface coils) and not affected by the susceptibility effects from air cavities in the skull base. Subject compliance is in general good, and several modes of the visual processing can be investigated.

A simple and robust stimulus for retinotopic fMRI mapping is to use contrast-reversing checker-boards of counter-clockwise/clockwise rotating wedges and contracting/expanding rings presented on a uniform grey background (235). The wedge/ring stimulus creates a strong cortical neural response, with a travelling wave of BOLD response sweeping the retinotopic maps in the visual cortex, in the direction of polar angle for the wedge stimulus and along the direction of eccentricity for the ring stimulus. The periodicity of the BOLD-wave equals the duty cycle of the stimulus (i.e. the time for a complete revolution of the rotating rings or for the expanding/contracting rings to go from minimum to maximum eccentricity).

In the first step of the fMRI analysis, the individual fMRI time-series are motion-corrected and realigned (e.g. using FLIRT (241) in FSL). Thereafter, the counter-clockwise wedge and contracting ring stimuli are shifted a few time frames back, and then averaged with the corresponding clockwise wedge's and expanding ring's time-series (242). By performing the time-frame shifting before averaging, a coarse compensation for the hemodynamic response can be made. In Study IV, a shift of 3 time frames for TR = 1.6 s was used, which equalled an estimation for the haemodynamic response of 3*TR = 4.8 s.

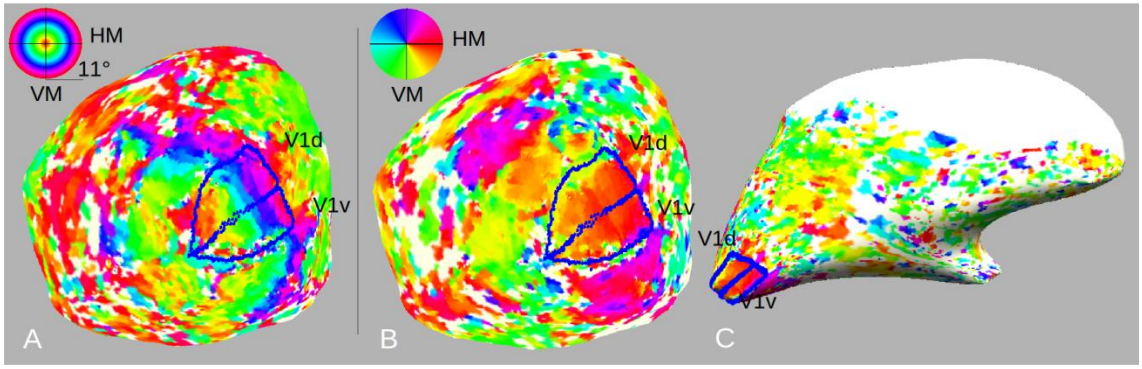

Figure 3-8: Retinotopic fMRI mapping of the right visual hemifield in the left hemisphere. Cortical flattened maps showing phase maps of (A) the ring stimulus, mapping the eccentricity, and (B) of wedge stimulus, mapping the polar angle. The polar angle is also displayed on (C) inflated cortical maps. The retinotopic visual field maps can be defined as the ridges of reversing phase in the (B) polar angle map. Here as the dorsal (V1d) and ventral (V1v) parts of primary visual cortex (V1). V1d- and V1v-ROIs are displayed on all images (A-C). H/VM=horizontal/vertical meridian.

In the next step, a harmonic function with periodicity equal to the number of cycles in the visual stimulus is fitted to the averaged time-series (235). The polar angle and eccentricity will then correspond to the phase of the fitted function. The best visualization of the activation maps is to plot them on a flattened cortical map of the occipital cortex. The visual field maps are then displayed as a continuous phase map (Figure 3-8). The borders between the visual areas can be identified from the ridges of reversing phase (i.e. reversing polar angles) in the phase maps of the wedges stimulus (see Figure 3-8B). The different visual areas can be delineated into region-of-interests (ROIs), and used in analysis or as input to the fibre tracking algorithm.

3.3.4 Data acquisition and data processing (Study I – IV)

Neuroimaging data for Study I & II was acquired on a 1.5-Tesla MR-scanner (Signa Excite Twinspeed), and for Study III & IV on a 3 Tesla MR-scanner, both from GE Healthcare (Milwaukee, WI, USA). The same type of 8-channel head coil was used.

3.3.4.1 Acquisition and visual evaluation of conventional MRI (Study I & II and III & IV)

In Study I & II, conventional MRI included axial and coronal T2w-images, coronal FLAIR images (in-plane resolution 0.43 mm^2 and slice thickness 4 mm, no slice gap for coronal images and 1 mm slice gap for axial image), and 3-dimensional sagittal T1w-image (SPGR; TR/TE=20/5 ms, flip angle (FA)=35°; voxel size 0.86x1x0.86 mm^3), which was reformatted in all imaging planes.

In Study III & IV, conventional MRI included 3-dimensional T1w-images (IR-SPGR; TR/TE/TI= 1986/2.8/450 ms, FA=12°; voxel size 1 mm^3; ARC=1.5 in-plane) and FLAIR images (TR/TE/TI= 8000/117/2257 ms; 1.2 mm^3, reconstructed to 0.6x0.52x0.52 mm^3; ARC=2 in- and through plane), which were reformatted in all imaging planes. In the index group, axial T2w-images were also collected in many cases.

3.3.4.2 Visual assessment of conventional MRI (Study I & II and III & IV)

Early brain lesions seen on conventional MRI were classified as malformations of cortical development, white matter damage of immaturity (WMDI), and grey matter/cortical lesions (33), and considered the primary brain lesion. The timing was judged from the lesion pattern in relation to information of the gestational age, and in relevant cases the birth history. The extent of periventricular WM damage was classified as mild/moderate or severe if less than 50 % or more than 50 % of the bulk periventricular WM was reduced, judged subjectively by visual inspection. Abnormally high signal on T2/FLAIR images in the periventricular WM was considered a radiological sign of gliosis. Associated lesions in the basal ganglia, thalamus, brainstem and cerebellum were noted. In cases of focal infarcts, the vascular territories were reported. In Study III & IV, involvement of the visual pathways was also assessed visually and considered affected if size or MRI appearance were abnormal in the optic chiasm, the optic tracts, the lateral geniculate nuclei (LGN) or the optic radiations (OR).

Radiological assessments in Study I & II were done in a consensus group of two paediatric neurologists and a paediatric neuroradiologist, and in Study III & IV by the primary study rater (Finn Lennartsson, thesis defendant) and discussed with a paediatric neuroradiologist.

3.3.4.3 Data acquisition of diffusion-weighted MRI (Study I & II and III & IV)

In Study I & II and in Study III & IV the diffusion-weighted MRI (dMRI) was collected in conjunction with the conventional MRI. Sequence parameters are given in Table 3-2 (p. 64). They have both similarities and differences.

Diffusion-weighted MRI data in Study I & II was collected during 2007 on a 1.5 T MR-scanner, whereas the imaging data in Study III & IV was collected in autumn 2013 to spring 2014 on a 3 T MR-scanner. Both used the same 8-channel head coil, the same pulse-sequence (twice-refocused SS-EPI), isotropic 2.3 mm^3 voxels and had similar gradient strengths. Study I & II opted for full-brain coverage (64 slices), which then required a TR of 10 s, whereas Study III & IV only needed coverage of the superior fossa requiring fewer slices (~ 50), which could reduce the TR substantially, and hence the scan time. The total scan times were similar: 8:30 min in Study I & II and around 9 min in Study III & IV. Study I & II was optimized for DTI analysis and for probabilistic fibre tracking with the "ball-and-stick" model (191) and used 45 gradient directions at a b-value of 1000 s/mm^2. Study III & IV used a HARDI-protocol with 60 directions at a b-value of 2200 s/mm^2 for fibre tracking with CSD (198). Using 3 T in Study III & IV meant a boost of signal, but increased the problem with susceptibility induced field offsets due to the higher field strength and the longer TE from using a higher b-value, resulting larger image distortions. Therefore, parallel imaging was employed (in-plane, R=2) to reduce the echo spacing and the readout time. Two additional 2 b=0 images with a reversed phase-encoding polarity were collected for correction of susceptibility induced image artefacts in the post-processing (172). In summary, both protocols were designed to provide high-quality dMRI data given the available MR-hardware and within a scan time of $\leq$ 10 min.

Acquisition parameters	Motor system Study I & II	Visual system Study III & IV
MR-scanner	1.5 Tesla (GE Signa Excite)	3 Tesla (GE 750 Discovery)
Data collection	2007	2012-2013
Receiver coil	8-channel head coil	8-channel head coil
Gradient strength	40 mT/m	50 mT/m
Pulse-sequence	Twice-refocused SS-EPI	Twice-refocused SS-EPI
TR/TE	10,000 / 76 ms	6000–7800 / 91.6 ms
Acquired voxel size	2.3 mm^3	2.3 mm^3
Coverage	64 slices (full brain)	~ 50 slices (superior fossa)
Directions and b-values	6 b=0, 45 b=1000 s/mm^2	2 b=0, 60 b=2200 s/mm^2 2 b=0 reversed PE-polarity
Parallel imaging	-	In-plane (ASSET), R=2
Total scan time	8:30 min	8:11 min (for TR=7800) 1:03 min (reversed PE-polarity∗)

Table 3-2 Diffusion-weighted MRI sequence parameters used in Study I & II and Study III & IV. SS-EPI=single-shot echo planar imaging, TR=repetition time, TE=echo time, PE=phase encoding, R=reduction factor. * Reversed PE-polarity scan was acquired as 2b=0 followed by 6 b=200 s/mm^2 in the index group and 6b=1000 s/mm^2 in the control group, however, only the 2b=0 images were used in the analysis.

3.3.4.4 Quality control of dMRI data

In Study I & II, prior to any post-processing, the first b=0 image in the DWI data was discarded due the presence of a higher baseline signal. Presumably from differences in T1-relaxation due to inadequate pre-saturation. This left 5 b=0 images. This was followed by a quality assessment of the DWI data for artifacts. The motivation was rare, scanner-related signal dropouts in some images, but also to exclude data sets corrupted by extensive head motion and/or pulsatile artifacts. Cardiac gating was not used. The procedure resulted in the exclusion of two individuals in the CP group (one with malformation of cortical development and one with WMDI).

In Study III & IV, the problem with differences in the signal levels among the b=0 images, seen in Study I & II, was not present for the dMRI data, presumably due to improved effect from pre-saturating dummy scans in the vendor's dMRI sequence. All images in the dMRI data sets were visually screened to rule out major image artifacts. As expected, some slices contained signal-dropouts artifacts due to head motion and pulsatile movements. No data sets were excluded.

3.3.4.5 Pre-processing and fitting of diffusion models

The pre-processing step consisted of image distortion-correction and realignment, and was performed for both Study I & II and Study III & IV in FSL (194). In Study I & II this was

done with eddy_correct tool (FSL version 4.1). In Study III & IV this was done with the eddy tool (173), that used the additional two b=0 images (with reversed phase-encoding polarity) to estimate susceptibility induced off-resonance field, which is used to improve the image distortion-correction. Realignment was done in both cases to the first b=0 image.

In Study I, the BedpostX tool (default parameters) (191) and the dtifit in the FDT toolbox in FSL (version 4.1; (194)) were used to estimate intravoxel fibre orientation distributions (FOD) and the diffusion tensor respectively. Parametric maps of fractional anisotropy (FA), mean diffusivity (MD) and axial diffusivity ($D_{//}$), and radial diffusivity ($D_{\perp}$) were calculated from the diffusion tensor.

In Study II and III & IV, the intravoxel fibre orientation distributions (FOD) were estimated with constrained spherical deconvolution (CSD) (default parameters; lmax=8) (198) and diffusion tensors with a log-linear fit (174). From the diffusion tensor parametric maps of FA, MD, $D_{//}$ and $D_{\perp}$ were calculated.

In Study II, the quality of the CSD-fit was satisfactory, but affected by partial volume effects in voxels in the proximity of CSF spaces, probably due to the relatively low signal suppression of CSF at b-value=1000 s/mm^2. Therefore a WM-mask was generated in MRtrix (MRtrix2; gen_WM_mask command) and multiplied with the FOD-field. No such problems were present in Study III & IV, probably due to better CSF-signal suppression at the higher b-value used.

3.3.4.6 Fibre tractography of the cortico-fugal fibres (Study I)

The aim of Study I was to track the central cortico-fugal fibres. Fibre tractography was performed using the with ProbTrackX (default parameters) tool in FSL (version 4.1; (194)).

Two sets of region-of-interests (ROI) were defined on the FA-maps. One ROI covering the cerebral peduncle (CerPed; ROI1) and one covering the posterior limb of the internal capsule (PLIC; ROI2). The ROIs were not always symmetrical nor equal in size, but had good anatomical coverage of the structures. The ROI-definition was done by two raters, and showed high reliability (interclass correlation coefficient 0.89-0.96 for inter-rater reliability and 0.88-0.98 for intra-rater reliability; (243)). For each side, two fibre tracts with 5,000 streamlines were generated by seeding in the CerPed (ROI1) and PLIC (ROI2) respectively, and using the other ROI as a waypoint mask. Termination ROIs were defined as voxels inferior and superior to the ROIs. This generated two tracts that were then thresholded to retain 1 % of the total number of generated fibres, and finally, the intersection of the thresholded tracts was extracted as the desired cortico-fugal fibres between the ROIs, here referred to as the "partial tract". ROIs and the partial tracts were used to calculate the mean values of MD, FA, $D_{//}$ and $D_{\perp}$, which were used for statistical comparisons.

3.3.4.7 *Fibre tractography of the cortico-spinal tract and thalamic projection to somatosensory cortex (Study II)*

The aim of Study II was to perform realistic fibre tractography of the motor and sensory tracts. Fibre tractography was performed using the MRtrix package (MRtrix2; (201)).

For an objective ROI definition, a study-based template was created using symmetric normalisation (SyN) (244) of a set of FA-maps. SyN uses a high-resolution diffeomorphic image registration that can capture large brain deformations, common in this patient population. A subset of six controls and seven patients (excluding patients with too large ventricular dilatation and severe pathology) was chosen for constructing the FA-template within the Advanced Normalization Tools Software (ANTs) package (http://www.picsl.upenn.edu/ANTS). Using these transformations, b=0- and colour-coded FA-templates were created as the average of the corresponding images mapped into template space. Each of the subjects' FA-maps were thereafter registered to this FA-template de-novo, creating transformations from native space into template space for all subjects. A set of ROIs were then defined on the FA-template (Figure 3-9).

All ROIs in template space were then mapped into the corresponding native spaces using the inverse transformations. The mapped, non-binary ROIs were thresholded (empirically defined threshold of 0.2) and, in some cases, manually adjusted according to the rules of ROI-definition in template space (Figure 3-9) to assure adequate anatomical coverage.

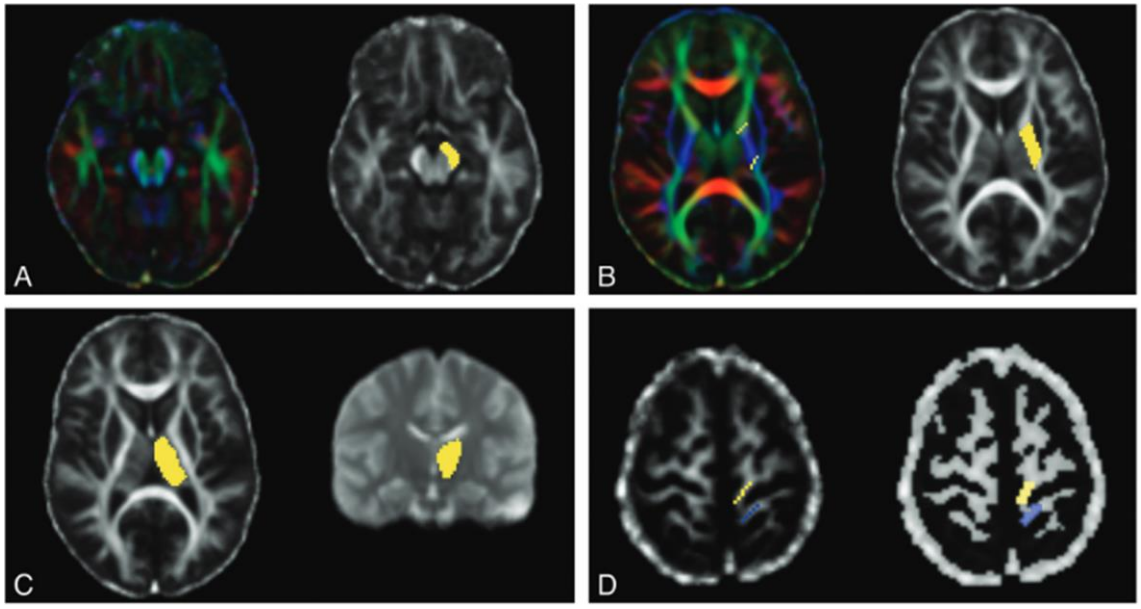

Figure 3-9: ROI definition in Study II. (A) ROIs of the cerebral peduncles (CerPed) and (B) PLIC were defined in the study template using the same rules as in Study I. (C) ROIs of the thalami were defined with lateral borders given by the FA template and medial/ventricular borders from the b=0 template. (D) ROIs of the M1- and the S1-areas were defined by drawing guiding voxels on the FA template over several slices in the pre- and postcentral gyri, laterally past the "hand knob", and defining the extent of the ROI by including surrounding voxels the FA template thresholded at FA ≥ 0.2. R=right, L=left, CerPed=cerebral peduncle, PLIC=posterior limb of internal capsule.

Probabilistic fibre tractography of the cortico-spinal tract (CST) and the thalamic projections to primary somatosensory cortex (TRS1) was performed in MRtrix (default parameters). For

the CST, streamlines were seeded in the M1-ROI using the ipsilateral PLIC- and CerPed-ROI as waypoint masks. The TRS1 was generated by seeding in the thalamus-ROI and using the ipsilateral S1-ROI as a waypoint mask. All fibre tracts were generated until 10,000 accepted streamlines had been achieved. Tracts that could not produce this number of streamlines within a factor of 10^4 more trials (i.e. 10^8 trials) were considered to have too low a probability of connectivity, and were excluded from further analysis. Fibre tracts were then converted to probability maps, which were thresholded at 0.01 (i.e. including voxels through which 1 % of the generated streamlines passed) to represent the "core" of the tracts. The CerPed- and PLIC-ROIs were used to divide the CST into three portions: between M1 and CerPed (CST-M1 to CerPed), between PLIC and CerPed (CST-PLIC to CerPed), and between M1 and PLIC (CST-M1 to PLIC, not including PLIC-level voxels). This allowed the different parts of the CST to be analysed separately. Similarly, the thalamic-ROIs were used to exclude thalamic voxels from the TRS1 tracts. Visual inspection of the fibre tracts revealed four distinct patterns deviating from what was normally expected: tracts that were split, dislocated, compacted or non-trackable. This qualitative fibre-tract assessment (FTA) was done by identifying a deviating pattern along the fibre tracts and confirming it on the thresholded probability map. Finally, the median values of MD, FA, $D_{//}$ and $D_{\perp}$ were extracted for all of the relevant parts of the CST and TRS1 tracts, as described above.

3.3.4.8 Fibre tractography of the optic radiation (Study III & IV)

The aim of Study III & IV was to perform realistic fibre tractography of the optic radiation (OR). Fibre tractography was performed using the MRtrix package (201).

Both studies used a 4-mm radius sphere, encapsulating the lateral geniculate nuclei (LGN) (245), as a seed ROI. The location of the LGN-sphere was determined by following tensor streamlines generated in the optic tracts when they reached the thalamus, by visual inspection of this area on b=0- and fractional anisotropy (FA)-maps, as well as from the coherence in the FOD-field. To prevent streamlines from erroneously crossing the midline, exclusion ROIs of the corpus callosum and the anterior commissure were defined. Even so, in some instances, streamlines managed to reach the occipital lobe by traversing the CSF space in the quadrageminal cistern. This was prevented by defining a local exclusion ROI medio-posteriorly to the LGN-sphere, which blocked such erroneous streamlines.

Study III used a 30-mm radius sphere centred in the same side's occipital pole and covering the calcarine sulcus as an ipsilateral waypoint mask (201). In Study IV, cortical activation maps of the dorsal V1-area (V1d-ROI) and the ventral V1-area (V1v-ROI) were used as ipsilateral termination masks. With the defined seeding, inclusion and exclusion ROIs probabilistic fibre-tracking was performed with MRtrix (default parameters). In Study III, the reconstructed ORs also included extrastriate projections. In Study IV, only striate projections in the OR were generated, specifically the projections to the dorsal and ventral V1 areas (defined by the V1d- and V1v-ROIs respectively). These tracts are referred to as the OR-V1d and OR-V1v tracts. OR-V1 tracts were created by combining the OR-V1d and OR-V1v tracts on each side.

In Study III, the tracking algorithm was run until 10,000 streamlines had been generated, whereas in Study IV, 5,000 streamlines were generated for each of the OR-V1d and OR-V1v tracts.

To exclude connections of low probability, streamlines that entered voxels with a visitation count of less than 0.1 % of the total number of generated streamlines were rejected (i.e. 10 and 5 for tracts with 10,000 and 5,000 streamlines respectively). In Study III, this resulted in a rejection of 15-25 % of the total number of streamlines for the patients. In Study IV, the rejection rate was in the range 5-11 % for both controls and patients. The set of remaining streamlines was considered to be of the desired tract. The discrepancy in the rejection rates between Study III and Study IV was expected, as the occipital sphere in Study III was a much larger waypoint mask than the cortical V1d- and V1v-ROIs in Study IV.

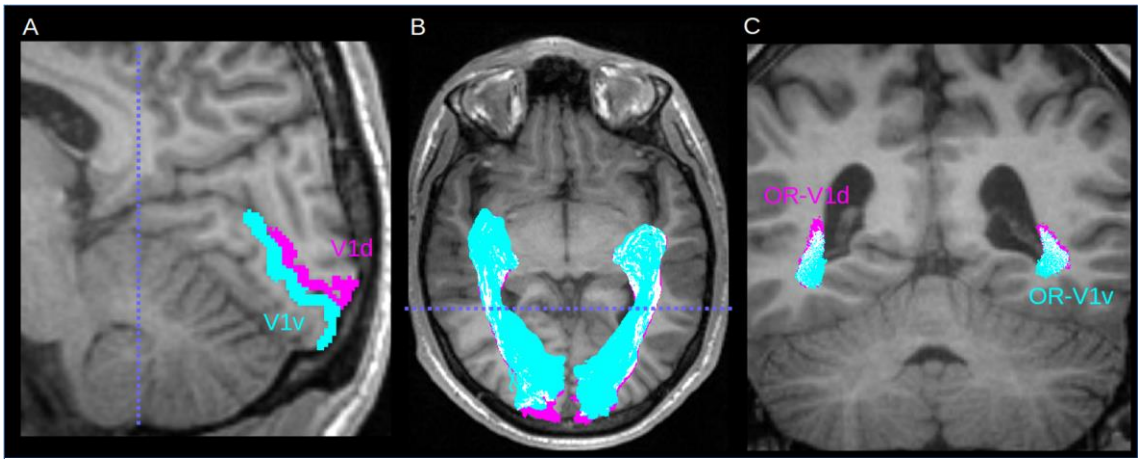

Figure 3-10: Fibre tractography of the ORs. (A) The left side's V1d- (pink) and V1v-ROI (turquoise) mapped onto a T1w-image in sagital mid-line section around the calcarine sulcus. (B) Fibre tracts for OR-V1d (pink) and OR-V1v (turquoise) overlaid on T1w-image in (B) an axial and (C) a coronal section at the level of the trigone (dotted blue line in A and B). Images displayed in radiological convention.

To assess the tracts' relations to anatomical structures, the T1w- and dMRI images were co-registered using FLIRT (241) in FSL. The thresholded OR tracts in Study III and the OR-V1, OR-V1d and OR-V1v tracts in Study IV were visually assessed and compared to their expected extent and topographical configuration (26,246), and to the lesions seen on conventional MRI.

In Study IV, the mean values of FA, mean diffusivity (MD), axial ($D_{//}$) and radial diffusivity ($D_{\perp}$) were calculated along each streamline in the OR-tracts, then averaged for each tract and used for statistical comparison. The spatial overlap between the OR-V1d and OR-V1v tracts was evaluated using Cohen's kappa-coefficient (208,247) of the corresponding probability maps (binarized). Finally, the apparent fibre density (AFD) (225) connectivity (afdconnectivity command in MRtrix3; https://github.com/MRtrix3/mrtrix3) was calculated for all OR-tracts. This is based on the fact that the integral over an FOD lobe is proportional to the volume of the underlying MR tissue signal (225). By adding the integrals of the FODs traversed by all streamlines, a total tract volume is obtained, which is then divided with the average streamline length giving an average area of the tract. The average area corresponds to a

measure of the connectivity of the tract which is independent of the tract length. The AFD connectivity measure for each OR tract was used for statistical comparison.

3.3.4.9 Acquisition and analysis of retinotopic fMRI mapping (Study IV)

Retinotopic fMRI mapping was done with a gradient-echo EPI-sequence (TR/TE=1600/34 ms; FA=65°; resolution 3 mm^3; 30 axial slices, interleaved acquisition; ASSET=2 in-plane). Slices were placed to ensure coverage of the occipital lobe. A total number of 144 imaged volumes were collected to match the retinotopic stimulus for a total scan time of 4:06 min.

Stimulation of the visual field was performed using rotating wedges and expanding/contracting rings (235), as described in 3.3.3. The stimulus was presented to the subject's dominant eye (the non-dominant eye was covered with an eyepatch) in the MR-scanner, using an MR-compatible visual system (NordicNeuroLab, Norway). The system allowed stimulation of the visual field of maximum 30^o horizontally and 23^o vertically. The maximum eccentricity used in the visual stimulus was 11^o. One stimulus cycle was set to 16*TR. The complete fMRI-stimulus contained two blocks with three cycles of complete revolutions, interspersed within three blocks of non-active stimulus (grey screens), lasting one cycle each. The first non-active block was preceded by 10 "dummy scans". The total duration for each fMRI stimulus amounted to 4:06 min.

The rationale for including non-active blocks was to provide a baseline for estimation of population receptive fields. In this study, the fMRI volumes for these time points were excised from the time series, and only the active stimulus data was used for the analysis in Study IV.

Analysis of the retinotopic fMRI data was performed using standard procedures (235), and is described in 3.3.3. A sinusoidal function with 6 cycles was fitted to the averaged time-series for the wedge and ring stimuli. The polar angle and eccentricity would then correspond to the phase of the fitted response function for the wedge and the ring stimuli respectively. The V1-area was defined on the phase map of the polar angle stimulus on the cortical flattened maps. Its ventral (V1v) and dorsal subparts (V1d) were defined as the separation corresponding to the middle of V1 (corresponding to the horizontal meridian) (Figure 3-8B, p. 62). Subsequently, the V1-, V1d- and V1v-ROIs were then mapped into diffusion space, to be used as cortical targets for fibre tractography (Figure 3-10, p. 68).

3.4 CLINICAL TESTING

3.4.1 Motor system (Study I & II)

The children with unilateral CP in Study I & II were assessed for gross motor function with Gross Motor Function Classification System (GMFCS) (110). All participants had GMFCS level I, which means they can walk outdoors and indoors and climb stairs without problems. The Manual Ability Classification System (MACS) (79) was used to describe how they used their hands to handle objects in daily life. The children were found to have MACS levels I-II.

At MACS level I, objects are handled easily and successfully, whereas for level II, most objects are handled, but with some loss of accuracy and/or speed.

To measure gross manual dexterity, the timed Box and Blocks test (B&B) (80) was used for each hand. In the B&B-test the participant is asked to move blocks from one box to another, which are divided by a 20 cm high separator. The test score is the total number of blocks moved in 60 seconds.

3.4.2 Visual system (Study III & IV)

In all participants, their best corrected visual acuity was tested monocularly, in a standardized way, using LogMar charts. Binocular evaluation was done with a cover test. Colour fundus photographs were obtained for documentation and illustration.

For quantitative measurement of the central (30°) visual field (VF), standard automated perimetry was performed using a computerized Humphrey Field analyzer (HFA; Carl Zeiss Meditec, Dublin, CA, USA) with the SITA Fast 24-2 test. The visual field sensitivity was quantified using the mean deviation, i.e. the average of differences from the normal expected value for that age. The mean deviation gives an overall value of the total amount of visual field loss, and is given in decibel (dB).

In the patient group, standardized kinetic Goldmann perimetry was performed (248). The extent of the VF was determined by using V/4e or II/4 stimulus. For the central VF, one or more of the stimuli, I/3e, I/2e, or I/1e, were used. In cases where these stimuli were not detected, I/2d was used for the central 10°.

In all participants in Study III & IV, an examination of the retinal nerve fibre layer (RNFL) and the macular ganglion cell complex (GCL_IPL; including the ganglion cell layer and the inner plexiform layers) was performed using a standardized laser measurement technique with Spectral domain OCT from the Carl Zeiss model HD-Cirrus OCT™ 5000 (Carl Zeiss Meditec, Dublin, CA, USA). The Optic Disc Cube protocol was used for classifications of the RNFL surrounding the optic nerve head. Quantitative measures of the mean RNFL thickness and the mean values in each quadrant around the optic disc is given in µm by the machine. Similarly, for the GCL_IPL, the Ganglion Cell Analysis protocol was used .

3.5 STATISTICAL ANALYSIS

3.5.1 Statistical methods

Statistical analyses were performed in SPSS 17® (SPSS Inc, Chicago, IL, USA) in Study I, and in Statistics Toolbox in Matlab (MathWorks, Natick, MA, USA) in Study II-IV.

All statistical inference used two-tailed test and P-value < 0.05 as significance level.

3.5.1.1 Study I & II

Statistical comparisons of DTI parameters between groups in Study I & II were done using the non-parametric Wilcoxon rank test. Side differences were explored using the Sign Test. Associations between FA and the B&B-test score in Study I were explored, with partial correlations controlling for age. Exploratory regression analysis was performed with the dependent variable "B&B-test score" and the independent variables FA, lesion type, and severity of periventricular white matter reduction.

To assess intra-and inter-rater reliability of ROI-definition in Study I, the interclass correlation coefficient (243) was used. In Study II, the intra- and inter-rater reliability was assessed by pair-wise comparisons of the spatial matching (208) between the thresholded probability maps of the fibre tracts by calculating Cohen's kappa-coefficient (247) .

3.5.1.2 Study III & IV

In Study III, the non-parametric correlation coefficient (Spearman's rho) was used to infer associations between the visual field loss (mean deviation of HFA given in dB) and the average RNFL thickness.

In Study IV, the non-parametric Wilcoxon rank test was used to infer within- and between group differences for tract parameters in the OR tracts, the spatial overlap between OR-V1d and OR-V1v tracts, and the OCT measurements of GCL_IPL thickness in the eyes. Associations between the mean values of the left and right tract parameters and the mean of the left and right eye's average GCL_IPL thickness were estimated with the non-parametric correlation coefficient (Spearman's rho). A more realistic model explored associations between the GCL_IPL thickness for each eye and the tract parameters in the ipsi- and contralateral OR tracts using a linear regression model.

4 RESULTS

4.1 MOTOR SYSTEM

The overall aim of Study I & II was to investigate the microstructure in motor and sensory tracts with diffusion-weighted MRI (dMRI) and fibre tractography in unilateral CP, and to relate this to lesion assessment on conventional MRI and measures of hand function.

4.1.1 Study I

The specific aim of this study was to investigate the microstructure in central parts of corticofugal fibres in unilateral CP (at the level of the posterior limb of the internal capsule (PLIC; ROI2), the cerebral peduncle (CerPed; ROI1) and the portion of fibres (partial tract) connecting these areas, and their correlations with hand motor function.

Diffusion measures on the non-dominant side in the CP group showed a significant decrease in FA in both ROI1 and ROI2, as well as in the partial tract, compared to the controls. This was driven by a significant increase in the radial diffusivity ($D_{\perp}$). On the lower level, in

ROI1, there was a concomitant significant decrease axial diffusivity ($D_{//}$), which is interpreted as changes congruent with secondary anterograde (Wallerian) degeneration (181). On the upper level, in ROI2, there was a significant increase in MD which, in combination with changes in FA and $D_{\perp}$, indicates altered tract microstructure. The particular combination of changes to these DTI parameters in ROI2 does not indicate a specific neurodegenerative pattern. Subgroup analysis showed a significant side-difference for individuals with unilateral lesions on conventional MRI (n=10) in FA in ROI1, and MD in ROI2, but no significant side-differences in the individuals with bilateral lesions (n=5).

There was a positive correlation between FA and the performance on the B&B-test both in the partial tract ($r = 0.570$, $p = 0.042$) and the ROI1 ($r = 0.602$, $p = 0.027$) on the non-dominant side (Figure 4-1). This remained significant after controlling for the voxel number, as a measure of tract size. No correlations were seen for ROI1, nor for the dominant side. An exploratory regression analysis showed that FA was a significant contributor to the B&B performance, whereas neither the lesion type nor the lesion extent were.

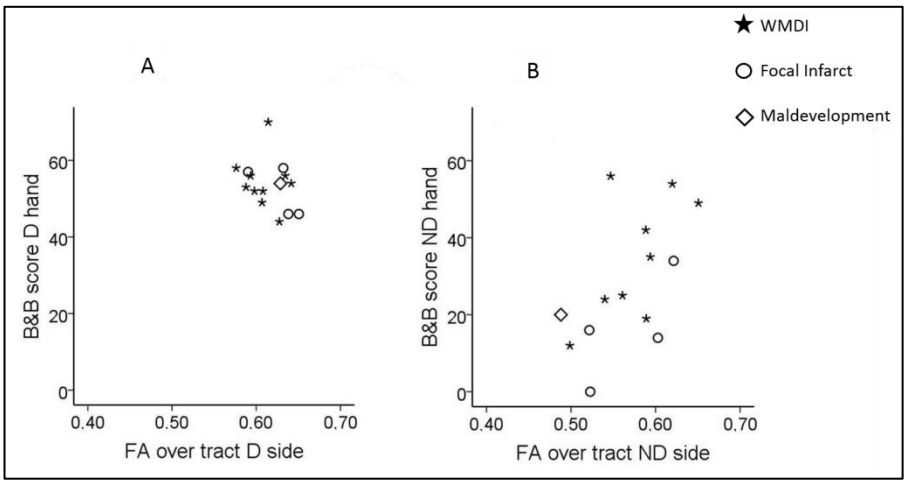

Figure 4-1: Relationships between functional outcome and FA. Performance on the B&B test (the higher the score, i.e. the more blocks moved within 60 seconds, the better the performance). FA=fractional anisotropy, D hand = dominant hand, ND hand = non-dominant hand, and association with FA, D side=tract contralateral to dominant hand, ND side = tract contralateral to non-dominant hand; n=15 children with CP.

In summary, Study I showed that FA is a sensitive marker for damage to the motor system and correlates with hand function in unilateral CP. Analysis of diffusion parameters reveal altered microstructure in affected cortico-fugal fibres, which, distant from the lesions, are congruent with secondary neurodegeneration.

4.1.2 Study II

The aim of this study was to further investigate the changes to the cortico-fugal fibres seen in Study I, using a combined normalization and probabilistic fibre-tracking methods for improved fibre tractography. With this method, the cortico-spinal tract (CST) could be investigated both close to and distant from the lesion, and compared to the adjacent thalamo-cortical connection to the primary sensory cortex (TRS1). This method thus enabled a selection of the CST from the cortico-fugal fibres analysed in Study I.

The method used showed high intra- and inter-rater reproducibility, and could realistically reconstruct the CST and TRS1 in the controls and the CP group. Qualitative fibre-tract assessment (FTA) of the gross morphology of the CST and TRS1 showed alterations in the tract paths on the lesion-side in the individuals with unilateral CP. The patterns of atypical FTA ranged from advanced morphological alterations, to an inability to track the tract, and could be explained by an interaction of the tract with the lesion (Figure 4-2).

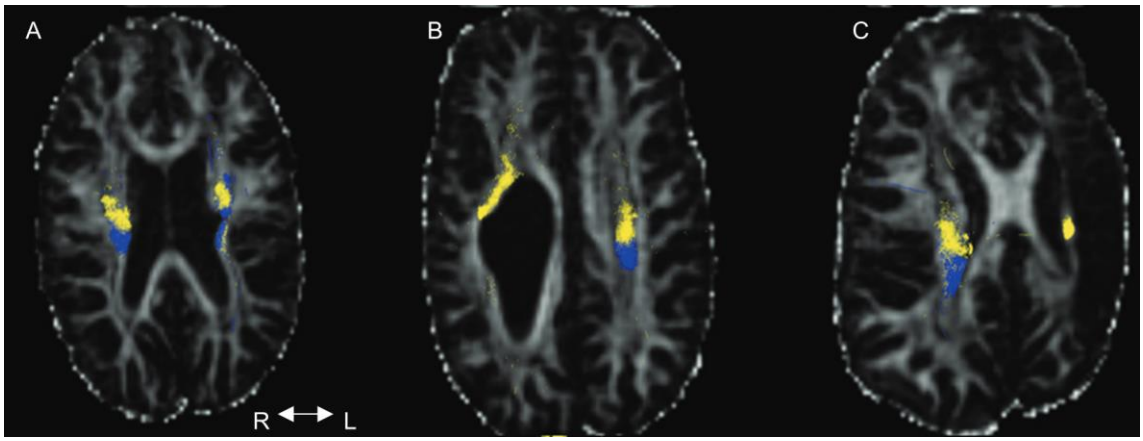

Figure 4-2: Fibre tract assessment of the CSTs (yellow) and the TRS1s (blue) in three individuals with unilateral CP (Subject 9, 12 & 14). Tracts are superimposed on FA maps in the axial section at the level of corona radiata. (A) Subject 9 has WMDI and a periventricular pseudocyst at the level of corona radiata, which causes local splits to the left TRS1 and left CST, and a dislocation of the major branch of the left CST. (B) Subject 12 has WMDI. The large right WM lesion made tracking of the right TRS1 impossible and caused a dislocation of the right CST. (C) Subject 14 had a focal infarct resulting in extensive damage to the entire left hemicranium. The left CST was confined within a thin sliver of WM at the level of the corona radiata. The left TRS1 was non-trackable. CST=cortico-spinal tract, TRS1=thalamic projections to primary sensory cortex, WMDI=white matter damage of immaturity.

Analysis of DTI parameters showed signs of primary neurodegeneration in lesion-affected areas and distant secondary (Wallerian) neurodegeneration in the CST in the CP group (181), whereas TRS1 showed a significant increase in MD only, which does not indicate any specific neurodegenerative pattern. On the non-lesion side, TRS1 and comparable parts of CST showed similar significant, modest increases in MD, which may indicate the presence of bilateral affection or secondary changes caused by the contralateral lesion. The results are summarized in Table 4-1.

Tract	Lesion side	Non-lesion side
CST (distant from lesion)	MD - , FA ↓↓ , $D_{//}$ ↓↓, $D_{\perp}$ ↑↑ Secondary neurodegeneration*	MD - , FA - , $D_{//}$ - , $D_{\perp}$ - No changes
CST (close to lesion)	MD ↑↑ , FA ↓↓ Primary neurodegeneration*	MD ↑ , FA - Neurodegeneration*?
TRS1 (close to lesion)	MD ↑↑ , FA - Reactive changes??	MD ↑ , FA - Neurodegeneration*?

Table 4-1 Study II showed significant changes in DTI parameters in patients compared to controls in the CST and the TRS1 on both the lesion and non-lesion sides. CST=cortico-spinal tract, TRS1=thalamic projections to primary sensory cortex, MD=mean diffusivity, FA=fractional anisotropy, $D_{//}$ = axial diffusivity, $D_{\perp}$ =radial diffusivity. * Interpretation based on Pierpaoli et al (181).

In summary, the fibre-tracking method explored in Study II offers a sensitive means to study WM tracts in early brain lesions in areas of complex white matter architecture. There are dissimilarities in both the structural and the parametric changes seen in CST compared to TRS1 on the lesion-side, which indicate that the tracts are affected differently by the injury. Whether this could also be due to secondary reactive changes in TRS1 cannot by inferred with the limited information given by the tensor model.

4.2 VISUAL SYSTEM

The overall aim of Study III & IV was to seek evidence for relationships between injuries to the immature optic radiation, the cortical visual field representation, and the development of the retinal nerve fibre layer and macular ganglion cell complex, and to correlate this with visual field function.

4.2.1 Study III

The specific aim of this study was seek evidence of a relationship between damage to the immature optic radiation (OR) and subsequent development of the retinal nerve fibre layer (RNFL), and the associated visual field (VF) function.

Visual inspection of conventional MRI showed WMDI affecting the posterior periventricular WM to different degrees in all seven cases. In four cases with VF defects, fibre tractography showed a marked reduction in the superior extent of the OR, and OCT measurement showed commensurate reduction of the RFNL thickness in the temporal and perimacular bundle. All four cases had corresponding injuries to the visual pathways on conventional MRI. One case showed a slight reduction of the number of fibres/fibre density in the central part of the right OR, and OCT showed a slightly reduced RFNL on the left side consistent with close-to-normal central VF on the right and slightly abnormal central VF on the left. Whereas two cases showed normally appearing OR on fibre tractography and normal RFNL thickness, corresponding with their normal VF function, despite suspected injury to the OR on conventional MRI. There was a linear correlation between the average thickness of the RFNL and the VF defect (mean deviation of HFA), illustrated in Figure 4-3.

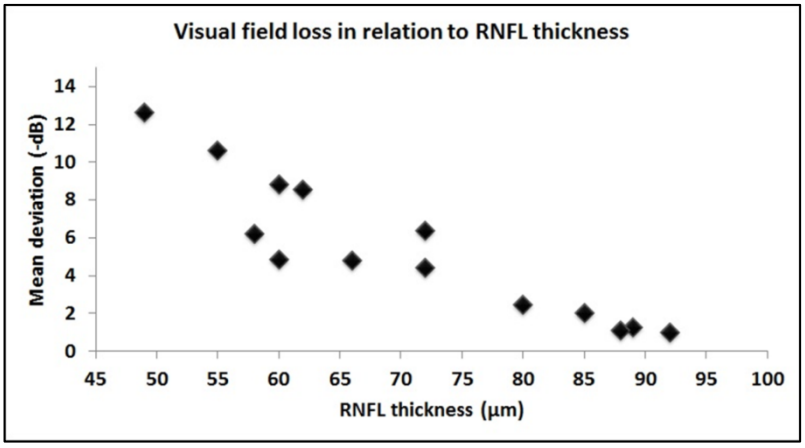

Figure 4-3: Visual field loss, given as mean deviation plotted relative to the average RNFL thickness, showed a significant negative correlation (r=0.92, p<0.0001). RNFL=retinal nerve fibre layer.

In summary, Study III supports the fact that fibre tractography is more sensitive than conventional MRI in assessing injuries in the immature OR. Injuries to the immature OR are associated with reduced RFNL thickness and show corresponding VF defects. Cases of primary injuries to posterior visual pathways show congruent retinal injuries, which suggests retrograde trans-synaptic degeneration. OCT and measurement of the RFNL thickness could be a valuable tool for predicting VF defects, especially in a paediatric population.

4.2.2 Study IV

The specific aim of Study IV was to refine the fibre tractography of the OR by including cortical targets of the V1-area from retinotopic fMRI mapping. The retinotopic organisation of the OR could thereby be studied and compared with OCT measurements of the macular ganglion cell complex (GCL_IPL; including the ganglion cell layer and the inner plexiform layers), which has a more direct correspondence to visual field. This study could provide evidence for retrograde trans-synaptic degeneration (RTSD) in the visual system.

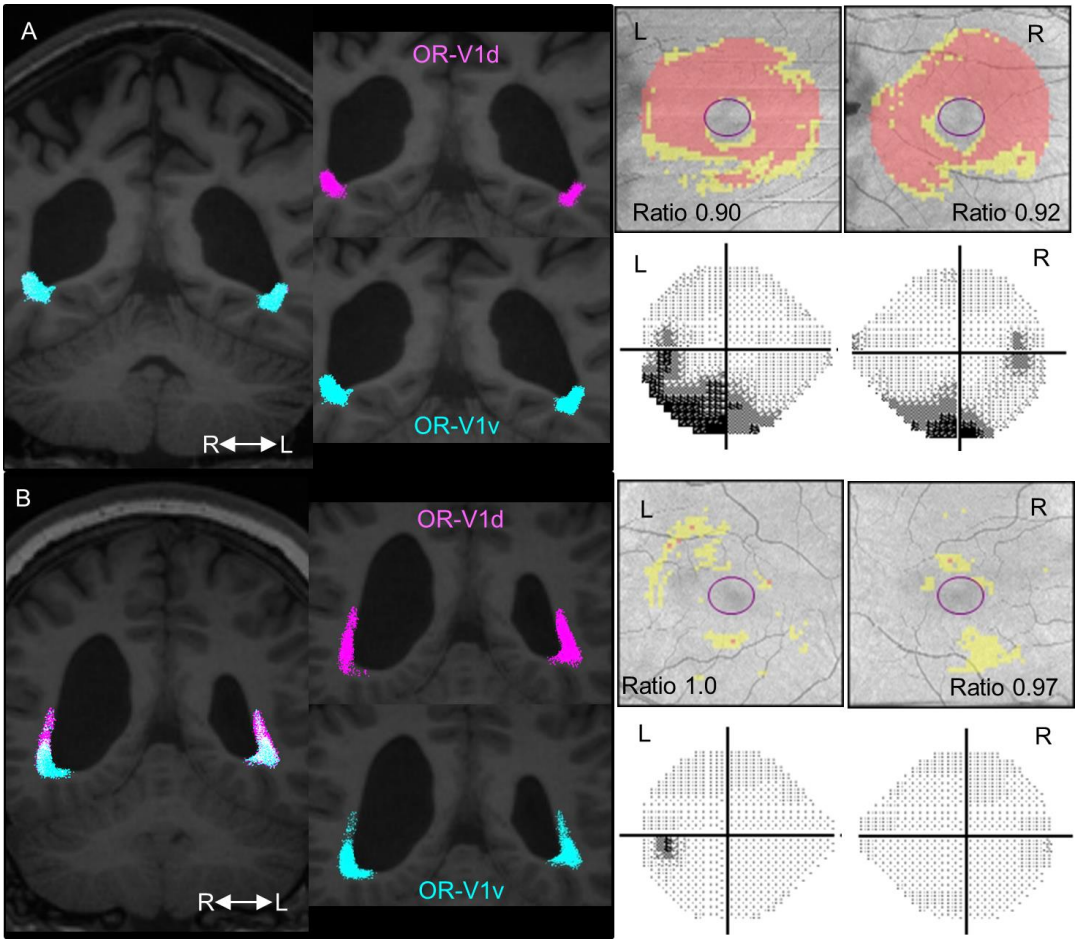

Figure 4-4: Spatial distribution of streamlines in the OR-V1d (pink) and OR-V1v (turquoise) tracts in (A) Subject C and in (B) subject G, and their corresponding GCL_IPL measurements and visual field maps. Left column: Tracts overlaid on 3D-T1w images in a coronal section at the level of the trigone. Right column: Maps of the macular GCL_IPL thickness topography, with yellow indicating minor thinning and red more severe thinning. Ratio of the average GCL_IPL thickness in superior and inferior sectors are inserted. VF maps assessed with Humphrey Field analyser. The grayscale running from white to black with more intense darkness, illustrating deeper sensitivity reduction. Grayscale printouts illustrating the reduced sensitivity in the inferior hemifield, typical for this study group. R=right, L=left.

The OR tracts could be reliably reconstructed for all participants. They showed a substantial overlap between the OR-V1d and OR-V1v tracts, pronounced in four patients with bilateral, homonymous inferior visual field (VF) defects, in which the OR-V1d tract to a large extent was encapsulated within the OR-V1v, suggesting structural morphological changes.

Diffusion parameters were significantly different (increase in MD, $D_{//}$ and $D_{\perp}$, and decreased FA) between patients and controls, most pronounced in OR-V1d, with a pattern indicating general loss of structural coherence as in primary injury (181). The GCL_IPL thickness was significantly thinner in the patients than in the controls, and most pronounced in the superior sectors, with a clear distinction for the four patients with VF defects. A significant linear correlation was seen between the ratio of the mean GCL_IPL thickness in the superior and inferior sectors, and the $D_{//}$ and MD in the contra- and ipsilateral OR-V1d tracts in the patients. This suggests a causal link between injuries to the superior portion of the immature OR and secondary thinning of the GCL_IPL thickness, resulting in inferior VF-defects.

The MD and $D_{//}$ in OR-V1d tracts and the GCL_IPL thicknesses are illustrated in Figure 4-5.

With the suggestive evidence for RTSD in four individuals, the spatial dislocation of the OR-V1d tract (i.e. the most probable connection to dorsal V1) to within the OR-V1v, must suggest that we see compensatory changes to the OR in WMDI, however, we cannot say whether this is strengthening already existing connections or a recruitment of new fibres. Both are possible, as WMDI occur during the time frame of the developing connectivity (2).

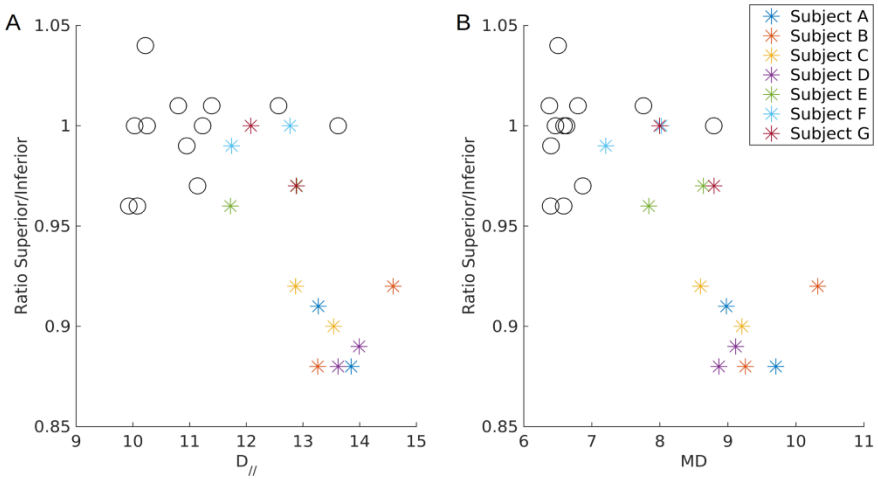

Figure 4-5: The ratio of the average GCL_IPL thickness in superior and inferior sectors in each eye plotted against (A) $D_{//}$ and (B) MD in the ipsilateral OR-V1d tract. Data points are colour-coded for each patient. Diffusivity in unit 10^{-4} mm/s^2. $D_{//}$ = axial diffusivity , MD = mean diffusivity.

In summary, Study IV showed a topographical relationship between injury in the superior portion of the OR, which was evaluated in the OR-V1d tract, and thinning of the GCL_ILP above the horizontal meridian. The correspondence is compelling, and compliant with the extent of VF-defects. This study gives strong evidence of RTSD in the immature visual system. The structural changes to the OR-V1d tract in the cases of RTSD may suggest a compensatory re-organisation in the OR upon injury.

5 DISCUSSION

5.1 METHODOLOGICAL CONSIDERATIONS

5.1.1 Diffusion-weighted magnetic resonance imaging

Diffusion-weighted MRI (dMRI) with fibre tractography is the main method of investigation used in this thesis. At the time of designing the studies, it was decided that the dMRI acquisition protocols (Table 3-2, p. 64) and the choice of fibre tractography methods were optimal for Study I and Study III & IV.

Study II was an extension of Study I, and used probabilistic CSD-fibre tracking. CSD was not considered at the time of the design of the dMRI protocol in Study I. In retrospect, Study II would have benefitted from an dMRI acquisition optimized for CSD (200), primarily by using more directions (at least 60) at a higher b-value (2000-3000 s/mm^2). This would have improved the angular resolution in the FOD-profiles, and minimized partial volume effects from CSF, which might have helped us to understand the small splits to tract paths seen in non-lesion affected areas. In addition, the differences in FA-changes seen between the CST and the TRS1 on the lesion-side, and the minor MD increases seen in both tracts on the non-lesion side, might have been better understood.

Study IV could have opted for the SIFT-method (spherical-deconvolution informed filtering of tractograms) (249) as a better alternative to the AFD connectivity. The spatial overlap between the OR-V1d and OR-V1v tracts means that the tracts share FODs in many voxels. The AFD connectivity method cannot differentiate between streamline populations that share FODs, whereas SIFT can. Differences between the OR-V1d and OR-V1v could therefore have been investigated in more detail with SIFT. However, the implementation of SIFT in Study IV would have required extensive further analysis, which would have included generating dense, computationally intensive whole-brain tractograms, and improving the GM/WM segmentation in the datasets of the individuals with WMDI.

5.1.2 Accuracy and reliability of the ROI-definition and the fibre tractography methods

The manual definition of the ROIs in Study I, and the fibre tracking method in Study II, showed high intra- and inter-rater reliability for all the controls and patients.

No reproducibility studies were performed for the fibre tracking method used in Study III & IV. The use of a spherical ROI, with 4-mm radius to define the lateral geniculate nuclei (LGN), was adapted from another study (245). The LGN can vary in size in humans (250), but the 4-mm radius ensures that the entire LGN is encapsulated within the spherical ROI (245). Alternative approaches could have been to use fMRI or anatomical sequences to delineate the LGN (251,252). The occipital spherical ROI with 30-mm radius used in Study III was a pragmatic approach adapted from another study (201), and gave reliable reconstructions of the optic radiations (OR). The retinotopic fMRI mapping used in Study IV gave anatomical accuracy to the OR-V1 tracts, which, however, only showed minor differences in

their periventricular courses compared to the OR tracts in Study III. This mapping method provided a topographical representation along the OR of the division between the lower (inferior) and upper (superior) visual fields. The results showed correspondence with the known retinotopic organization (26,246) and with previous fibre tracking studies (245,253,254).

5.2 STRUCTURAL MORPHOLOGICAL CHANGES TO FIBRE TRACTS

A main finding of this thesis is the observation of advanced morphological changes to the fibre tracts. This was seen both in the studied tracts in the motor system (CST and TRS1 tracts in Study II), and in the visual system (OR tracts in Study III & IV).

In Study II, from visual inspection, we could identify four distinct characteristics in the gross morphology of the CST and TRS1 tracts that deviated from what was expected as the tracts passed in lesion-affected areas. This was summarized as atypical patterns in fibre tract assessment (FTA). Tracts showing atypical FTA were observed on the lesion-side in several cases, and in all lesion types. Similar morphological alterations to the sensory and the motor tracts have been reported before in early brain lesions (145,146), also using probabilistic CSD-fibre tractography (125,147).

In Study III & IV, we saw, similar to Study II, structural alterations to OR tracts caused by the periventricular white matter lesions. In Study III, we studied the entire OR tract and could, by comparison with expected neuroanatomy, see distinct areas in the superior portion of the OR, with substantially fewer streamlines in four individuals. This was described as "reduced number of fibres" in parts of the published article (255). This is not an accurate description (204), and instead "reduced number of streamlines" should have been used consistently (although only visually assessed). The results however, hold true, since a matching thinning of the retinal nerve fibre layer and inferior visual field defects were seen in those four individuals. With the refined methodology used in Study IV, we concluded that the superior portion of the OR, evaluated as the OR-V1d tract, was indeed displaced and confined within the OR-V1v tract. This is suggestive of a re-organisation of the immature OR upon injury (see also the discussion in 5.5). Only case studies have previously shown fibre tractography results of OR by-passing periventricular lesions (92,133), but no studies have investigated this in more detail.

5.3 INFERENCE OF MICROSTRUCTURAL CHANGES FROM DIFFUSION PARAMETERS

This thesis used estimations of DTI parameters to infer microstructural changes to the studied white matter tracts caused by early brain lesions. The ROIs used for extracting diffusion parameters were manually drawn in Study I, and tract-based in Study I,II & IV (see 3.3.2.6 for a discussion on differences). Each study includes a discussion on the validity and limitation of using DTI parameters. The last study, Study IV, also calculated the AFD (225) connectivity (CSD-based parameter), which provides quantitative measures specific to individual fibre tracts in areas of complex fibre architecture.

5.3.1 Changes in diffusion parameters in lesion affected areas

In Study I & II, the changes in DTI parameters in the cortico-fugal fibres at the level of the cerebral peduncle (ROI1) and in the CST distant from lesion site (CST-PLIC to CerPed), were indicative of secondary neurodegeneration (181). This has also been demonstrated in a previous study (120). In Study I, these changes were not significant in the partial tract or in the PLIC (ROI2). However, DTI parameters (specifically axial $D_{//}$ and radial diffusivity $D_{\perp}$) are difficult to interpret in this area (PLIC), because it is, firstly, located closer to the primary lesion and, secondly, it naturally contains voxels dominated by, or intermingled with, fibre tracts other than the descending motor tracts (256). The latter had a larger effect on the broader cortio-fugal tract in Study I than the CST in Study II. In fact, fibre tractography of cortic-fugal fibres in Study II revealed, as expected, that the CST was located within the cortico-fugal fibres (data not shown) in all cases with trackable CSTs.

In Study II, we could study the CST closer to the lesion (CST-M1 to PLIC), and saw changes here indicative of a general loss of coherence, as in primary injury (large decrease in FA and large increase in MD). Several other studies have shown similar changes of increased MD and decreased FA on the lesion side in the CST in unilateral CP (118), and also congruent decrease in AFD connectivity (124). DTI parameters in TRS1 showed a similar increase in MD, but no significant change in FA, though the FA was generally lower. This could not be linked to any specific injury pattern. Two other studies have used a similar probabilistic CSD-tracking method with cortical targets in larger cohorts with WMDI (122,125). Tsao et al (125) reported increased MD and decreased FA in thalamic projections to the post-central gyrus, whereas Pannek et al (122) saw no changes in FA (MD not reported). The interpretation from Study II is that in our study cohort, the CST was more affected by lesions than the TRS1. However, reactive changes in TRS1 is a speculative alternative interpretation. The spatial closeness of the CST and TRS1 tracts (illustrated in Figure 4-2, p. 73) and the cover page of this thesis) makes it important to investigate these findings in more detail, preferably in a more homogenous lesion group, using higher-order diffusion models.

In Study IV, we could see changes in DTI parameters (increased MD, $D_{//}$ and $D_{\perp}$ and decreased FA) bilaterally in all OR-tracts, which were most pronounced in OR-V1d tracts. Our interpretation is that the DTI changes indicate primary destructive injuries, as in WMDI. In contrast to the analysis of CST-M1 to PLIC and TRS1, we could use the axial $D_{//}$ and radial diffusivity $D_{\perp}$ to aid our interpretation. The results in Study IV are in line with previous studies in preterms (134–136,138). The AFD connectivity was also decreased, which is in line with the DTI changes. Interestingly, there was a significant and consistent left-right difference in the AFD connectivity in the seven patients. This is difficult to explain. One reason may be a difference in lesion-load in the seven patients. Another explanation may be related to the large, natural variability seen in the extent of the Meyer's loop (246). Recent tractography studies indicate a lateralization in Meyer's loop associated with language lateralization (257). However, we did not observe any side-differences among our six controls.

5.3.2 Changes on the non-lesion side in unilateral cerebral palsy

In Study I and Study II (CST-PLIC to CerPed), we did not find any differences between DTI parameters on the non-lesion side in the patients and in the controls. This is in line with a previous study on spastic unilateral CP by Glenn et al (258), who studied the CST in these locations in a similar cohort also containing different lesion types. Further, in Study I we found, also in line with Glenn et al, significant differences in the DTI parameters between the two hemispheres in the subgroup of patients with unilateral lesions on visual inspection of conventional MRI. This reached significance at the level of the cerebral peduncle (ROI1) for MD and FA. There were similar side-differences in FA in the patients with bilateral lesions on visual inspection of conventional MRI, but these did not reach significance. The small size of this subgroup (n=5) may have contributed to this. However, overall, this finding may serve to help explain why hand function is more impaired on one side, even though bilateral lesions are seen on visual inspection of conventional MRI.

In Study II, we saw similar, modest increases in MD in the patients compared to the controls - on the non-lesion side in the TRS1, and the comparable part of the CST (CST-M1 to PLIC). This indicates more wide-spread lesion-effects. However, we cannot say whether the MD changes are due to bilateral lesions or secondary changes from the lesion side, e.g. in trans-callosal connections. Recent studies in unilateral CP have shown reduced FA in trans-callosal motor fibres in unilateral CP (121,122). An important further step would be to analyse these changes in more detail in order to understand the pathological changes upon injury. This would require using higher-order diffusion models to study the fibre populations separately.

5.4 CORRELATIONS WITH CLINICAL MEASURES

5.4.1 Relationship between the brain lesion and the clinical picture

A major finding in this thesis is how apparent the link between the brain lesion and the clinical function became when fibre tractography was added as a method. This is clearly illustrated in two of the patients.

The first example is an individual (born 1989 at GA 33 weeks) who participated in Study III & IV (indexed as Subject C). The perinatal and neonatal history was uncomplicated, and presumably the WMDI occurred prenatally. Visual dysfunction is characterised by early onset strabismus, nystagmus and cognitive visual problems. She has no CP, and has completed a university degree. Ophthalmological examination revealed large cupping of the discs. Goldmann perimetries and Humphrey visual field analysis showed decreased sensitivity in the central inferior visual fields, but a close to normal extent for large stimuli. Ocular coherence tomography showed marked thinning of the RNFL and the superior GCL_IPL. The MRI showed bilateral WMDI with reduction of the periventricular white matter, most pronounced posteriorly, and fairly extensive gliosis bilaterally in the deep white matter. The anterior and posterior visual pathways were affected, and fibre tractography showed confinement of the OR-V1d tracts within the OR-V1v tracts on both sides (Figure 4-4:Subject C, p. 75). Clearly, there is a direct link between the WMDI, the thinning in the retina and the visual dysfunction.

However, interestingly, despite wide-spread periventricular gliosis, the reconstructed CST and TRS1 tracts were visually normal and passed through and in-between islets of gliosis in the corona radiata (Figure 5-1). On conventional MRI one could not have guessed that the motor and sensory tracts would have been spared.

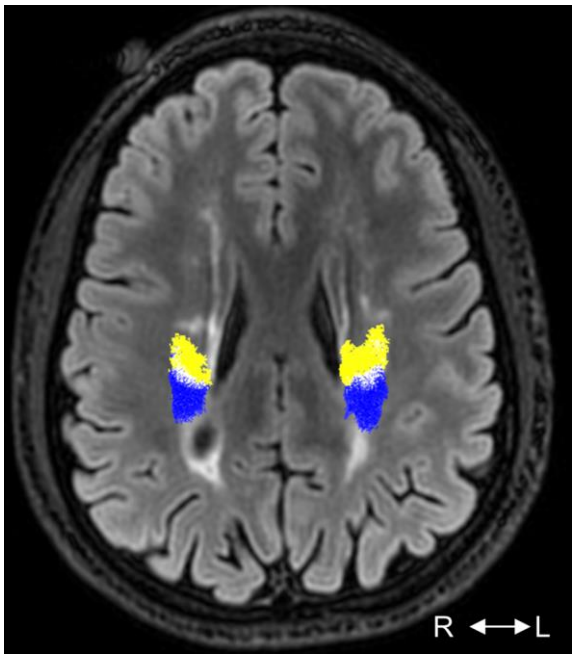

Figure 5-1: The CSTs (yellow) and the TRS1s (blue) tracts in an individual with WMDI and visual dysfunction, but no CP (Subject C in Study III & IV). Note how the tracts are passing in and between islet of gliosis at the level of the upper corona radiata. R=right, L=left.

The second example is an individual (born 1995 at GA 26 weeks) who participated in both Study I & II (indexed as Subject 12) and Study III & IV (indexed as Subject G). She has a left-sided unilateral CP, and managed a B&B score of 19 for the non-dominant hand, which is in the lower range. Visual dysfunction is characterised by cognitive visual problems, mainly dorsal stream, but normal visual fields. Ocular coherence tomography measurements showed normal thickness in the RNFL and GCL_IPL. The MRI can be seen in Figure 4-2 (p. 73) and Figure 4-4 (p. 75). These show bilateral WMDI with extensive reduction of the middle and posterior white matter, especially on the right side, and a porencephalic cyst in the right corona radiata, as a remnant of a PHI. Discrete gliosis is seen in the periventricular WM, and along the right CST. The right OR is believed to be affected on conventional MRI, but the rest of the visual pathways are normal. This picture is confirmed by the fibre tractography showing that the right TRS1 was impossible to track, the right CST was dislocated anteriorly, whereas the CST and the TRS1 on the left side and both the ORs were normal. The latter confirms that visual pathways are unaffected, despite the suspicion aroused by the conventional MRI, and her cognitive visual problems.

For both of these two individuals, the complete clinical and radiological picture fell into place when the fibre tractography of the tracts were analysed. This concludes that white matter tracts affected by early brain lesions ought to be evaluated with the most accurate methods available.

5.4.2 Correlations with hand motor function (Study I)

Study I showed that FA is a sensitive marker of injury to the cortico-fugal fibres on the side corresponding to the affected hand, and is negatively correlated with the B&B score in the affected hand, irrespective of lesion pattern. This is supported in a comparable study by Glenn et al (258) who, in a cohort of 17 individuals with unilateral CP and similar distribution of lesion types, evaluated DTI parameters in the CST at the level of the PLIC. They could show correlations between the asymmetry in the DTI parameters (increased MD and axial diffusivity and decreased FA on affected side) and the severity of the CP, irrespective of

lesion type. This is also supported by Bleyenhuft et al (259), who showed that the degree of cortical dysgenesis at the level of the cerebral peduncle (evaluated as the asymmetry of transverse area of the two sides CSTs, delineated from dMRI) correlated with upper-limb function, also irrespective of lesion type. Our interpretation of our findings and of these two studies, is that parametric changes in the descending motor tracts in locations more distant from the primary lesion site are sensitive in detecting injury, and correlate with clinical function, independent of the primary lesion type.

The intention of Study II was to explore these associations in the CST distant from (CST-PLIC to CerPed) and close to the primary lesion (CST-M1 to PLIC). However, it was not possible to track the CST and/or the TRS1 on the lesion-side in several individuals with B&B scores in the lower range (Figure 4-1, p. 72) and, therefore, no such associations could be explored.

5.4.3 Correlations with visual function (Study III & IV)

In Study III & IV, we presented convincing evidence for retrograde trans-synaptic degeneration (RTSD) in the immature visual system.

In Study III, we demonstrated a topographical correspondence between injury in the superior optic radiation (OR) and the thickness of the retinal nerve fibre layer (RNFL), causing predictable inferior visual field defects. In Study IV, by refinement of the fibre tracking method, we showed that the injuries in the superior portions of the OR, in fact, had a strict topographical correspondence with the thinning above the horizontal meridian in the macular ganglion cell complex (GCL_IPL; including the ganglion cell layer and the inner plexiform layers). Additionally, the ratio of the averaged thickness in the superior and inferior GCL_IPL in one eye correlated, indeed, negatively with the degree (increased $D_{//}$ and MD) of the injuries in the ipsi- and contralateral OR-V1d. RTSD in the visual system has been shown in animals (260–262), and one single-case histological study exists in humans (263), though the retina was not examined. The existence of RTSD in the human visual system is well-established, mainly by OCT studies of the RNFL and/or GCL_IPL in individuals with congenital injuries or acquired injuries to the posterior visual pathways (93,94). However, detailed analysis of the causality between the primary cerebral injuries and the secondary retinal thinning has not been studied until now. The importance of this is illustrated in a recent study in preterm newborns by Rothman et al (264), which showed thinning of the RNFL in the temporal quadrant and the papillomacular bundle in preterm newborns compared to term newborns. They suggested that the RNFL thinning in preterm newborns was related to brain structure abnormalities on MRI at term equivalent age, and level of general neurodevelopment at 18-24 months of age. This is an important study, as it suggests, in agreement with our conclusion in Study III, that OCT measurements could be used in the infant to detect early brain injuries. However, Rothman et al explored this by seeking associations between the RNFL thickness and a whole-brain MRI scoring system (265). Our study clearly showed that the causal link is specifically between injuries to the posterior visual pathways and the secondary retinal thinning. This is also illustrated in the two patients (Subjects E and G) with extensive WMDI but with-

out involving their ORs. Their OCTs showed normal GCL_IPL thicknesses, which then excluded the presence of RTSD. Therefore, explanations for abnormal OCT measurement must be sought in the visual system primarily, rather than elsewhere. Such a function-structure relationship should, as discussed in 5.4.1, be explored in other systems too, including the motor system.

5.5 INDICATIONS OF RE-ORGANISATION IN THE IMMATURE OPTIC RADIATION

One of the major results in this thesis is the suggestive re-organization of the immature optic radiation (OR) in Study IV.

The retinotopic fMRI mapping showed cortical activation in V1d, with expected anatomical location in the medial occipital cortex above the calcarine sulcus, and since none of the individuals had any deep, absolute inferior visual field (VF) defects (i.e. absolute VF defects reaching close to the horizontal meridian), we could be certain that the activation in V1d-ROI represented relevant cortical activation for a visual stimulus below the horizontal meridian. The is in line with a recent case-study by Merabet et al (133) using retintopic fMRI mapping in one individual with WMDI and inferior VF defects. Merabat et al showed a normal location of the early visual field maps in the occipital cortex. However, the cortical BOLD-response for visual stimulus in the inferior visual field was lower than the BOLD-response for visual stimulus in the superior visual field. This was congruent with the individual's inferior VF defects.

Retinotopic fMRI mapping allowed us to reconstruct the geniculo-striate connections to the dorsal (V1d) and ventral (V1v) subparts of the primary visual cortex. This generated the corresponding OR-V1d and OR-V1v tracts. In four patients we could give convincing evidence of retrograde trans-synaptic degeneration (RTSD) after injuries to the superior portion of the OR (discussed in 5.4.3). In those four individuals, we could see that the OR-V1d tracts were displaced, and to a large extent, encapsulated within the OR-V1v tracts (Figure 4-4, p. 75). This must be a lesion-invoked pattern, as we did not observe it in the other three patients without RTSD, nor in the controls. Since the streamlines in the displaced OR-V1d tract must, from a probabilistic fibre tracking perspective and the given dMRI data, represent the most probable connections to V1d, and, therefore, the results are suggestive of a re-organization of the OR in WMDI.

As outlined in 1.4.2, many studies attribute the general good visual recovery after early brain lesions to the potential of plasticity at the time of the insult. Our results are in line with previous case studies indicating ipsilesional re-organization with tracts "by-passing" the periventricular white matter lesions (92,133). Importantly, we cannot say whether this suggestive re-organisation is due to a strengthening of already existing connections or a recruitment of new fibres. Both explanations are possible, as WMDI occurs during the time frame of the developing connectivity (2). However, we could see that the suggestive mode of re-organization of the OR, when "by-passing" the WMDI lesion, was by displacing connections

according to the retinotopic organization of the OR, which is in line with the fundamental developmental mechanism of preserving the cortical maps (28).

5.6 GENERALISATION OF FINDINGS

Study I & II of the motor system consisted of the same cohort of children with unilateral CP, selected as a convenience sample with the aim of including children with a wide range of hand function. They had a range of lesion types including WMDI, focal infarcts and malformation of cortical development (one individual). A general issue concerning dMRI studies in CP is the heterogeneity of the studied CP groups (118), both with respect to included lesion types and the CP subtypes. This makes generalization difficult. In Study I & II the individuals had a common CP subtype, but different lesion types. However, by studying subparts of tracts in which the injury pattern is more homogenous, the sensitivity of the method seems to increase, despite a heterogeneity in the included lesion types. The descending motor pathways below the PLIC appear to be just such a subpart of the motor system. Our interpretation of our and other studies is that the diffusion parametric and structural changes in this area reflect secondary anterograde (Wallerian) degeneration from upstream, primary lesions and are, presumably, more independent of the primary lesion's aetiology. Given that our studies only had one individual with a lesion type of malformation of cortical development (bilateral polymicrogyria with unilateral schizencephaly), it is our belief that the results from Study I can be generalized to unilateral spastic CP for the destructive lesion types of WMDI and FI. Moreover, the results in Study II are, as discussed in 5.2 and 5.3.1, supported in previous studies. However, the DTI changes in the TRS1 on the lesion side and CST and TRS1 on the non-lesion side must be investigated more thoroughly, preferably using higher-order models, before drawing firm conclusions.

The main result from Study III & IV is the evidence of retrograde trans-synaptic degeneration (RTSD) in the immature visual system. The studies were multiple case-studies of seven patients with WMDI and visual dysfunctions. Among the seven patients, we could show clear evidence for RTSD in four individuals, and dismiss RTSD in three individuals. The results should, of course, be replicated in more patients with WMDI, and also other lesion types should be studied. However, the results give convincing evidence for a fundamental pathophysiological process known to exist in the human visual system, but as yet not shown this clearly *in vivo*.

6 CONCLUSIONS

This thesis has studied alterations to brain organization after injury during early brain development using diffusion-weighted MRI (dMRI) and fibre tractography, by specifically studying the motor system in individuals with unilateral CP and the visual system in individuals with WMDI and visual dysfunction.

Study I & II show that both the motor and sensory systems are affected in unilateral CP, with changes to both the gross morphology of the tract paths and to the tract microstructure. In the

cortico-fugal fibres distant from the primary lesion site, changes to tract microstructure, specifically the fractional anisotropy, correlated with hand motor function, independent of the lesion type.

Study III & IV showed a topographical correspondence between injuries to the superior portion of the optic radiation (OR) in WMDI and the thinning of the retinal nerve fibre layer and the macular ganglion cell complex, resulting in inferior visual field defects. These studies give compelling evidence for retrograde trans-synaptic degeneration in the immature visual system. The structural changes to the OR, specifically its superior portion projecting to the dorsal striate cortex (OR-V1d tract), suggest compensatory re-organisation in the OR upon injury.

Both the findings from the studies on the motor system and on the visual system conclude that in early brain lesions, dMRI is more sensitive in detecting and assessing the extent of injuries than conventional MRI. This is apparent from Study III & IV, where the extent of injury to the OR is overestimated in conventional MRI; from Study II & IV where alterations to the gross morphology of the tract paths in lesion-affected areas show connections by-passing lesions, even in areas of large lesions; and from Study II, where DTI parameters indicated involvement on the non-lesion side. In both systems, the degree of injury, inferred from changes in DTI parameters, correlated with relevant clinical measures: the hand-motor function in unilateral CP, and the retinal ganglion cell structure and visual field function in WMDI. This leads to the overall conclusion that dMRI is a sensitive marker for relevant structural entities of the underlying fibre tract that directly affect clinical function.

7 FUTURE DIRECTIONS

The research field of dMRI for investigating white matter pathways in early brain lesions is rapidly advancing, and recent studies are using increasingly advanced methodologies. However, the strength of the studies in this thesis has been the thorough investigation of clinically relevant research questions in carefully selected patient materials, rather than focusing on using advanced methodological approaches. I believe that this approach is also relevant for future studies investigating the white matter pathways in early brain lesions.

The data for Study I and II were collected in 2007, with a state-of-the art dMRI acquisition, at that time, for the available 1.5 T MR-instrument. Given the interesting results in the studies, primarily in Study II, it would be beneficial to replicate the study using more advanced dMRI. Firstly, to address the morphological alterations to the fibre tracts on the lesion-side by using improved fibre tractography and specific cortical targets, e.g. fMRI with sensorimotor activations, in order to understand the spatial representation of streamlines reaching different cortical locations within the CST and TRS1 tracts. Secondly, more advanced diffusion models should be employed to study lesion-invoked changes to individual fibre populations in the areas with complex fibre architecture, both on the lesion and on the non-lesion sides.

The results from Study III and IV ought to be investigated further, particularly the findings of re-organization of the OR. This could be done with the existing data, by mapping the cortical visual field maps along the OR to show how the spatial distribution of streamlines is related to the visual field map, not only the horizontal meridian. This would challenge the hypothesis of a preservation of the cortical map in early brain development. In addition, as suggested in Study IV, this ought to be done in individuals with lately acquired lesions causing visual field defects. It is already established that these individuals experience retrograde trans-synaptic degeneration of the retinal ganglion cells (93), but exactly how the retina is affected by the primary brain lesions and what the spatial distribution of streamlines in their ORs look like has not yet been investigated. Exploring this in more detail would provide important additional information on the compensatory mechanisms in early brain lesions.

My overall conclusion is, nevertheless, that future studies in the field of early brain lesions looking at structure-function relationships with a focus on clinically relevant areas, must aim to better understand the underlying pathophysiological processes in different types of early brain lesions, preferably in a joint effort between neuroimaging and neuropathology. Future studies ought to employ recently available, improved dMRI methodologies to better evaluate the true extent of the lesion, and to infer which specific structures that are, or have been, affected, including the transient developmental structures.

8 ACKNOWLEDGEMENTS

This may be the most read part of this, and I dare say any thesis! So the most important people come first, my family. Indy: without your love and support none of these pages would ever have been written. The same goes for the rest of our life journey! Also to our three children, Emile, Iris & Eden for bringing so much joy and meaning into our lives.

A huge thank you to all the participants in these studies: your efforts have been enormous, often travelling from afar, and you made all the difference to the end result!

I would also especially like to thank:

My main supervisor Olof Flodmark. On our meandering scientific journey you have supported me fully, made things possible and provided advice and direction whenever needed.

My co-supervisor Brigitte Vollmer, for your endless support and encouragement, ever since the first day we worked together on Study I, and thereafter in our joint research projects.

My co-supervisor Lena Jacobson, for your curious mind and desire to understand the visual system in early brain lesions. It has been a joint effort in the true meaning of the word.

My co-supervisor Jonas Larsson, for sharing your expertise in the field of visual neuroscience and your endless patience in coping with my computer issues.

My co-authors Linda Holmström, Ann-Christine Eliasson, Kristina Tedroff and Hans Forssberg at Astrid Lindgren Children's Hospital, Chris Clark at University College London, J-Donald Tournier at the King's College London, and Maria Nilsson at the St Erik's Eye Hospital. These studies have all come out of translational research projects and have been completely dependent on these people! A special thanks to Donald for inspiring discussions and invaluable help over all these years!

All the personnel at the Department for Neuroradiology at the Karolinska University Hospital. It has been a true pleasure working with you during these years!

My former boss Bo Nordell for introducing me to the field of MR-physics and giving me work as an MR-physicist during my medial studies.

Past and current colleagues of the MR-physics group at the Karolinska University Hospital.

Ljungby Hospital for generously giving me time off for research during my medical residency and the Department of Radiology for an inspiring residency, which made me decide on the path of radiology for my medical career!

The MR Research Centre at Karolinska Institutet / Karolinska University Hospital for providing vital resources for the project, and especially Martin Ingvar and Mimmi Wernman.

All the close friends I have made through life! From childhood in Stockholm, teenage years in Skåne, studies in Lund, Paris, Stockholm and Buenos Aires, the years in the Småland forest and recently back in Stockholm. You are too numerous to mention!

My parents Ingegerd and Moje for their never-ending support, even when I decided to go to medical school after finishing my engineering degree, and for bringing us up to believe in ourselves. And finally, my brother Mats and sister Rebecca with their families, for being close though living far away, and my extended family with Rosey, Andy and Aaron and Seth with families.

9 REFERENCES

1. Bystron I, Blakemore C, Rakic P. Development of the human cerebral cortex: Boulder Committee revisited. Nat Rev Neurosci. 2008 Feb;9(2):110–22.

2. Kostović I, Jovanov-Milošević N. The development of cerebral connections during the first 20–45 weeks' gestation. Semin Fetal Neonatal Med. 2006 Dec;11(6):415–22.

3. ten Donkelaar HJ, Lammens M, Hori A. Clinical Neuroembryology. Berlin, Heidelberg: Springer Berlin Heidelberg; 2014.

4. Shen Q, Wang Y, Dimos JT, Fasano CA, Phoenix TN, Lemischka IR, et al. The timing of cortical neurogenesis is encoded within lineages of individual progenitor cells. Nat Neurosci. 2006 Jun;9(6):743–51.

5. Kostović I, Judaš M. The development of the subplate and thalamocortical connections in the human foetal brain: Human foetal cortical circuitry. Acta Paediatr. 2010 Mar 29;99(8):1119–27.

6. Hevner RF. Development of connections in the human visual system during fetal mid-gestation: a DiI-tracing study. J Neuropathol Exp Neurol. 2000;59(5):385–92.

7. Eyre JA, Miller S, Clowry GJ, Conway EA, Watts C. Functional corticospinal projections are established prenatally in the human foetus permitting involvement in the development of spinal motor centres. Brain J Neurol. 2000 Jan;123 (Pt 1):51–64.

8. Raybaud C, Ahmad T, Rastegar N, Shroff M, Nassar M. The premature brain: developmental and lesional anatomy. Neuroradiology. 2013 Jul 7;55(S2):23–40.

9. Khazipov R, Luhmann HJ. Early patterns of electrical activity in the developing cerebral cortex of humans and rodents. Trends Neurosci. 2006 Jul;29(7):414–8.

10. Chi JG, Dooling EC, Gilles FH. Gyral development of the human brain. Ann Neurol. 1977;1(1):86–93.

11. Kostović I, Jovanov-Milošević N, Radoš M, Sedmak G, Benjak V, Kostović-Srzentić M, et al. Perinatal and early postnatal reorganization of the subplate and related cellular compartments in the human cerebral wall as revealed by histological and MRI approaches. Brain Struct Funct. 2012 Dec 19;219(1):231–53.

12. Volpe JJ. Brain injury in premature infants: a complex amalgam of destructive and developmental disturbances. Lancet Neurol. 2009;8(1):110–24.

13. Raybaud C. Normal and Abnormal Embryology and Development of the Intracranial Vascular System. Neurosurg Clin N Am. 2010 Jul;21(3):399–426.

14. Okudera T, Huang YP, Fukusumi A, Nakamura Y, Hatazawa J, Uemura K. Micro-angiographical studies of the medullary venous system of the cerebral hemisphere. Neuropathology. 1999 Jan 1;19(1):93–111.

15. du Plessis AJ. Cerebral Blood Flow and Metabolism in the Developing Fetus. Clin Perinatol. 2009 Sep;36(3):531–48.

16. Kehrer M, Blumenstock G, Ehehalt S, Goelz R, Poets C, Schöning M. Development of Cerebral Blood Flow Volume in Preterm Neonates during the First Two Weeks of Life. Pediatr Res. 2005 Nov;58(5):927–30.

17. Mitew S, Hay CM, Peckham H, Xiao J, Koenning M, Emery B. Mechanisms regulating the development of oligodendrocytes and central nervous system myelin. Neuroscience. 2014 Sep 12;276:29–47.

18. Verney C, Monier A, Fallet-Bianco C, Gressens P. Early microglial colonization of the human forebrain and possible involvement in periventricular white-matter injury of preterm infants. J Anat. 2010 Oct;217(4):436–48.

19. Freeman MR. Specification and morphogenesis of astrocytes. Science. 2010;330(6005):774–8.

20. Jessen NA, Munk ASF, Lundgaard I, Nedergaard M. The Glymphatic System: A Beginner's Guide. Neurochem Res. 2015 Dec;40(12):2583–99.

21. Purves D, editor. Neuroscience. 5th ed. Sunderland, Mass: Sinauer Associates; 2012. 1 p.

22. Martin JH. The Corticospinal System: From Development to Motor Control. The Neuroscientist. 2005 Apr 1;11(2):161–73.

23. Eyre JA, Taylor JP, Villagra F, Smith M, Miller S. Evidence of activity-dependent withdrawal of corticospinal projections during human development. Neurology. 2001 Nov 13;57(9):1543–54.

24. Eyre J. Corticospinal tract development and its plasticity after perinatal injury. Neurosci Biobehav Rev. 2007;31(8):1136–49.

25. Lin J-P. The Cerebral Palsies: A Physiological Approach. J Neurol Neurosurg Psychiatry. 2003 Jan 3;74(suppl 1):i23–9.

26. Wärntges S, Michelson G. Detailed Illustration of the Visual Field Representation along the Visual Pathway to the Primary Visual Cortex: A Graphical Summary. Ophthalmic Res. 2014;51(1):37–41.

27. Wandell BA, Dumoulin SO, Brewer AA. Visual Field Maps in Human Cortex. Neuron. 2007 Oct;56(2):366–83.

28. Shatz CJ. Emergence of order in visual system development. J Physiol-Paris. 1996;90(3):141–50.

29. Vanhatalo S, Kaila K. Development of neonatal EEG activity: From phenomenology to physiology. Semin Fetal Neonatal Med. 2006 Dec;11(6):471–8.

30. Kelly KR, McKetton L, Schneider KA, Gallie BL, Steeves JKE. Altered anterior visual system development following early monocular enucleation. NeuroImage Clin. 2014;4:72–81.

31. Braddick O, Atkinson J. Development of human visual function. Vision Res. 2011 Jul 1;51(13):1588–609.

32. Penn AA, Shatz CJ. Brain waves and brain wiring: the role of endogenous and sensory-driven neural activity in development. Pediatr Res. 1999 Apr;45(4 Pt 1):447–58.

33. Krägeloh-Mann I. Imaging of early brain injury and cortical plasticity. Exp Neurol. 2004 Nov;190:84–90.

34. Barkovich AJ, Millen KJ, Dobyns WB. A developmental and genetic classification for midbrain-hindbrain malformations. Brain. 2009 Dec 1;132(12):3199–230.

35. Barkovich AJ, Kuzniecky RI, Jackson GD, Guerrini R, Dobyns WB. A developmental and genetic classification for malformations of cortical development. Neurology. 2005 Dec 27;65(12):1873–87.

36. Barkovich AJ, Kuzniecky RI, Jackson GD, Guerrini R, Dobyns WB. Classification system for malformations of cortical development Update 2001. Neurology. 2001 Dec 26;57(12):2168–78.

37. Haydar TF, Kuan C-Y, Flavell RA, Rakic P. The Role of Cell Death in Regulating the Size and Shape of the Mammalian Forebrain. Cereb Cortex. 1999 Jan 9;9(6):621–6.

38. Barkovich AJ. Current concepts of polymicrogyria. Neuroradiology. 2010 Mar 3;52(6):479–87.

39. Barkovich AJ, Rowley H, Bollen A. Correlation of prenatal events with the development of polymicrogyria. Am J Neuroradiol. 1995 Jan 4;16(4):822–7.

40. Marques Dias M, Harmant-van Rijckevorsel G, Landrieu P, Lyon G. Prenatal Cytomegalovirus Disease and Cerebral Microgyria: Evidence for Perfusion Failure, not Disturbance of Histogenesis, as the Major Cause of Fetal Cytomegalovirus Encephalopathy. Neuropediatrics. 1984 Feb;15(01):18–24.

41. Barkovich AJ, Norman D. MR imaging of schizencephaly. Am J Neuroradiol. 1988;9(2):297–302.

42. Fernández-Bouzas A, Harmony T, Santiago-Rodríguez E, Ricardo-Garcell J, Fernández T, Avila-Acosta D. Schizencephaly with occlusion or absence of middle cerebral artery. Neuroradiology. 2006 Jan 4;48(3):171–5.

43. Volpe JJ. Neurology of the newborn. 5th ed. Philadelphia: Saunders/Elsevier; 2008. 1094 p.

44. Bax M, Tydeman C, Flodmark O. Clinical and MRI correlates of cerebral palsy. JAMA J Am Med Assoc. 2006;296(13):1602–8.

45. Banker B, Larroche J. Periventricular leukomalacia of infancy: A form of neonatal anoxic encephalopathy. Arch Neurol. 1962 Nov 1;7(5):386–410.

46. Greenfield JG, Love S, Louis DN, Ellison D. Greenfield's neuropathology. 8th ed. London: Hodder Arnold; 2008. 2 p.

47. Shuman RM, Selednik LJ. Periventricular leukomalacia: A one-year autopsy study. Arch Neurol. 1980 Apr 1;37(4):231–5.

48. Rutherford MA, Supramaniam V, Ederies A, Chew A, Bassi L, Groppo M, et al. Magnetic resonance imaging of white matter diseases of prematurity. Neuroradiology. 2010 Apr 27;52(6):505–21.

49. Volpe JJ, Kinney HC, Jensen FE, Rosenberg PA. The developing oligodendrocyte: key cellular target in brain injury in the premature infant. Int J Dev Neurosci. 2011 Jun;29(4):423–40.

50. Kinney HC, Back SA. Human oligodendroglial development: Relationship to periventricular leukomalacia. Semin Pediatr Neurol. 1998 Sep;5(3):180–9.

51. Back SA, Luo NL, Borenstein NS, Levine JM, Volpe JJ, Kinney HC. Late Oligodendrocyte Progenitors Coincide with the Developmental Window of Vulnerability for Human Perinatal White Matter Injury. J Neurosci. 2001 Feb 15;21(4):1302–12.

52. Back SA. Brain Injury in the Preterm Infant: New Horizons for Pathogenesis and Prevention. Pediatr Neurol. 2015 Sep;53(3):185–92.

53. Billiards SS, Haynes RL, Folkerth RD, Borenstein NS, Trachtenberg FL, Rowitch DH, et al. Myelin Abnormalities without Oligodendrocyte Loss in Periventricular Leukomalacia. Brain Pathol. 2008 Apr 1;18(2):153–63.

54. Deguchi K, Oguchi K, Matsuura N, Armstrong DD, Takashima S. Periventricular leukomalacia: relation to gestational age and axonal injury. Pediatr Neurol. 1999 May;20(5):370–4.

55. Haynes RL, Billiards SS, Borenstein NS, Volpe JJ, Kinney HC. Diffuse Axonal Injury in Periventricular Leukomalacia as Determined by Apoptotic Marker Fractin. Pediatr Res. 2008 Jun;63(6):656–61.

56. Pierson CR, Folkerth RD, Billiards SS, Trachtenberg FL, Drinkwater ME, Volpe JJ, et al. Gray matter injury associated with periventricular leukomalacia in the premature infant. Acta Neuropathol (Berl). 2007 Oct 3;114(6):619–31.

57. Talos DM, Follett PL, Folkerth RD, Fishman RE, Trachtenberg FL, Volpe JJ, et al. Developmental regulation of α-amino-3-hydroxy-5-methyl-4-isoxazole-propionic acid receptor subunit expression in forebrain and relationship to regional susceptibility to hypoxic/ischemic injury. II. Human cerebral white matter and cortex. J Comp Neurol. 2006 Jul 1;497(1):61–77.

58. Robinson S, Li Q, DeChant A, Cohen ML. Neonatal loss of γ–aminobutyric acid pathway expression after human perinatal brain injury. J Neurosurg Pediatr. 2006 Jun 1;104(6):396–408.

59. Pogledic I, Kostovic I, Fallet-Bianco C, Adle-Biassette H, Gressens P, Verney C. Involvement of the subplate zone in preterm infants with periventricular white matter injury. Brain Pathol Zurich Switz. 2014 Mar;24(2):128–41.

60. Iida K, Takashima S, Takeuchi Y. Etiologies and distribution of neonatal leukomalacia. Pediatr Neurol. 1992 May;8(3):205–9.

61. Inder TE, Warfield SK, Wang H, Hüppi PS, Volpe JJ. Abnormal Cerebral Structure Is Present at Term in Premature Infants. Pediatrics. 2005 Jan 2;115(2):286–94.

62. Verney C, Pogledic I, Biran V, Adle-Biassette H, Fallet-Bianco C, Gressens P. Microglial reaction in axonal crossroads is a hallmark of noncystic periventricular white matter injury in very preterm infants. J Neuropathol Exp Neurol. 2012 Mar;71(3):251–64.

63. Anstrom JA, Brown WR, Moody DM, Thore CR, Challa VR, Block SM. Subependymal veins in premature neonates: implications for hemorrhage. Pediatr Neurol. 2004 Jan;30(1):46–53.

64. Ballabh P. Intraventricular Hemorrhage in Premature Infants: Mechanism of Disease. Pediatr Res. 2010 Jan;67(1):1–8.

65. Takashima S, Mito T, Ando Y. Pathogenesis of periventricular white matter hemorrhages in preterm infants. Brain Dev. 1986;8(1):25–30.

66. Maitre NL, Marshall DD, Price WA, Slaughter JC, O'Shea TM, Maxfield C, et al. Neurodevelopmental Outcome of Infants With Unilateral or Bilateral Periventricular Hemorrhagic Infarction. Pediatrics. 2009 Jan 12;124(6):e1153–60.

67. Staudt M. Reorganization after pre- and perinatal brain lesions*. J Anat. 2010 Oct 1;217(4):469–74.

68. Chugani HT. Review : Metabolic Imaging: A Window on Brain Development and Plasticity. The Neuroscientist. 1999 Jan 1;5(1):29–40.

69. Martinez-Biarge M, Diez-Sebastian J, Kapellou O, Gindner D, Allsop JM, Rutherford MA, et al. Predicting motor outcome and death in term hypoxic-ischemic encephalopathy. Neurology. 2011 Jun 14;76(24):2055–61.

70. Barkovich AJ, Hajnal BL, Vigneron D, Sola A, Partridge JC, Allen F, et al. Prediction of neuromotor outcome in perinatal asphyxia: evaluation of MR scoring systems. Am J Neuroradiol. 1998 Jan 1;19(1):143–9.

71. Nelson KB. Perinatal Ischemic Stroke. Stroke. 2007 Feb 1;38(2):742–5.

72. Schulzke S, Weber P, Luetschg J, Fahnenstich H. Incidence and diagnosis of unilateral arterial cerebral infarction in newborn infants. J Perinat Med. 2005;33(2):170–5.

73. Rosenbaum P, Paneth N, Leviton A, Goldstein M, Bax M, Damiano D, et al. A report: the definition and classification of cerebral palsy April 2006. Dev Med Child Neurol Suppl. 2007 Feb;109:8–14.

74. Himmelmann K, Uvebrant P. The panorama of cerebral palsy in Sweden. XI. Changing patterns in the birth-year period 2003-2006. Acta Paediatr. 2014 Jun;103(6):618–24.

75. Sellier E, Platt MJ, Andersen GL, Krägeloh-Mann I, De La Cruz J, Cans C, et al. Decreasing prevalence in cerebral palsy: a multi-site European population-based study, 1980 to 2003. Dev Med Child Neurol. 2016 Jan 1;58(1):85–92.

76. Uvebrant P. Hemiplegic cerebral palsy. Aetiology and outcome. Acta Paediatr Scand Suppl. 1988;345:1–100.

77. Mackenzie SJ, Getchell N, Modlesky CM, Miller F, Jaric S. Using grasping tasks to evaluate hand force coordination in children with hemiplegic cerebral palsy. Arch Phys Med Rehabil. 2009 Aug;90(8):1439–42.

78. Krumlinde-Sundholm L, Eliasson A-C. Comparing tests of tactile sensibility: aspects relevant to testing children with spastic hemiplegia. Dev Med Child Neurol. 2002;44(9):604–12.

79. Eliasson A-C, Krumlinde-Sundholm L, Rösblad B, Beckung E, Arner M, Öhrvall A-M, et al. The Manual Ability Classification System (MACS) for children with cerebral palsy: scale development and evidence of validity and reliability. Dev Med Child Neurol. 2006;48(07):549–54.

80. Mathiowetz V, Volland G, Kashman N, Weber K. Adult norms for the Box and Block Test of manual dexterity. Am J Occup Ther Off Publ Am Occup Ther Assoc. 1985 Jun;39(6):386–91.

81. Jacobson L, Flodmark O, Martin L. Visual field defects in prematurely born patients with white matter damage of immaturity: a multiple-case study. Acta Ophthalmol Scand. 2006;84(3):357–62.

82. Jacobson L, Rydberg A, Eliasson A-C, Kits A, Flodmark O. Visual field function in school-aged children with spastic unilateral cerebral palsy related to different patterns of brain damage: Visual Field Function in Children with Spastic Unilateral CP. Dev Med Child Neurol. 2010 Jan 28;52(8):e184–7.

83. Black P. Visual disorders associated with cerebral palsy. Br J Ophthalmol. 1982;66(1):46–52.

84. Jacobson L, Ygge J, Flodmark O. Nystagmus in periventricular leucomalacia. Br J Ophthalmol. 1998 Jan 9;82(9):1026–32.

85. Salati R, Borgatti R, Giammari G, Jacobson L. Oculomotor dysfunction in cerebral visual impairment following perinatal hypoxia. Dev Med Child Neurol. 2002 Aug 1;44(8):542–50.

86. Pansell T, Hellgren K, Jacobson L, Brautaset R, Tedroff K. The accommodative process in children with cerebral palsy: different strategies to obtain clear vision at short distance. Dev Med Child Neurol. 2014 Feb 1;56(2):171–7.

87. Cioni G, Fazzi B, Coluccini M, Bartalena L, Boldrini A, van Hof-van Duin J. Cerebral visual impairment in preterm infants with periventricular leukomalacia. Pediatr Neurol. 1997 Nov;17(4):331–8.

88. Rahi JS, Cable N, British Childhood Visual Impairment Study Group. Severe visual impairment and blindness in children in the UK. Lancet Lond Engl. 2003 Oct 25;362(9393):1359–65.

89. Rosenberg T, Flage T, Hansen E, Riise R, Rudanko S-L, Viggosson G, et al. Incidence of registered visual impairment in the Nordic child population. Br J Ophthalmol. 1996;80(1):49–53.

90. Mitry D, Bunce C, Wormald R, Bowman R. Childhood visual impairment in England: a rising trend. Arch Dis Child. 2013 May;98(5):378–80.

91. Knyazeva MG, Maeder P, Kiper DC, Deonna T, Innocenti GM. Vision after early-onset lesions of the occipital cortex: II. Physiological studies. Neural Plast. 2002;9(1):27–40.

92. Guzzetta A, D'Acunto G, Rose S, Tinelli F, Boyd R, Cioni G. Plasticity of the visual system after early brain damage: Review. Dev Med Child Neurol. 2010 Oct;52(10):891–900.

93. Jindahra P, Petrie A, Plant GT. Retrograde trans-synaptic retinal ganglion cell loss identified by optical coherence tomography. Brain. 2009 Jan 21;132(3):628–34.

94. Mitchell JR, Oliveira C, Tsiouris AJ, Dinkin MJ. Corresponding Ganglion Cell Atrophy in Patients With Postgeniculate Homonymous Visual Field Loss: J Neuroophthalmol. 2015 Dec;35(4):353–9.

95. Jacobson L, Hellström A, Flodmark O. Large cups in normal-sized optic discsa variant of optic nerve hypoplasia in children with periventricular leukomalacia. Arch Ophthalmol. 1997;115(10):1263–9.

96. Cans C, Dolk H, Platt MJ, Colver A, Prasauskiene A, Krägeloh-Mann IK. Recommendations from the SCPE collaborative group for defining and classifying cerebral palsy. Dev Med Child Neurol. 2007;49(s109):35–8.

97. Johnson MA, Pennock JM, Bydder GM, Steiner RE, Thomas DJ, Hayward R, et al. Clinical NMR Imaging of the Brain in Children: Normal and Neurologic Disease. Am J Neuroradiol. 1983 Jan 9;4(5):1013–26.

98. Flodmark O, Lupton B, Li D, Stimac GK, Roland EH, Hill A, et al. MR imaging of periventricular leukomalacia in childhood. Am J Neuroradiol. 1989;10(1):111–8.

99. Flodmark O. The brain imaging perspective. Dev Med Child Neurol. 2007;49(s109):18–9.

100. Uggetti C, Egitto MG, Fazzi E, Bianchi PE, Zappoli F, Martelli A, et al. Transsynaptic degeneration of lateral geniculate bodies in blind children: in vivo MR demonstration. Am J Neuroradiol. 1997;18(2):233–8.

101. Rutherford M, Malamateniou C, McGuinness A, Allsop J, Biarge MM, Counsell S. Magnetic resonance imaging in hypoxic-ischaemic encephalopathy. Early Hum Dev. 2010 Jun;86(6):351–60.

102. Filan PM, Inder TE, Cameron FJ, Kean MJ, Hunt RW. Neonatal hypoglycemia and occipital cerebral injury. J Pediatr. 2006 Apr;148(4):552–5.

103. Cans C. Surveillance of cerebral palsy in Europe: a collaboration of cerebral palsy surveys and registers. Dev Med Child Neurol. 2000;42(12):816–24.

104. Krägeloh-Mann I, Horber V. The role of magnetic resonance imaging in elucidating the pathogenesis of cerebral palsy: a systematic review. Dev Med Child Neurol. 2007;49(2):144–51.

105. Serdaroglu G, Tekgul H, Kitis O, Serdaroglu E, Gökben S. Correlative value of magnetic resonance imaging for neurodevelopmental outcome in periventricular leukomalacia. Dev Med Child Neurol. 2004 Nov;46(11):733–9.

106. Staudt M, Niemann G, Grodd W, Krägeloh-Mann I. The pyramidal tract in congenital hemiparesis: relationship between morphology and function in periventricular lesions. Neuropediatrics. 2000 Oct;31(5):257–64.

107. Krägeloh-Mann I, Helber A, Mader I, Staudt M, Wolff M, Groenendaal F, et al. Bilateral lesions of thalamus and basal ganglia: origin and outcome. Dev Med Child Neurol. 2002 Jul 1;44(7):477–84.

108. Duque J, Thonnard J-L, Vandermeeren Y, Sébire G, Cosnard G, Olivier E. Correlation between impaired dexterity and corticospinal tract dysgenesis in congenital hemiplegia. Brain. 2003 Mar 1;126(3):732–47.

109. Arnfield E, Guzzetta A, Boyd R. Relationship between brain structure on magnetic resonance imaging and motor outcomes in children with cerebral palsy: A systematic review. Res Dev Disabil. 2013 Jul;34(7):2234–50.

110. Palisano R, Rosenbaum P, Walter S, Russell D, Wood E, Galuppi B. Development and reliability of a system to classify gross motor function in children with cerebral palsy. Dev Med Child Neurol. 1997 Apr;39(4):214–23.

111. Fiori S, Cioni G, Klingels K, Ortibus E, Van Gestel L, Rose S, et al. Reliability of a novel, semi-quantitative scale for classification of structural brain magnetic resonance imaging in children with cerebral palsy. Dev Med Child Neurol. 2014 Sep;56(9):839–45.

112. Shiran SI, Weinstein M, Sirota-Cohen C, Myers V, Ben Bashat D, Fattal-Valevski A, et al. MRI-Based Radiologic Scoring System for Extent of Brain Injury in Children with Hemiplegia. Am J Neuroradiol. 2014 Dec;35(12):2388–96.

113. Guzzetta A, Cioni G, Cowan F, Mercuri E. Visual disorders in children with brain lesions:: 1. Maturation of visual function in infants with neonatal brain lesions: correlation with neuroimaging. Eur J Paediatr Neurol. 2001 May;5(3):107–14.

114. Uggetti C, Egitto MG, Fazzi E, Bianchi PE, Bergamaschi R, Zappoli F, et al. Cerebral visual impairment in periventricular leukomalacia: MR correlation. Am J Neuroradiol. 1996;17(5):979–85.

115. Mercuri E, Atkinson J, Braddick O, Anker S, Nokes L, Cowan F, et al. Visual function and perinatal focal cerebral infarction. Arch Dis Child - Fetal Neonatal Ed. 1996 Jan 9;75(2):F76–81.

116. Dumoulin SO, Jirsch JD, Bernasconi A. Functional organization of human visual cortex in occipital polymicrogyria. Hum Brain Mapp. 2007 Dec;28(12):1302–12.

117. Mercuri E, Atkinson J, Braddick O, Anker S, Cowan F, Rutherford M, et al. Basal ganglia damage and impaired visual function in the newborn infant. Arch Dis Child - Fetal Neonatal Ed. 1997 Jan 9;77(2):F111–4.

118. Scheck SM, Boyd RN, Rose SE. New insights into the pathology of white matter tracts in cerebral palsy from diffusion magnetic resonance imaging: a systematic review: Review. Dev Med Child Neurol. 2012 Aug;54(8):684–96.

119. Holmstrom L, Lennartsson F, Eliasson A-C, Flodmark O, Clark C, Tedroff K, et al. Diffusion MRI in corticofugal fibers correlates with hand function in unilateral cerebral palsy. Neurology. 2011 Aug 10;77(8):775–83.

120. Thomas B, Eyssen M, Peeters R, Molenaers G, Van Hecke P, De Cock P, et al. Quantitative diffusion tensor imaging in cerebral palsy due to periventricular white matter injury. Brain J Neurol. 2005 Nov;128(Pt 11):2562–77.

121. Weinstein M, Green D, Geva R, Schertz M, Fattal-Valevski A, Artzi M, et al. Interhemispheric and intrahemispheric connectivity and manual skills in children with unilateral cerebral palsy. Brain Struct Funct. 2014 May;219(3):1025–40.

122. Pannek K, Boyd RN, Fiori S, Guzzetta A, Rose SE. Assessment of the structural brain network reveals altered connectivity in children with unilateral cerebral palsy due to periventricular white matter lesions. NeuroImage Clin. 2014;5:84–92.

123. Koerte I, Pelavin P, Kirmess B, Fuchs T, Berweck S, Laubender RP, et al. Anisotropy of transcallosal motor fibres indicates functional impairment in children with periventricular leukomalacia: Anisotropy of Motor Fibres in PVL. Dev Med Child Neurol. 2011 Feb;53(2):179–86.

124. Scheck SM, Pannek K, Raffelt DA, Fiori S, Boyd RN, Rose SE. Structural connectivity of the anterior cingulate in children with unilateral cerebral palsy due to white matter lesions. NeuroImage Clin. 2015;9:498–505.

125. Tsao H, Pannek K, Boyd RN, Rose SE. Changes in the integrity of thalamocortical connections are associated with sensorimotor deficits in children with congenital hemiplegia. Brain Struct Funct. 2015 Jan;220(1):307–18.

126. Englander ZA, Pizoli CE, Batrachenko A, Sun J, Worley G, Mikati MA, et al. Diffuse reduction of white matter connectivity in cerebral palsy with specific vulnerability of long range fiber tracts. NeuroImage Clin. 2013;2:440–7.

127. Lennartsson F, Holmstrom L, Eliasson A-C, Flodmark O, Forssberg H, Tournier J-D, et al. Advanced Fiber Tracking in Early Acquired Brain Injury Causing Cerebral Palsy. Am J Neuroradiol. 2015 Jan;36:181–7.

128. Farquharson S, Tournier J-D, Calamante F, Fabinyi G, Schneider-Kolsky M, Jackson GD, et al. White matter fiber tractography: why we need to move beyond DTI. J Neurosurg. 2013 Mar 29;118(6):1367–77.

129. Bleyenheuft Y, Dricot L, Gilis N, Kuo H-C, Grandin C, Bleyenheuft C, et al. Capturing neuroplastic changes after bimanual intensive rehabilitation in children with unilateral spastic cerebral palsy: A combined DTI, TMS and fMRI pilot study. Res Dev Disabil. 2015 Aug;43–44:136–49.

130. Trivedi R, Gupta RK, Shah V, Tripathi M, Rathore RKS, Kumar M, et al. Treatment-Induced Plasticity in Cerebral Palsy: A Diffusion Tensor Imaging Study. Pediatr Neurol. 2008 Nov;39(5):341–9.

131. Englander ZA, Sun J, Case L, Mikati MA, Kurtzberg J, Song AW. Brain structural connectivity increases concurrent with functional improvement: Evidence from diffusion tensor MRI in children with cerebral palsy during therapy. NeuroImage Clin. 2015;7:315–24.

132. Seghier ML, Lazeyras F, Zimine S, Saudan-Frei S, Safran AB, Huppi PS. Visual recovery after perinatal stroke evidenced by functional and diffusion MRI: case report. BMC Neurol. 2005;5(1):17.

133. Merabet LB, Devaney KJ, Bauer CM, Panja A, Heidary G, Somers DC. Characterizing Visual Field Deficits in Cerebral/Cortical Visual Impairment (CVI) Using Combined Diffusion Based Imaging and Functional Retinotopic Mapping: A Case Study. Front Syst Neurosci. 2016;13.

134. Bassi L, Ricci D, Volzone A, Allsop JM, Srinivasan L, Pai A, et al. Probabilistic diffusion tractography of the optic radiations and visual function in preterm infants at term equivalent age. Brain. 2008 Feb 1;131(2):573–82.

135. Berman JI, Glass HC, Miller SP, Mukherjee P, Ferriero DM, Barkovich AJ, et al. Quantitative Fiber Tracking Analysis of the Optic Radiation Correlated with Visual Performance in Premature Newborns. Am J Neuroradiol. 2008 Aug 7;30(1):120–4.

136. Glass HC, Berman JI, Norcia AM, Rogers EE, Henry RG, Hou C, et al. Quantitative Fiber Tracking of the Optic Radiation Is Correlated with Visual-Evoked Potential Amplitude in Preterm Infants. Am J Neuroradiol. 2010 May 6;31(8):1424–9.

137. Groppo M, Ricci D, Bassi L, Merchant N, Doria V, Arichi T, et al. Development of the optic radiations and visual function after premature birth. Cortex. 2014 Jul;56:30–7.

138. Pavaine J, Young JM, Morgan BR, Shroff M, Raybaud C, Taylor MJ. Diffusion tensor imaging-based assessment of white matter tracts and visual-motor outcomes in very preterm neonates. Neuroradiology. 2016 Mar 21;58(3):301–10.

139. Kennard M, Fulton J. Age and reorganization of central nervous system. Mt Sinai J Med. 1942;9:594–606.

140. Staudt M. Brain Plasticity Following Early Life Brain Injury: Insights From Neuroimaging. Semin Perinatol. 2010 Feb;34(1):87–92.

141. Carr LJ. Development and reorganization of descending motor pathways in children with hemiplegic cerebral palsy. Acta Paediatr Oslo Nor 1992 Suppl. 1996 Oct;416:53–7.

142. Guzzetta A, Bonanni P, Biagi L, Tosetti M, Montanaro D, Guerrini R, et al. Reorganisation of the somatosensory system after early brain damage. Clin Neurophysiol. 2007 May;118(5):1110–21.

143. Holmstrom L, Vollmer B, Tedroff K, Islam M, Persson JK, Kits A, et al. Hand function in relation to brain lesions and corticomotor-projection pattern in children with unilateral cerebral palsy: Hand Function and Brain Lesions in Unilateral CP. Dev Med Child Neurol. 2010 Feb;52(2):145–52.

144. Wilke M, Staudt M, Juenger H, Grodd W, Braun C, Krägeloh-Mann I. Somatosensory system in two types of motor reorganization in congenital hemiparesis: Topography and function. Hum Brain Mapp. 2009 Mar;30(3):776–88.

145. Staudt M, Braun C, Gerloff C, Erb M, Grodd W, Krägeloh-Mann I. Developing somatosensory projections bypass periventricular brain lesions. Neurology. 2006 Aug 8;67(3):522–5.

146. Arichi T, Counsell SJ, Allievi AG, Chew AT, Martinez-Biarge M, Mondi V, et al. The effects of hemorrhagic parenchymal infarction on the establishment of sensori-motor structural and functional connectivity in early infancy. Neuroradiology. 2014 Aug 14;56(11):985–94.

147. Rose S, Guzzetta A, Pannek K, Boyd R. MRI structural connectivity, disruption of primary sensorimotor pathways, and hand function in cerebral palsy. Brain Connect. 2011;1(4):309–16.

148. Ramenghi LA, Ricci D, Mercuri E, Groppo M, De Carli A, Ometto A, et al. Visual performance and brain structures in the developing brain of pre-term infants. Early Hum Dev. 2010 Jul;86(1, Supplement):73–5.

149. Guzzetta A, Fazzi B, Mercuri E, Bertuccelli B, Canapicchi R, van Hof-van Duin J, et al. Visual function in children with hemiplegia in the first years of life. Dev Med Child Neurol. 2001 May;43(5):321–9.

150. Zesiger P, Kiper D, Maeder P, Deonna T, Innocenti GM. Preserved visual function in a case of occipitoparietal microgyria. Ann Neurol. 2002 Oct;52(4):492–8.

151. Muckli L, Naumer MJ, Singer W. Bilateral visual field maps in a patient with only one hemisphere. Proc Natl Acad Sci. 2009;106(31):13034–9.

152. Guzzetta A, Fiori S, Scelfo D, Conti E, Bancale A. Reorganization of visual fields after periventricular haemorrhagic infarction: potentials and limitations. Dev Med Child Neurol. 2013 Nov;55:23–6.

153. Ricci D, Luciano R, Baranello G, Veredice C, Cesarini L, Bianco F, et al. Visual development in infants with prenatal post-haemorrhagic ventricular dilatation. Arch Dis Child - Fetal Neonatal Ed. 2007 Jan 24;92(4):F255–8.

154. Mercuri E, Anker S, Guzzetta A, Barnett A, Haataja L, Rutherford M, et al. Neonatal cerebral infarction and visual function at school age. Arch Dis Child - Fetal Neonatal Ed. 2003 Jan 11;88(6):F487–91.

155. Mercuri E, Haataja L, Guzzetta A, Anker S, Cowan F, Rutherford M, et al. Visual function in term infants with hypoxic-ischaemic insults: correlation with neurodevelopment at 2 years of age. Arch Dis Child - Fetal Neonatal Ed. 1999 Jan 3;80(2):F99–104.

156. Mansfield P. Multi-planar image formation using NMR spin echoes. J Phys C Solid State Phys. 1977 Feb;10:L55–8.

157. Beaulieu C. The basis of anisotropic water diffusion in the nervous system - a technical review. NMR Biomed. 2002 Nov;15(7-8):435–55.

158. Helenius J, Soinne L, Perkiö J, Salonen O, Kangasmäki A, Kaste M, et al. Diffusion-Weighted MR Imaging in Normal Human Brains in Various Age Groups. Am J Neuroradiol. 2002 Jan 2;23(2):194–9.

159. Hüppi PS, Dubois J. Diffusion tensor imaging of brain development. Semin Fetal Neonatal Med. 2006 Dec;11(6):489–97.

160. Partridge SC, Mukherjee P, Henry RG, Miller SP, Berman JI, Jin H, et al. Diffusion tensor imaging: serial quantitation of white matter tract maturity in premature newborns. NeuroImage. 2004 Jul;22(3):1302–14.

161. Wimberger DM, Roberts TP, Barkovich AJ, Prayer LM, Moseley ME, Kucharczyk J. Identification of 'premyelination' by diffusion-weighted MRI. J Comput Assist Tomogr. 1995 Feb;19(1):28–33.

162. Kinney HC, Brody BA, Kloman AS, Gilles FH. Sequence of Central Nervous System Myelination in Human Infancy. J Neuropathol Exp Neurol. 1988 May 1;47(3):217–34.

163. Tournier J-D, Mori S, Leemans A. Diffusion tensor imaging and beyond. Magn Reson Med. 2011 Jun;65(6):1532–56.

164. Jeurissen B, Leemans A, Tournier J-D, Jones DK, Sijbers J. Investigating the prevalence of complex fiber configurations in white matter tissue with diffusion magnetic resonance imaging: Prevalence of Multifiber Voxels in WM. Hum Brain Mapp. 2013 Nov;34(11):2747–66.

165. Stejskal EO, Tanner JE. Spin Diffusion Measurements: Spin Echoes in the Presence of a Time-Dependent Field Gradient. J Chem Phys. 1965 Jan 1;42(1):288–92.

166. Le Bihan D, van Zijl P. From the diffusion coefficient to the diffusion tensor. NMR Biomed. 2002 Nov;15(7-8):431–4.

167. Pruessmann KP, Weiger M, Scheidegger MB, Boesiger P. SENSE: sensitivity encoding for fast MRI. Magn Reson Med. 1999;42(5):952–62.

168. Griswold MA, Jakob PM, Heidemann RM, Nittka M, Jellus V, Wang J, et al. Generalized autocalibrating partially parallel acquisitions (GRAPPA). Magn Reson Med. 2002 Jun;47(6):1202–10.

169. Bammer R. Basic principles of diffusion-weighted imaging. Eur J Radiol. 2003 Mar;45(3):169–84.

170. Bammer R, Holdsworth SJ, Veldhuis WB, Skare ST. New methods in Diffusion Weighted and Diffusion Tensor Imaging. Magn Reson Imaging Clin N Am. 2009 May;17(2):175–204.

171. Reese TG, Heid O, Weisskoff RM, Wedeen VJ. Reduction of eddy-current-induced distortion in diffusion MRI using a twice-refocused spin echo. Magn Reson Med. 2003 Jan;49(1):177–82.

172. Andersson JLR, Skare S, Ashburner J. How to correct susceptibility distortions in spin-echo echo-planar images: application to diffusion tensor imaging. NeuroImage. 2003 Oct;20(2):870–88.

173. Andersson JLR, Sotiropoulos SN. An integrated approach to correction for off-resonance effects and subject movement in diffusion MR imaging. NeuroImage. 2016 Jan;125:1063–78.

174. Basser PJ, Mattiello J, LeBihan D. Estimation of the effective self-diffusion tensor from the NMR spin echo. J Magn Reson B. 1994 Mar;103(3):247–54.

175. Basser PJ, Pierpaoli C. Microstructural and physiological features of tissues elucidated by quantitative-diffusion-tensor MRI. J Magn Reson B. 1996 Jun;111(3):209–19.

176. Pajevic S, Pierpaoli C. Color schemes to represent the orientation of anisotropic tissues from diffusion tensor data: application to white matter fiber tract mapping in the human brain. Magn Reson Med. 1999 Sep;42(3):526–40.

177. Alexander DC, Barker GJ. Optimal imaging parameters for fiber-orientation estimation in diffusion MRI. NeuroImage. 2005 Aug 15;27(2):357–67.

178. Jones DK, Horsfield MA, Simmons A. Optimal strategies for measuring diffusion in anisotropic systems by magnetic resonance imaging. Magn Reson Med. 1999;42:515–25.

179. Samuel Groeschel, J-Donald Tournier, Gemma B. Northam, Torsten Baldeweg, John Wyatt, Brigitte Vollmer, et al. Identification and interpretation of microstructural abnormalities in motor pathways in adolescents born preterm. NeuroImage. 2014;87:209–19.

180. Wheeler-Kingshott CAM, Cercignani M. About 'axial' and 'radial' diffusivities. Magn Reson Med. 2009 May;61(5):1255–60.

181. Pierpaoli C, Barnett A, Pajevic S, Chen R, Penix L, Virta A, et al. Water Diffusion Changes in Wallerian Degeneration and Their Dependence on White Matter Architecture. NeuroImage. 2001 Jun;13(6):1174–85.

182. Jensen JH, Helpern JA, Ramani A, Lu H, Kaczynski K. Diffusional kurtosis imaging: The quantification of non-gaussian water diffusion by means of magnetic resonance imaging. Magn Reson Med. 2005 Jun 1;53(6):1432–40.

183. Wu EX, Cheung MM. MR diffusion kurtosis imaging for neural tissue characterization. NMR Biomed. 2010 Aug 1;23(7):836–48.

184. Wedeen VJ, Hagmann P, Tseng W-YI, Reese TG, Weisskoff RM. Mapping complex tissue architecture with diffusion spectrum magnetic resonance imaging. Magn Reson Med. 2005 Dec;54(6):1377–86.

185. Jones DK, editor. Diffusion MRI: theory, methods, and application. Oxford ; New York: Oxford University Press; 2010. 767 p.

186. Assaf Y, Basser PJ. Composite hindered and restricted model of diffusion (CHARMED) MR imaging of the human brain. NeuroImage. 2005 Aug 1;27(1):48–58.

187. Assaf Y, Blumenfeld-Katzir T, Yovel Y, Basser PJ. Axcaliber: A method for measuring axon diameter distribution from diffusion MRI. Magn Reson Med. 2008 Jun 1;59(6):1347–54.

188. De Santis S, Assaf Y, Evans CJ, Jones DK. Improved precision in CHARMED assessment of white matter through sampling scheme optimization and model parsimony testing. Magn Reson Med. 2014 Feb 1;71(2):661–71.

189. Zhang H, Schneider T, Wheeler-Kingshott CA, Alexander DC. NODDI: Practical in vivo neurite orientation dispersion and density imaging of the human brain. NeuroImage. 2012 Jul 16;61(4):1000–16.

190. Behrens TEJ, Woolrich MW, Jenkinson M, Johansen-Berg H, Nunes RG, Clare S, et al. Characterization and propagation of uncertainty in diffusion-weighted MR imaging. Magn Reson Med. 2003 Nov;50(5):1077–88.

191. Behrens TEJ, Berg HJ, Jbabdi S, Rushworth MFS, Woolrich MW. Probabilistic diffusion tractography with multiple fibre orientations: What can we gain? NeuroImage. 2007 Jan;34(1):144–55.

192. Jbabdi S, Sotiropoulos SN, Savio AM, Graña M, Behrens TEJ. Model-based analysis of multishell diffusion MR data for tractography: How to get over fitting problems. Magn Reson Med. 2012 Dec 1;68(6):1846–55.

193. Sotiropoulos SN, Jbabdi S, Xu J, Andersson JL, Moeller S, Auerbach EJ, et al. Advances in diffusion MRI acquisition and processing in the Human Connectome Project. NeuroImage. 2013 Oct;80:125–43.

194. Jenkinson M, Beckmann CF, Behrens TEJ, Woolrich MW, Smith SM. FSL. NeuroImage. 2012 Aug;62(2):782–90.

195. Tuch DS. Q-ball imaging. Magn Reson Med. 2004 Dec 1;52(6):1358–72.

196. Jansons KM, Alexander DC. Persistent Angular Structure: new insights from diffusion MRI data. Dummy version. Inf Process Med Imaging Proc Conf. 2003 Jul;18:672–83.

197. Tournier J-D, Calamante F, Gadian DG, Connelly A. Direct estimation of the fiber orientation density function from diffusion-weighted MRI data using spherical deconvolution. NeuroImage. 2004 Nov;23(3):1176–85.

198. Tournier J-D, Calamante F, Connelly A. Robust determination of the fibre orientation distribution in diffusion MRI: non-negativity constrained super-resolved spherical deconvolution. NeuroImage. 2007 May 1;35(4):1459–72.

199. Parker GD, Marshall D, Rosin PL, Drage N, Richmond S, Jones DK. A pitfall in the reconstruction of fibre ODFs using spherical deconvolution of diffusion MRI data. NeuroImage. 2013 Jan 15;65:433–48.

200. Tournier J-D, Yeh C-H, Calamante F, Cho K-H, Connelly A, Lin C-P. Resolving crossing fibres using constrained spherical deconvolution: Validation using diffusion-weighted imaging phantom data. NeuroImage. 2008 Aug 15;42(2):617–25.

201. Tournier J-D, Calamante F, Connelly A. MRtrix: Diffusion tractography in crossing fiber regions. Int J Imaging Syst Technol. 2012 Mar;22(1):53–66.

202. Mori S, Crain BJ, Chacko VP, van Zijl PC. Three-dimensional tracking of axonal projections in the brain by magnetic resonance imaging. Ann Neurol. 1999 Feb;45(2):265–9.

203. Jones DK. Precision and accuracy in diffusion tensor magnetic resonance imaging. Top Magn Reson Imaging. 2010;21(2):87–99.

204. Jones DK, Knösche TR, Turner R. White matter integrity, fiber count, and other fallacies: The do's and don'ts of diffusion MRI. NeuroImage. 2013 Jun;73:239–54.

205. Morris DM, Embleton KV, Parker GJM. Probabilistic fibre tracking: Differentiation of connections from chance events. NeuroImage. 2008 Oct 1;42(4):1329–39.

206. Wakana S, Jiang H, Nagae-Poetscher LM, van Zijl PCM, Mori S. Fiber tract-based atlas of human white matter anatomy. Radiology. 2004;230:77–87.

207. Catani M, Thiebaut de Schotten M. A diffusion tensor imaging tractography atlas for virtual in vivo dissections. Cortex. 2008 Sep;44(8):1105–32.

208. Wakana S, Caprihan A, Panzenboeck MM, Fallon JH, Perry M, Gollub RL, et al. Reproducibility of quantitative tractography methods applied to cerebral white matter. Neuroimage. 2007;36(3):630–44.

209. Thiebaut de Schotten M, ffytche DH, Bizzi A, Dell'Acqua F, Allin M, Walshe M, et al. Atlasing location, asymmetry and inter-subject variability of white matter tracts in the human brain with MR diffusion tractography. NeuroImage. 2011 Jan;54(1):49–59.

210. Dayan M, Kreutzer S, Clark CA. Tractography of the optic radiation: a repeatability and reproducibility study. NMR Biomed. 2015 Apr;28(4):423–31.

211. Lawes INC, Barrick TR, Murugam V, Spierings N, Evans DR, Song M, et al. Atlas-based segmentation of white matter tracts of the human brain using diffusion tensor tractography and comparison with classical dissection. NeuroImage. 2008 Jan 1;39(1):62–79.

212. Behrens TEJ, Johansen-Berg H, Woolrich MW, Smith SM, Wheeler-Kingshott C a. M, Boulby PA, et al. Non-invasive mapping of connections between human thalamus and cortex using diffusion imaging. Nat Neurosci. 2003 Jul;6(7):750–7.

213. Staempfli P, Reischauer C, Jaermann T, Valavanis A, Kollias S, Boesiger P. Combining fMRI and DTI: A framework for exploring the limits of fMRI-guided DTI fiber tracking and for verifying DTI-based fiber tractography results. NeuroImage. 2008 Jan 1;39(1):119–26.

214. Newton JM, Ward NS, Parker GJM, Deichmann R, Alexander DC, Friston KJ, et al. Non-invasive mapping of corticofugal fibres from multiple motor areas—relevance to stroke recovery. Brain. 2006 Jul 1;129(7):1844–58.

215. Calamante F, Tournier J-D, Jackson GD, Connelly A. Track-density imaging (TDI): Super-resolution white matter imaging using whole-brain track-density mapping. NeuroImage. 2010 Dec;53(4):1233–43.

216. Calamante F, Tournier J-D, Smith RE, Connelly A. A generalised framework for super-resolution track-weighted imaging. NeuroImage. 2012 Feb;59(3):2494–503.

217. Toosy AT, Ciccarelli O, Parker GJ., Wheeler-Kingshott CA., Miller DH, Thompson AJ. Characterizing function–structure relationships in the human visual system with functional MRI and diffusion tensor imaging. NeuroImage. 2004 Apr;21(4):1452–63.

218. Moseley ME, Cohen Y, Kucharczyk J, Mintorovitch J, Asgari HS, Wendland MF, et al. Diffusion-weighted MR imaging of anisotropic water diffusion in cat central nervous system. Radiology. 1990 Aug 1;176(2):439–45.

219. Song S-K, Yoshino J, Le TQ, Lin S-J, Sun S-W, Cross AH, et al. Demyelination increases radial diffusivity in corpus callosum of mouse brain. NeuroImage. 2005 May 15;26(1):132–40.

220. Song S-K, Sun S-W, Ramsbottom MJ, Chang C, Russell J, Cross AH. Dysmyelination Revealed through MRI as Increased Radial (but Unchanged Axial) Diffusion of Water. NeuroImage. 2002 Nov;17(3):1429–36.

221. Song S-K, Sun S-W, Ju W-K, Lin S-J, Cross AH, Neufeld AH. Diffusion tensor imaging detects and differentiates axon and myelin degeneration in mouse optic nerve after retinal ischemia. NeuroImage. 2003 Nov;20(3):1714–22.

222. Thomalla G, Glauche V, Koch MA, Beaulieu C, Weiller C, Röther J. Diffusion tensor imaging detects early Wallerian degeneration of the pyramidal tract after ischemic stroke. NeuroImage. 2004 Aug;22(4):1767–74.

223. Beaulieu C. CHAPTER 6 - The Biological Basis of Diffusion Anisotropy A2 - Behrens, Heidi Johansen-BergTimothy E.J. In: Diffusion MRI. San Diego: Academic Press; 2009. p. 105–26.

224. Vos SB, Jones DK, Jeurissen B, Viergever MA, Leemans A. The influence of complex white matter architecture on the mean diffusivity in diffusion tensor MRI of the human brain. NeuroImage. 2012 Feb 1;59(3):2208–16.

225. Raffelt D, Tournier J-D, Rose S, Ridgway GR, Henderson R, Crozier S, et al. Apparent Fibre Density: a novel measure for the analysis of diffusion-weighted magnetic resonance images. NeuroImage. 2012 Feb 15;59(4):3976–94.

226. Dell'Acqua F, Simmons A, Williams SCR, Catani M. Can spherical deconvolution provide more information than fiber orientations? Hindrance modulated orientational anisotropy, a true-tract specific index to characterize white matter diffusion: Hindrance Modulated Orientational Anisotropy. Hum Brain Mapp. 2013 Oct;34(10):2464–83.

227. Ashburner J, Friston KJ. Voxel-Based Morphometry—The Methods. NeuroImage. 2000 Jun;11(6):805–21.

228. Jones DK, Symms MR, Cercignani M, Howard RJ. The effect of filter size on VBM analyses of DT-MRI data. NeuroImage. 2005 Jun;26(2):546–54.

229. Jones DK, Griffin LD, Alexander DC, Catani M, Horsfield MA, Howard R, et al. Spatial Normalization and Averaging of Diffusion Tensor MRI Data Sets. NeuroImage. 2002 Oct;17(2):592–617.

230. Smith SM, Jenkinson M, Johansen-Berg H, Rueckert D, Nichols TE, Mackay CE, et al. Tract-based spatial statistics: Voxelwise analysis of multi-subject diffusion data. NeuroImage. 2006 Jul;31(4):1487–505.

231. Kanaan RA, Shergill SS, Barker GJ, Catani M, Ng VW, Howard R, et al. Tract-specific anisotropy measurements in diffusion tensor imaging. Psychiatry Res Neuroimaging. 2006 Jan 30;146(1):73–82.

232. Heiervang E, Behrens TEJ, Mackay CE, Robson MD, Johansen-Berg H. Between session reproducibility and between subject variability of diffusion MR and tractography measures. NeuroImage. 2006 Nov;33(3):867–77.

233. Besseling RMH, Jansen JFA, Overvliet GM, Vaessen MJ, Braakman HMH, Hofman PAM, et al. Tract Specific Reproducibility of Tractography Based Morphology and Diffusion Metrics. PLoS ONE. 2012 Apr 2;7(4):e34125.

234. Alexander DC, Pierpaoli C, Basser PJ, Gee JC. Spatial transformations of diffusion tensor magnetic resonance images. IEEE Trans Med Imaging. 2001 Nov;20(11):1131–9.

235. Engel SA, Glover GH, Wandell BA. Retinotopic organization in human visual cortex and the spatial precision of functional MRI. Cereb Cortex. 1997;7(2):181–92.

236. Morland AB, Baseler HA, Hoffmann MB, Sharpe LT, Wandell BA. Abnormal retinotopic representations in human visual cortex revealed by fMRI. Acta Psychol (Amst). 2001 Apr;107(1-3):229–47.

237. Sunness JS, Liu T, Yantis S. Retinotopic mapping of the visual cortex using functional magnetic resonance imaging in a patient with central scotomas from atrophic macular degeneration. Ophthalmology. 2004 Aug;111(8):1595–8.

238. Levin N, Dumoulin SO, Winawer J, Dougherty RF, Wandell BA. Cortical Maps and White Matter Tracts following Long Period of Visual Deprivation and Retinal Image Restoration. Neuron. 2010 Jan;65(1):21–31.

239. Jezzard P, Matthews PM, Smith SM, editors. Functional MRI: an introduction to methods. Oxford ; New York: Oxford University Press; 2001. 390 p.

240. Ogawa S, Lee T-M, Kay AR, Tank DW. Brain magnetic resonance imaging with contrast dependent on blood oxygenation. Proc Natl Acad Sci. 1990;87(24):9868–72.

241. Jenkinson M, Bannister P, Brady M, Smith S. Improved optimization for the robust and accurate linear registration and motion correction of brain images. NeuroImage. 2002 Oct;17(2):825–41.

242. Larsson J, Heeger DJ. Two Retinotopic Visual Areas in Human Lateral Occipital Cortex. J Neurosci. 2006 Dec 20;26(51):13128–42.

243. Portney LG, Watkins MP. Foundations of clinical research: applications to practice. 3rd ed. Upper Saddle River, N.J: Pearson/Prentice Hall; 2009. 892 p.

244. Avants BB, Epstein CL, Grossman M, Gee JC. Symmetric diffeomorphic image registration with cross-correlation: evaluating automated labeling of elderly and neurodegenerative brain. Med Image Anal. 2008;12(1):26–41.

245. Sherbondy AJ, Dougherty RF, Napel S, Wandell BA. Identifying the human optic radiation using diffusion imaging and fiber tractography. J Vis. 2008 Dec 1;8(10):12–12.

246. Ebeling U, Reulen HJ. Neurosurgical topography of the optic radiation in the temporal lobe. Acta Neurochir (Wien). 1988;92(1-4):29–36.

247. Landis JR, Koch GG. An application of hierarchical kappa-type statistics in the assessment of majority agreement among multiple observers. Biometrics. 1977 Jun;33(2):363–74.

248. Sample PA, Dannheim F, Artes PH, Dietzsch J, Henson D, Johnson CA, et al. Imaging and Perimetry Society standards and guidelines. Optom Vis Sci Off Publ Am Acad Optom. 2011 Jan;88(1):4–7.

249. Smith RE, Tournier J-D, Calamante F, Connelly A. SIFT: Spherical-deconvolution informed filtering of tractograms. NeuroImage. 2013 Feb;67:298–312.

250. Andrews TJ, Halpern SD, Purves D. Correlated Size Variations in Human Visual Cortex, Lateral Geniculate Nucleus, and Optic Tract. J Neurosci. 1997 Apr 15;17(8):2859–68.

251. Kastner S, O'Connor DH, Fukui MM, Fehd HM, Herwig U, Pinsk MA. Functional Imaging of the Human Lateral Geniculate Nucleus and Pulvinar. J Neurophysiol. 2004 Jan 1;91(1):438–48.

252. Fujita N, Tanaka H, Takanashi M, Hirabuki N, Abe K, Yoshimura H, et al. Lateral Geniculate Nucleus: Anatomic and Functional Identification by Use of MR Imaging. Am J Neuroradiol. 2001 Jan 10;22(9):1719–26.

253. Kammen A, Law M, Tjan BS, Toga AW, Shi Y. Automated retinofugal visual pathway reconstruction with multi-shell HARDI and FOD-based analysis. NeuroImage. 2016 Jan;125:767–79.

254. Yamamoto T, Yamada K, Nishimura T, Kinoshita S. Tractography to Depict Three Layers of Visual Field Trajectories to the Calcarine Gyri. Am J Ophthalmol. 2005 Nov;140(5):781–5.e1.

255. Lennartsson F, Nilsson M, Flodmark O, Jacobson L. Damage to the Immature Optic Radiation Causes Severe Reduction of the Retinal Nerve Fiber Layer, Resulting in Predictable Visual Field Defects. Invest Ophthalmol Vis Sci. 2014 Dec 18;55(12):8278–88.

256. Axer H, Keyserlingk DG v. Mapping of fiber orientation in human internal capsule by means of polarized light and confocal scanning laser microscopy. J Neurosci Methods. 2000 Jan 15;94(2):165–75.

257. Nowell M, Vos SB, Sidhu M, Wilcoxen K, Sargsyan N, Ourselin S, et al. Meyer's loop asymmetry and language lateralisation in epilepsy. J Neurol Neurosurg Psychiatry. 2015 Sep 18;jnnp – 2015–311161.

258. Glenn OA, Ludeman NA, Berman JI, Wu YW, Lu Y, Bartha AI, et al. Diffusion Tensor MR Imaging Tractography of the Pyramidal Tracts Correlates with Clinical Motor Function in Children with Congenital Hemiparesis. Am J Neuroradiol. 2007 Oct 1;28(9):1796–802.

259. Bleyenheuft Y, Grandin CB, Cosnard G, Olivier E, Thonnard J-L. Corticospinal Dysgenesis and Upper-Limb Deficits in Congenital Hemiplegia: A Diffusion Tensor Imaging Study. PEDIATRICS. 2007 Nov 19;120(6):e1502–11.

260. Cowey A, Stoerig P, Perry VH. Transneuronal retrograde degeneration of retinal ganglion cells after damage to striate cortex in macaque monkeys: selective loss of P beta cells. Neuroscience. 1989;29(1):65–80.

261. Cowey A, Alexander I, Stoerig P. Transneuronal retrograde degeneration of retinal ganglion cells and optic tract in hemianopic monkeys and humans. Brain. 2011 Jul 1;134(7):2149–57.

262. Hendrickson A, Warner CE, Possin D, Huang J, Kwan WC, Bourne JA. Retrograde transneuronal degeneration in the retina and lateral geniculate nucleus of the V1-lesioned marmoset monkey. Brain Struct Funct. 2015 Jan;220(1):351–60.

263. Beatty RM, Sadun AA, Smith LEH, Vonsattel JP, Richardson EP. Direct demonstration of transsynaptic degeneration in the human visual system: a comparison of retrograde and anterograde changes. J Neurol Neurosurg Psychiatry. 1982;45(2):143–6.

264. Rothman AL, Sevilla MB, Mangalesh S, Gustafson KE, Edwards L, Cotten CM, et al. Thinner Retinal Nerve Fiber Layer in Very Preterm Versus Term Infants and Relationship to Brain Anatomy and Neurodevelopment. Am J Ophthalmol. 2015 Dec;160(6):1296–308.e2.

265. Kidokoro H, Neil JJ, Inder TE. New MR Imaging Assessment Tool to Define Brain Abnormalities in Very Preterm Infants at Term. Am J Neuroradiol. 2013 Nov 1;34(11):2208–14.